GRAPHENE QUANTUM DOT-BASED ORGANIC LOGHT EMITTING DIODES

by

Mohammad Taghi Sharbati

B.S. in Electrical Engineering, Mazandaran University, Iran, 2006

M.S. in Electrical Engineering, Shiraz University of Technology, Iran, 2009

Submitted to the Graduate Faculty of

Swanson School of Engineering in partial fulfillment

of the requirements for the degree of

Master of Science

University of Pittsburgh

2016

UNIVERSITY OF PITTSBURGH

SWANSON SCHOOL OF ENGINEERING

This thesis was presented

by

Mohammad Taghi Sharbati

It was defended on

April 8, 2016

and approved by

Mahmoud El Nokali, Ph.D., Associate Professor, Department of Electrical and Computer Engineering

William E Stanchina, PhD., Professor, Department of Electrical and Computer Engineering

Thesis Advisor: Hong Koo Kim, Ph.D., Professor, Department of Electrical and Computer Engineering

GRAPHENE QUANTUM DOT-BASED ORGANIC LIGHT EMITTING DIODES

Mohammad Taghi Sharbati, M.S.

University of Pittsburgh, 2016

Graphene quantum dots (GQDs) have received a great deal of attention due to their unique optical properties, potentially useful for various applications such as display technology, optoelectronics, photovoltaics, sensing, and bioimaging. In this thesis we have investigated GQDs for an emissive layer in all-solution-processed organic light emitting diodes (OLEDs). Our GQD-based OLEDs are designed and fabricated as two different structures: bottom emission configuration on ITO substrate and top emission configuration on p-Si substrate. For both structures, GQDs show multiple emission peaks in blue, green and red regions. This multi-wavelength emission in the visible spectral range suggests presence and involvement of different-sized GQDs. In the case of GQD-OLEDs on silicon substrate, we have applied a SiO_2 buffer layer with various thickness (2-150nm) and investigated the effects on carrier injection and confinement. With thin layers (< 10nm) of SiO2 it is found that the oxide layer well serves as a barrier blocking the direct tunneling of holes from the substrate. With thick layers (20-150nm) of SiO_2 a band bending occurs enabling the Fowler-Nordheim (FN) tunneling of holes into the p-type transport layer. The FN-tunneling-enabled hole injection is found to allow varying the GQD excitation level (carrier energy and concentration), as demonstrated by the spectral change for different oxide thickness.

TABLE OF CONTENTS

LIST OF TABLES

LIST OF FIGURES

PREFACE

I would like to thank Professor Hong Koo Kim, my advisor, for giving me the opportunity to work in his laboratory.

I want to thank Professor Mahmoud El Nokali, depertment chairman, for his great advices and helps during my education. I will also thank him for his guidances and comments as my committee.

I thank Professor Stanchina to serve his time as my committee and provide me with his comments about my work.

My greatest thanks goes to my parents and my lovely wife, Samane, for helping me and encouraging me to overcome the challenges in my life.

1.0 INTRODUCTION

1.1 QUANTUM DOT OLED

For the first time in 2000 Ryzhii and Khmyrova have introduced Quantum Dots (QDs) as a light source and utilized them in QD infrared photodetectors and light emitting diodes [1]. Since 2000, researchers have started to develop and use this promising candidate for display applications [2]. After Organic Light Emitting Diode (OLED), QD Light Emitting Diode (QD LED or QLED) is the next generation for flat panel display technology which is using nano-scale size crystals or colloidal quantum dots (QDs), as a light source. The physics principle of Colloidal QDs is similar to epitaxially grown QDs. In contrast to epitaxially grown quantum dots, colloidal quantum dots have unique advantages owing to their smaller size such as high carrier confinement effect, high quantum yield, high monodispersivity, larg electron-holes interaction, and excellent control over shape and composition [3]. In addition, they can be deposited over large areas by inexpensive solution deposition process like spin coating and roll-to-roll production.

The output light of these nanometer scaled QDs is tuned by their sizes and a small variation in their size will change the emission peak wavelength. The physical concept behind of this photon emission for DQs is described by quantum confinement effects and the emitted photon energy has a reverse relationship with the QDs size [4].

The basic structure of QD LED is similar to the OLED technology but the only difference is that emissive materials for this technology are quantum dots instead of organic semiconductor molecules. To have an efficient hole-electron recombination, a thin layer of QDs are sandwiching between hole transport layers (HTL) and electron transport layers (ETL) which are organic semiconductor molecules. Holes and electrons will transfer and recombine in QDs layer by applying external electric field and photons would be produced. To confine carriers in active layer (QDs), hole blocking and electron blocking layers will be added which results in high recombination efficiency [5]. Some advantages of QD OLED are: low power consumption, pure color, low cost manufacture, etc.

Recently, grapheme quantum dots (GQDs) have attracted a great deal of attention due to their novel optical, electronic, and chemical properties. GQDs are controllable nanometer sized graphen that are able to generate light in various wavelengths from visible to near-infra red. In this study we have investigated GQDs synthesized by bottom-up method with size smaller than 15nm. Quantum confinement effect in GQDs will introduce a band gap into graphen and make it a potential material for optoelectronics applications.

In this thesis we have investigated two kind of GQD based OLEDs which are conventional configuration (bottom emission) on ITO substrate as a transparent anode, and top emission configuration on p-Si substrate. In bottom emission configuration we have introduced and optimized hole transport layers (PEDOT:PSS, Poly-TPD, and PVK) and electron transport layers (TPBi, LiF) to confine electron-hole within active layer and enhance the radiative recombination and device performance.

1.2 GRAPHENE QUANTUN DOTS (GQD) OLED

Although ITO is widely used as anode in OLED devices, it has some drawbacks which are investigated and reported in the literature. Some of these disadvantages are defect formation on the ITO surface shown by scanning electron microscopy, indium diffusing into the organic materials, being inefficient in hole injecting into the organic layers [6-8]. To overcome and remove the disadvantages of ITO substrate, in this study, we have introduced p-type Si as the anode in OLED device structure. In GQD-OLED on p-Si substrate we have applied silicon dioxide with various thicknesses, from ultrathin to very thick layer, grown by thermal oxidation furnace to investigate the carrier confinement and injection effect on device performance. For very thin buffer layer SiO_2 (2 to 10 nm), on the one hand, the holes are penetrating through oxide layer by direct tunneling mechanism to into active layer (QD). On the other hand, by blocking electrons coming from top sputtered ITO, the carrier concentration within active layer is enhanced which results in higher external quantum efficiency. For thicker oxide case, with the help of high external field and occurring band bending phenomena in oxide bad structure, holes will be injecting through oxide and transport to the GQD active layer. For various oxide thicknesses from 23nm to 150nm, the output color is changed. The physical principle of this phenomenon is that the band bending for thicker oxide is larger than the thinner one even at same applied voltage. As a result, only holes with high energy can reach the narrow part of the oxide band and penetrate through the oxide according to the FNT mechanism. These high energy holes have sufficient energy to excite electron-holes from HOMO/LUMO of the molecules with high energy gap. Thus, the emission wavelength is blue shifted for higher oxide thickness and the color is changed accordingly.

2.0 CARRIER TRANSPORT MATERIALS

2.1 ELECTRON TRANSPORT MATERIALS

2.1.1 TPBi

In Figure 2.1, the chemical structure of TPBI has been shown. The HOMO and LUMO energy of TPBI are 6.3 eV and 2.8 eV, respectively. Owing to its large HOMO-LUMO energy gap, 1,3,5-tris(N-phenylbenzimidazol-2-yl)benzene (TPBI) has been recognized as a useful electron-transport and hole blocking layer in OLED applications [9]. This property result in higher recombination efficiency by increasing the carrier confinement in the emissive layer. In addition, since in this study the PVK polymer with hole mobility 2.5×10^{-6} $cm^2\ V^{-1}\ s^{-1}$ has been used as hole transport material, applying TPBI with the same order of transport ability (electron mobility approximately 10^{-5} $cm^2\ V^{-1}s^{-1}$) helps charge balance in active layer [10].

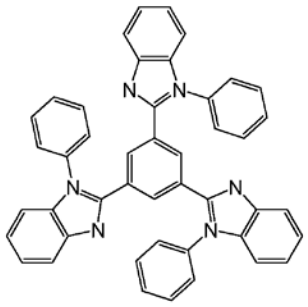

Figure 2.1. Molecular structure of TPBI

2.1.2 TPBI solution preparation

The TPBI polymer was dissolved in a mixture of 0.5 wt % with methanol solvent [11]. To have 0.5%wt for 20 mg of TPBI, we need 4000mg (4gr) solvent. According to methanol molarity (0.791 gr/ml), 4 gr of methanol is equal to 5.05 ml. So by dissolving 20 mg of TPBI in 5.05 ml methanol, TPBI solution with 0.5 wt% is prepared. The related calculations have been listed below:

$(20\ \text{mgr})/x = 0.5/100$ $\gg\gg$ $x = 4\ \text{gr}$ of methanol is required

$(0.791\ \text{gr})/(1\ \text{ml}) = (4\ \text{gr})/x$ $\gg\gg$ $x = 5.05\ \text{ml}$, the required methanol in mili litter

Since the methanol is volatile, stirring for 3 to 4 hour is enough at 80^{oC}. Long time stirring on hot plate can change the amount of methanol due to the evaporation. After TPBI spin coating on the substrate, 20 min annealing at 50^{oC} is applied to dry out moisture.

2.1.3 TPBI thickness measurement

The spin coating condition that applied for TPBI to achieve 20 nm thickness was 3500 rpm for 30 sec. Two different methods for thickness measurement have been used. First, use tape to cover half of the surface, do TPBI spin coating and peel the tape off (Figure 2.2) and measure the thickness by the alpha-step profiler.

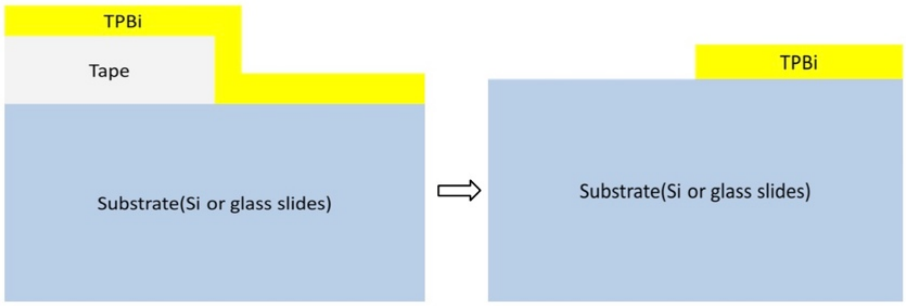

Figure 2.2. Thickness measurement of TPBi using tape

Second, use lithography to create PR patterns and do TPBi spin coating. Then wash away PR and measure the thickness by the alpha-step profiler (Figure 2.3).

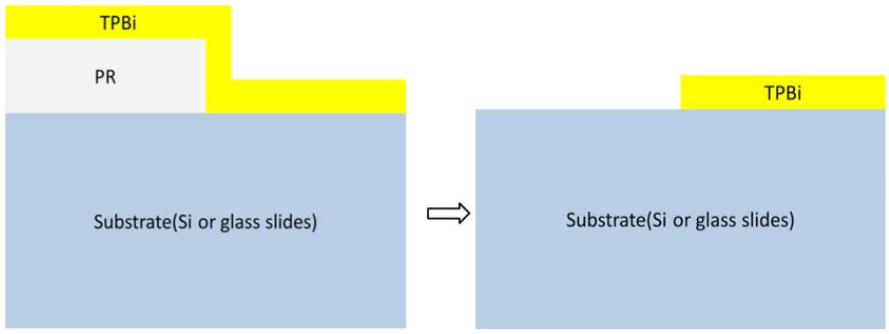

Figure 2.3. Thickness measurement of TPBi using photolithography process

2.2 HOLE TRANSPORT MATERIALS

2.2.1 PEDOT: PSS

PEDOT:PSS is a polymer mixture of polystyrene sulfonic acid (PSS) and poly(3,4,-ethylene dioxythiphene (PEDOT) as shown in Figure 2.4. This compound is available and

applied as a dispersion of gelled particles in water. A conductive layer of this dispersion will be obtained by surface coating on glass substrate and driving out the moisture by heat. This conductive polymer has been widely used as hole injection layer (HIL) by spin coating on indium tin oxide (ITO) due to a high hole affinity, high work function and high transparency. The highest occupied molecular orbital (HOMO) and Lowest unoccupied molecular orbital (LUMO) of PEDOT:PSS are 5.1eV and 3.3eV, respectively. The HOMO value of PEDOT:PSS make it a good candidate for the ITO and p-Si substrates. These small potential barriers facilitate hole carrier transportation from anode to the next layer.

The pristine PEDOT:PSS dispersion conductivity is less than 10 S cm^{-1} and can be improved by a post treatment with some compounds such as ethylene glycol [12-14].

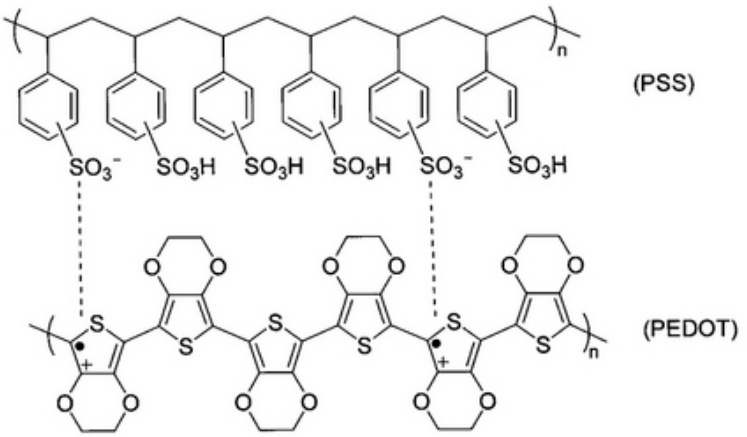

Figure 2.4. Chemical structure of PEDOT:PSS

The commercial PEDOT:PSS was purchased from Heraeus (Clevios PH1000) and filtered through a 0.45 µm filter (PVDF membrane, pore size:0.45µm) to eliminate any possible impurities and particles. To enhance the electrical conductivity, the original solution has been doped by 6% ethylene glycol. The other important factor when we spin coat PEDOT:PSS on ITO

is the surface adhesion. To make a good adhesion and also provide uniform PEDOT:PSS layer, we mixed the solution with 0.25 % p-t-octylophenol (Triton X-100). Finally, the polymer solution including 94% PEDOT:PSS, 6% ethylene glycol, and 0.25% Triton is sonicated by ultrasonic machine for 30 minutes. By spin coating of the prepared solution with 2000 rpm for 40 sec, the PEDOT:PSS film with 50nm thickness will be deposited on the substrate and after 40 minutes heating the layer is ready for further process depends on the substrate.

2.2.2 Poly-TPD

Poly (N,N'-bis(4-butyphenyl)-N,N'-(bis phenyl) benzidine) or Poly-TPD is largely used as a hole transport layer in organic electronics device such as OLED, organic/quantum dot LED, organic field effect transistor and organic solar cells due to its high conductivity and hole mobility (~1×10^{-4} cm^2 V^{-1} s^{-1}), high solubility, and homogenous morphology [15]. In Figure 2.5, the chemical structure of Poly-TPD has been shown. The high HOMO energy (5.4eV) and low LUMO level of energy (2eV) make this polymer a good hole injection and electron blocking material for OLED application. The small potential barrier (~ 0.3eV) between two HOMO levels of PEDOT:PSS and Poly-TPD make Poly-TPD a good hole transport material along with PEDOT:PSS.

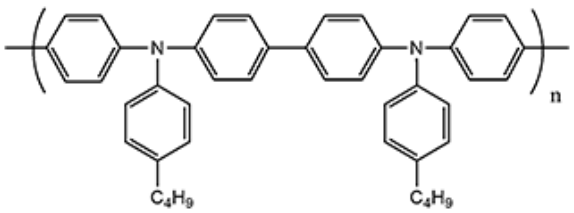

Figure 2.5. Chemical structure of Poly-TPD

2.2.2.1 Poly-TPD solution preparation

Poly-TPD was purchased from American Dye Source Inc. 8 mg poly-TPD is dissolved in 1 ml chlorobenzene (8 mg/ml) [16]. To make a uniform solution and dissolving Poly-TPD in solvent completely, the solution was stirred over one night with 80^{oC}. It is worth mentioning that before every usage of this solution, heating for at 80^{oC} for 30 min can dissolve any recrystallized Poly-TPD.

2.2.2.2 Photoluminescence (PL) of Poly-TPD

The Poly-TPD solution has been coated on pre-cleaned quartz substrate using spin coating. The spin coating speed and time were 2000 rpm and 45 sec, respectively and baked at 110 OC for 20 minutes. The measured thickness of Poly-TPD film was 26 nm. The photoluminescence (PL) measurements was carried out using a 325 nm He-Cd continues-wave (CW) laser (vertically polarized E-field) and BWTek CCD spectrum analyzer as a PL detector at room temperature.

The excitation beam was emitted to the edge of the quartz substrate coated by Poly-TPD and the PL spectra is collected by probe fiber connected to the spectrum analyzer. In Figure 2.6, the PL measurement setup has been shown.

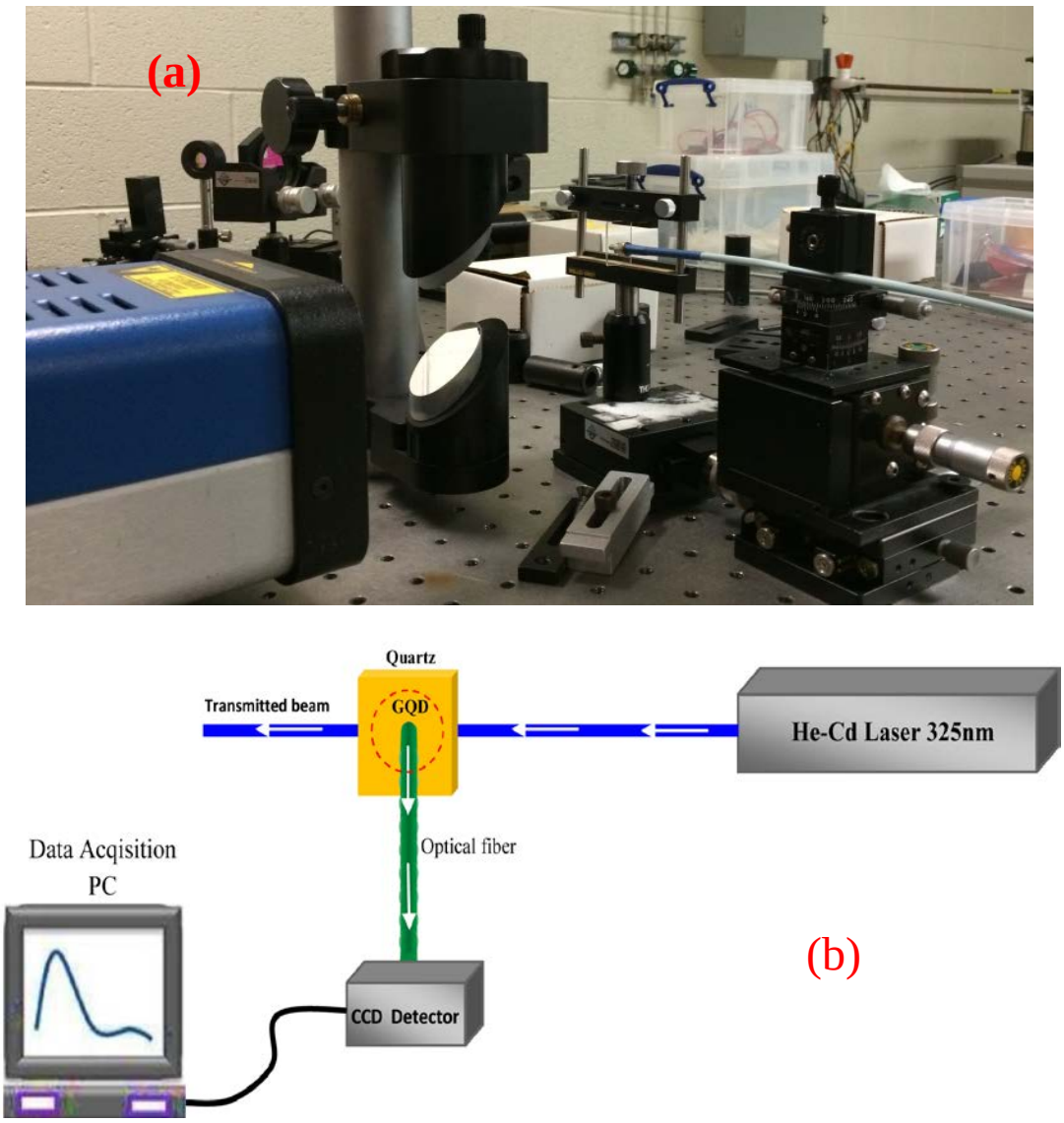

Figure 2.6. The PL measurement Setup (a) Lab. manual setup (b) Schematic

As the Figure 2.7 Shows, the PL spectrum of Poly-TPD has three peaks around 426, 448, and 490nm.

PL measurement condition: Integration time: 5 sec, Average: 1

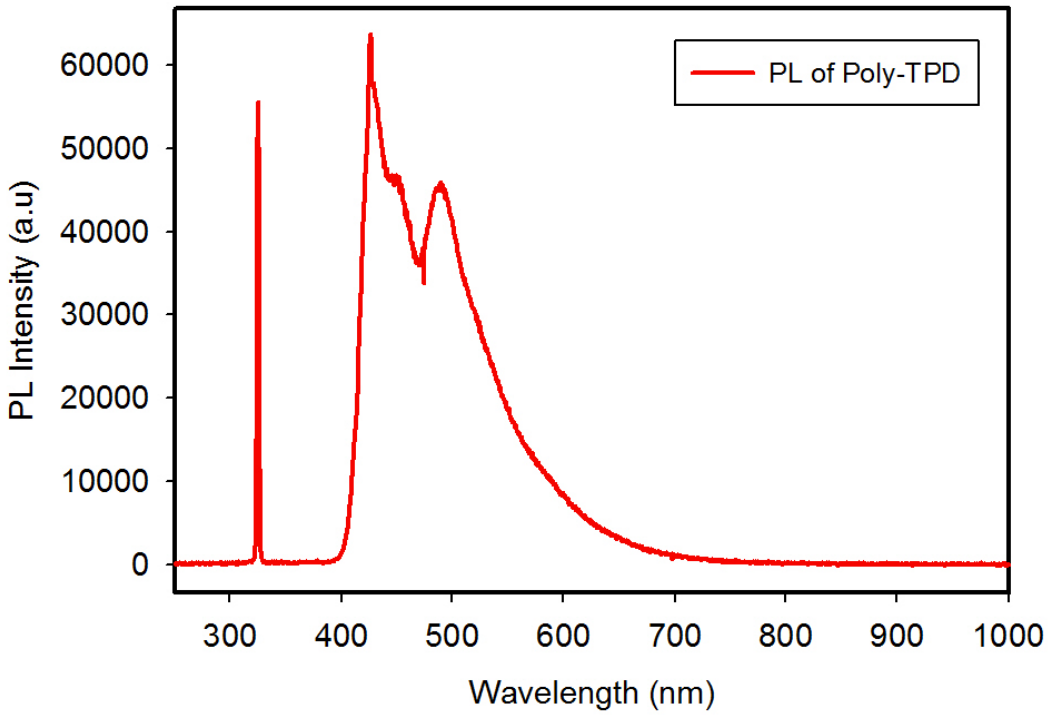

Figure 2.7. PL of Poly-TPD excited by 325 nm He-Cd laser

2.2.3 PVK

Poly(9-vinlycarbazole) or PVK (Figure 2.8) is a conductive polymer with hole mobility of 2.5×10^{-6} cm^2 V^{-1} s^{-1}[17] with HOMO and LUMO level energy of 5.8eV and 2.2 eV, respectively. The PVK was selected as hole transport layer with a higher HOMO level than the hole injection layers (PEDOT:PSS and Poly-TPD) and also as electron blocking layer with LUMO level lower than the emissive material. As a result, we can confine more electron-hole in

the emission layer which in turn increases the recombination efficiency.

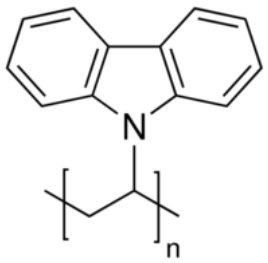

Figure 2.8. Molecular formation of PVK

2.2.3.1 PVK solution preparation

The PVK polymer was dissolved in a mixture of 0.5 wt % with chlorobenzene solvent. Since the density of chlorobenzene at 25^{oC} is about 1.1 g/ml, 10 ml solution of this solvent is equal to 11 gr. As a result, to have a solution with 0.5% PVK, 55 mg pf PVK powder is dissolved in 10ml chlorobenzene [18]. To make a uniform solution, it was stirred for overnight in a rotating magnet plate. Note that, it is possible that the PVK recrystallize in ambient air so it is necessary to stir solution on hot plate (at 80^{oC}) for 30 minutes before every time usage.

2.2.3.2 Photoluminescence (PL) of PVK

The PVK solution was spin-coated onto the quartz substrate at successive rotation speeds of 1000 and 4000 rpm for 10 sec each. This process was carried out at ambient condition and to driving out the moisture the sample baked at 120^{oC} for 30 min in the oven. The measured thickness was about 10nm. The PL of PVK has been measured by manual setup as described for Poly-TPD in section 2.2.2.2. The characterized PL has been shown in Figure 2.9.

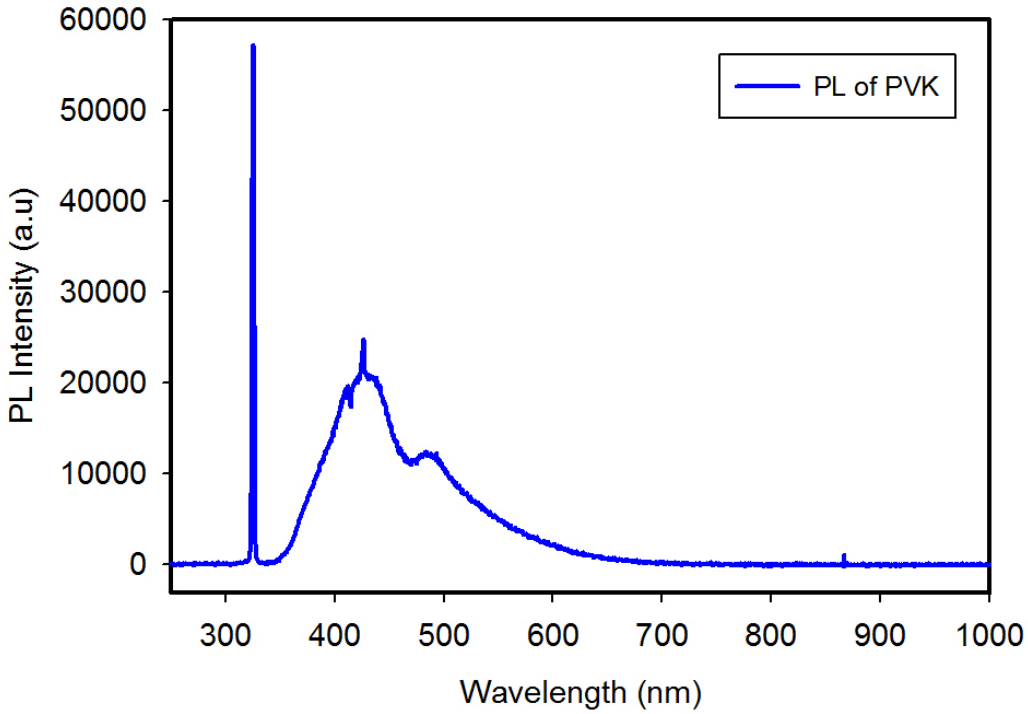

Figure 2.9. PL of PVK excited by 325 nm He-Cd laser

2.2.4 PL comparison between Poly-TPD and PVK

In Figure 2.10a and b showed the the PL comparison of both Poly-TPD and PVK. As the Figure 2.10a illustrates, at the same PL measurement condition, same integration time and average, the PL spectrum of Poly-TPD is much stronger than the PVK spectrum. Figure 2.10b shows the normalized PL intensity for two materials. As the Figure points out, for the both materials we have three peaks at 426, 448 and 490 nm in the right hand side, but for PVK one more peaks is added in left hand side. In other word, for PVK we can see purplish color that participate in PL emission.

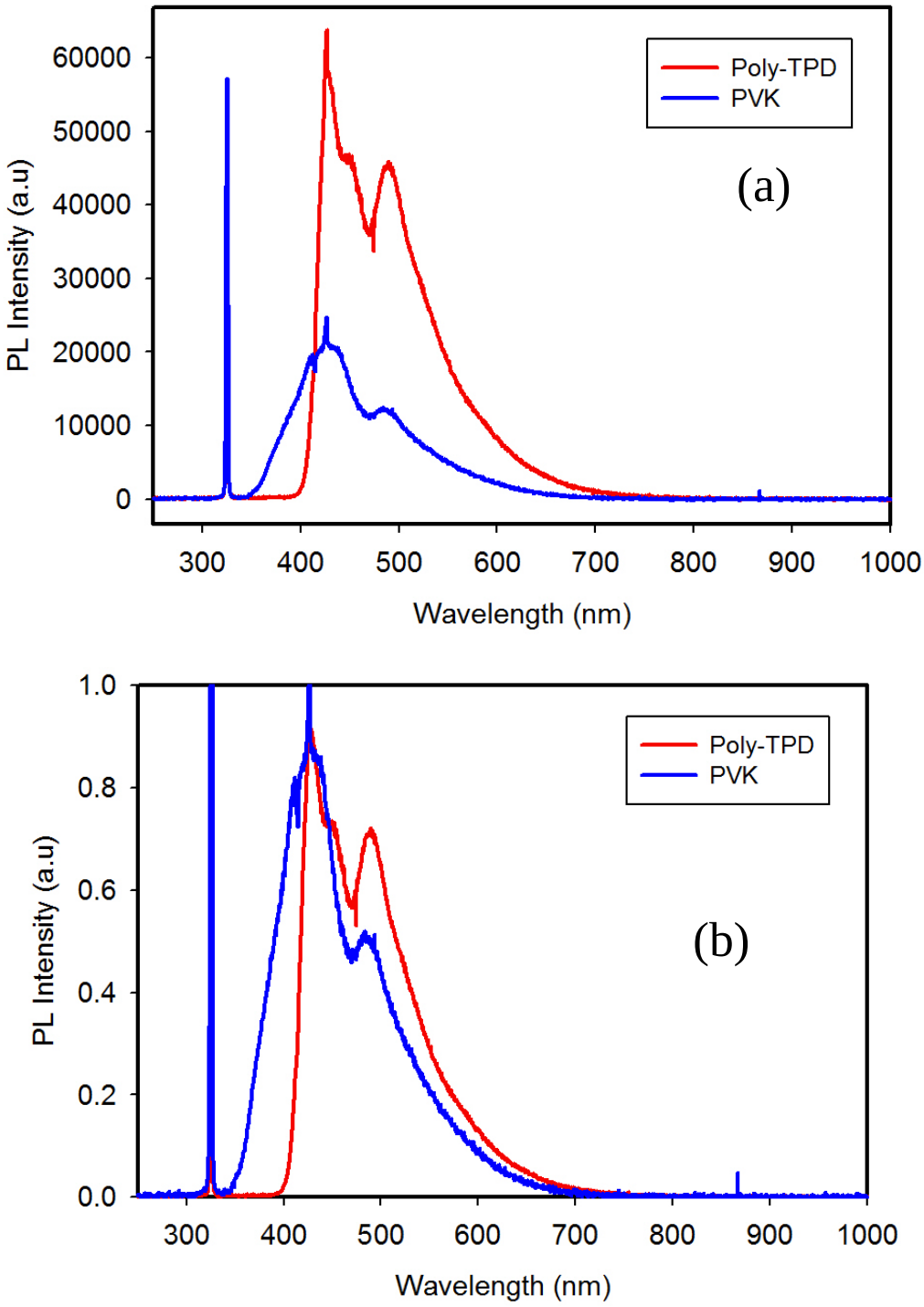

Figure 2.10. (a) Normalized PL spectra comparison between poly-TPD and PVK, (b). PL comparison between poly-TPD and PVK

3.0 EMISSIVE MATERIALS

3.1 GRAPHENE QUANTUM DOTS (GQD)

Graphene is a zero band gap material with an atomically-thin carbon honeycomb lattice structure. Many research has been done on its fundamental properties and applications [19-24]. However, to use graphene with such zero band gap in optoelectronics applications specially in the visible light range, we need to open a band gap in its band structure. One way to make a band gap into grapheme is fabricating graphene in the form of one dimensional nano-ribbons or zero-dimensional quantum dots (nanoscale lateral dimensions). Quantum confinement effect in those structures will introduce a band gap into graphene and make it a promising candidate for optoelectronics applications [25]. Graphene quantum dots (GQDs) have received a great deal of attention due to their unique optoelectronic properties and their considerable potential in different applications such as display technology, optoelectronics, photovoltaics, sensing, and bioimaging [26-29].

Two common fabrication techniques of GQDs are bottom up and top-down [29,30]. The GQDs properties are strongly depends on synthesized process which results in considerable variation in both particle size and chemical structure. Thus, this large variation makes the GQDs luminescence characteristics complex and intriguing [30,31].

Researcher have previously reported that the PL emission of GQD luminescence can be tuned from UV to near-infrared region by edge configuration (zigzag edge sites) [32], defect effect [27], quantum size effect [27, 33], functional group, recombination of localized electron-hole pairs [34, 35], and heterogeneous hybridization of the carbon network. Although the size of GQD has strong effect on their optical properties which is crucial for optical applications, the relationship between size and luminescence properties have not been fully understood. We expect that the GQD should be highly size dependent and as the size diameter increases, the PL emission shifts to longer wavelength. However, the previous studies contradict the size dependent emission of GQDs. GQDs synthesized in various sizes from 1.5 to 60 nm can emit light at different wavelength ranging from deep UV, blue, green and red color with no clear size dependence [36]. For example GQDs with almost large size (60nm) emit blue [37] while small GQDs (1.5-5 nm) emit green light [38]. Two important factors that can address these discrepancies are: First, large heterogeneity of the GQDs synthesized by different methods and second, GQDs PL emission is dependent on some parameters such as defects, size and chemicals components. Here, some of the parameters that can affect the GQD PL emission have been addressed.

1- Shape and size

The PL emission will be changed as the GQDs size and shape increase. Kim et al. showed the population of different shapes for given size of GQDs by high resolution transmission electron microscopy (HRTEM) as shown in Figure 3.1 [39]. Kim group confirmed that the elliptical and circular GQDs have dominant population for the average size of 5 and 12 nm for GQDs and as the size increases to 15nm, the elliptical shape GQDs are the GQDs

configuration and circular shapes are disappeared. At d= 20, and 25 the dominant shapes of GQDs become hexagonal and for d=35nm, the shapes are parallelogram rectangles form with rounded vertices. As a result, the shape of the GQDs is determined by their sizes and for any given size, the dominant shape population is contributing in PL emission. The PL emission peaks of GQDs, have shifted to the red color regions as the size of GQDs is increased.

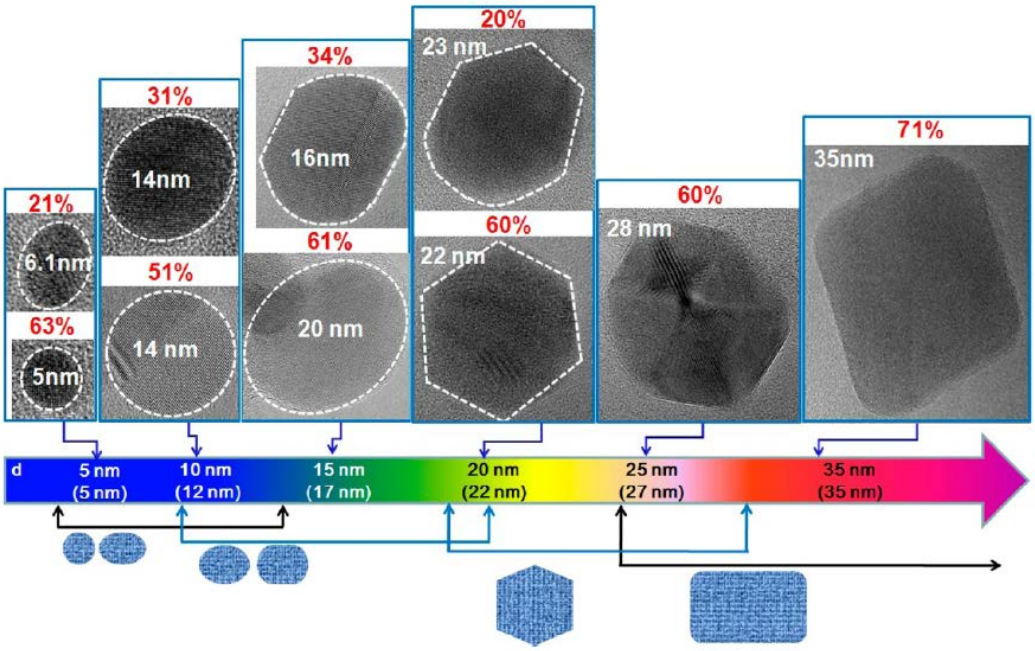

Figure 3.1. The various shapes for a given size of GQDs with lateral diameter d using HRTEM [39].

2- Edge configuration

The chemical structure of the synthesized GQDs can have either zigzag or armchair edge which results in different quantum confinement effects (see Figure 3.2) [40].

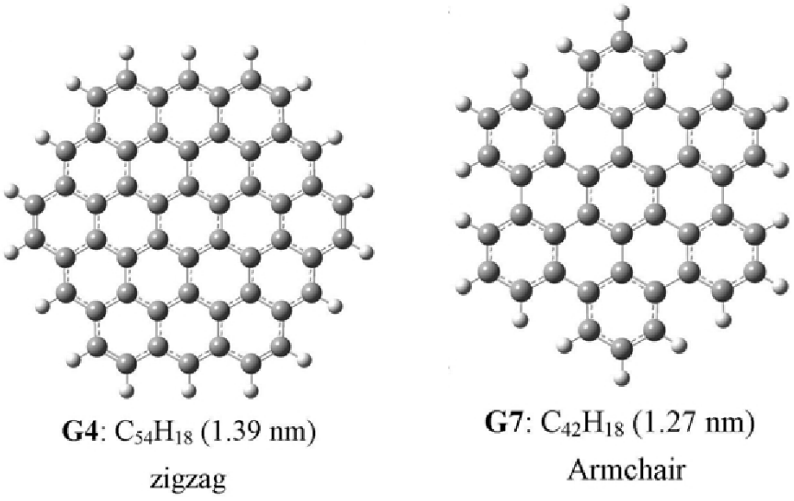

Figure. 3.2. The chemical structure of GQDs with zigzag and armchair edges [40].

Figure 3.3 shows the HRTEM image of a typical GQD reported by Kim et al. [39]. As the figure illustrates, at the edges of GQD particle, a mixture of zigzag and armchair configuration can be seen. The armchair configuration is more at the linear edges but curved regions is consist of both armchair and zigzag structures.

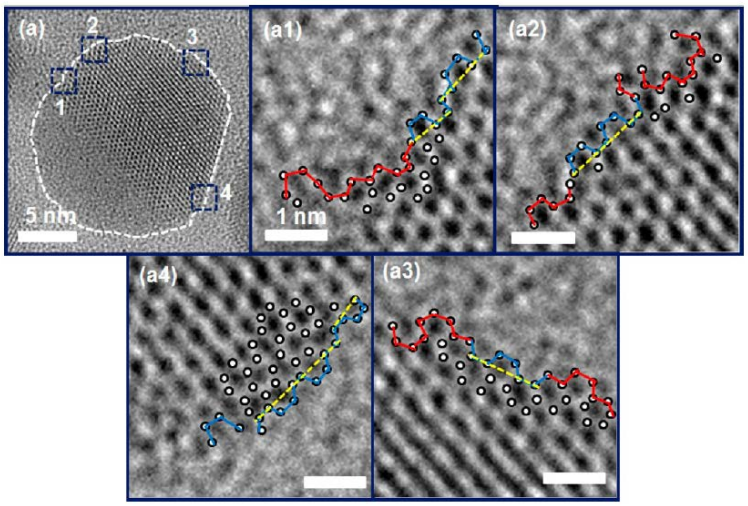

Figure 3.3. The HRTEM images of a typical GQD at four distinct edges (a_1-a_4) with linear and curved shapes. The red and blue lines show zigzag and armchair configuration, respectively [39].

It has been shown that the GQDs with zigzag edges has lower energy band gap rather than armchair edge (Figure 3.4). The reason is that the localized states in zigzag-edged GQD are pushed to the edge sites results in reducing the lowest unoccupied molecular energy (LUMO) and thus decrease the band gap. While armchair-edged GQD structure with the same size have localized states in the center with higher LUMO level and thus larger band gap. As a result, for zigzag GQDs we observe a red shift in compare to blue shift in armchair GQDs [40].

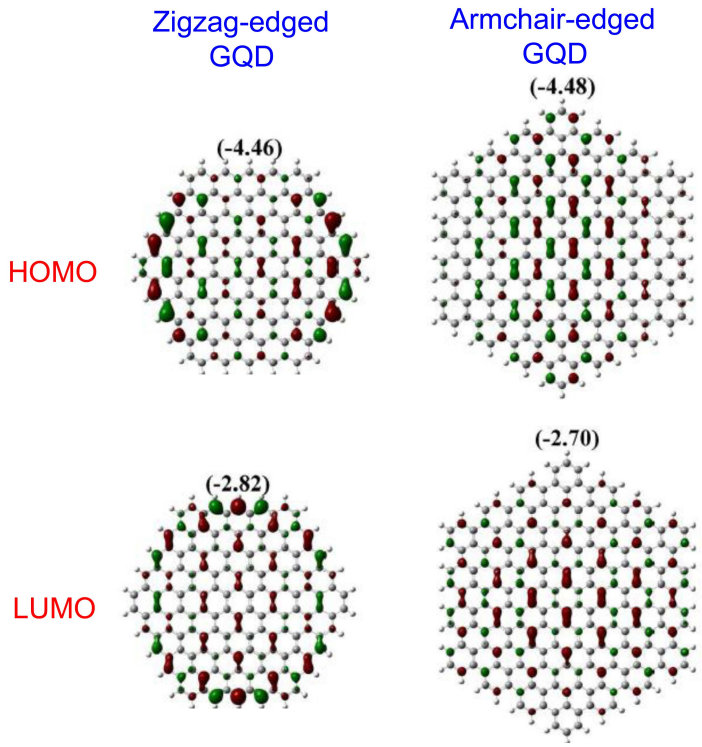

Figure 3.4. HOMO and LUMO level energy for the both zigzag and armchair configuration [40].

3- Oxygenated Functional Groups (OFG)

The functional groups, C-O, C=O, OH, COOH, will reduce the band gap of the GQD. Since the synthesized GQD is containing these groups, the emission peakes would be shifted to the longer wavelength. The theoretical calculation shows showed that adding -OH groups externally to the edge carbon, the PL emission of the GQD is shifted from 572.4 nm (green) to 732.3 nm (red), as shown in Figure 3.5 [40]. Similarly, -COOH attached to the carbon edge change 572.4 nm to 612.3nm.

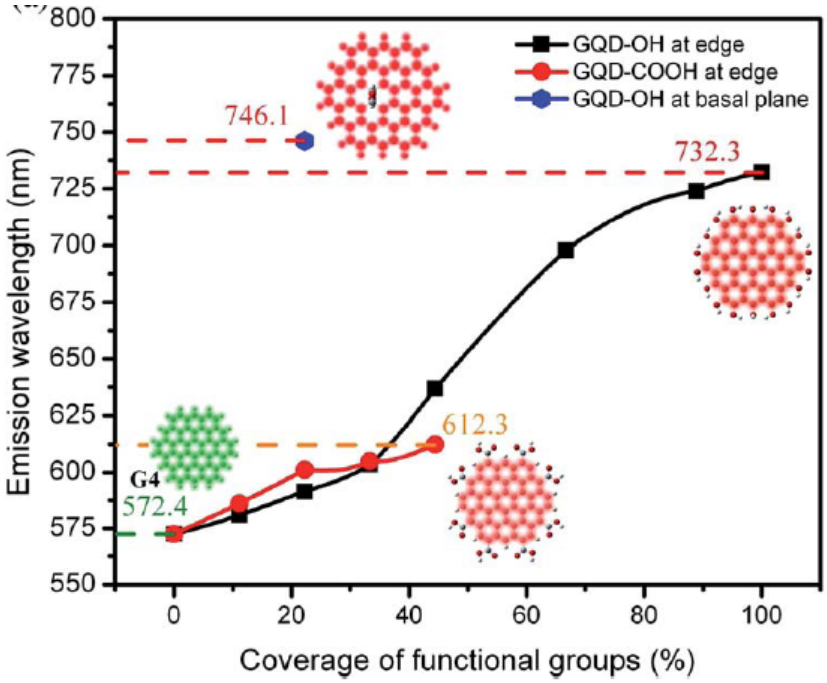

Figure 3.5. The effect of functional groups on emission peak [40].

4- SP^2 clusters

In previous sections, we have introduced some parameters of GQDs such as size, functional group which can change the luminescence properties of GQD. However, those parameters cannot describe why the emission peaks of the almost large GQDs synthesized by top-down methods are usually in green or blue region, instead of red [38, 41-43].

As reported in the literature, the scanning tunneling microscopy and spectroscopy the quantum confinement effect confirmed 0.2 eV energy band gap in 5nm size GQDs fabricated by carbon dots [44]. On the other hand, the recent study for GQDs with typical size (>~5 nm), showed PL emission above 600nm (~2 eV) which is much more than the band gap due to the quantum confinement effect [45]. Lim and Chen are reported that the small sp^2 fragments are the main reason for the red shift of GQD emission. In fact, the p-electrons which are causing the electron resonance are confined within the sp^2 clusters in a small domain and these clusters are determining the GQD emission peak positions rather than the general size of GQD [40]. To support this theory more, they showed that by increasing the sp^2 clusters size, the band gap of GQD is changed. Furthermore, with the fixed size of the sp^2 clusters, they have increased the general size of the GQD but the band gap did not change [40].

In this study, the GQD in IPA solvent has been purchased from ACS materials [46]. The material characteristics and properties have been shown in Table 3.1.

Table 3.1. GQD data purchased from ACS materials [42].

Preparation Method	Bottom-up
Elemental composition/Information on Ingredients (wt %)	H (4%) C (46 %) O (50 %)
Quantum Dots Size	<15 nm
Thickness	0.5-2 nm
Purity	> 80 %
Standard Concentration	1 mg/ml
Solvent	Isopropanol alcohol (IPA)

The TEM image of this GQD [ACS website] shows the quantum dots concentration (see Figure 3.6 [46]). The dark spots indicate the GQDs stacked over each other which results in change in GQD characteristics by changing in its size.

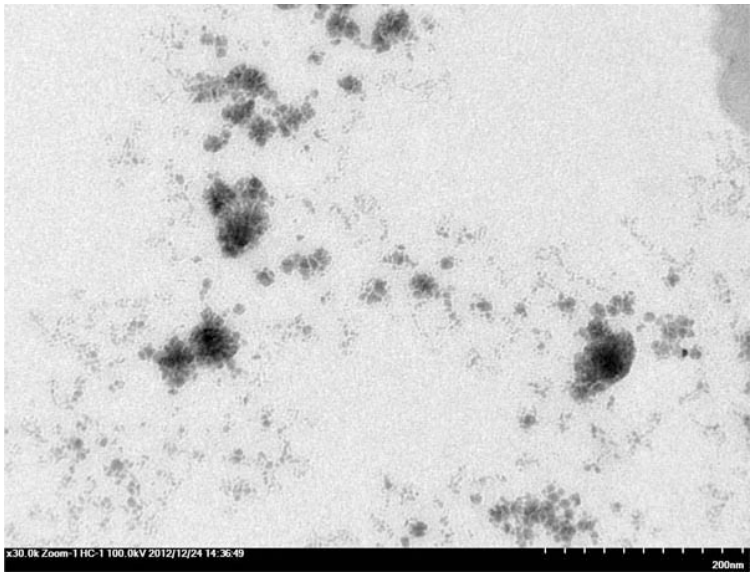

Figure 3.6. TEM image of GQD [46]

3.2 CALCULATION OF NUMBER OF GQD IN GIVEN SOLUTION

In Figure 3.7a and b, the atomic Structures of Graphene (Gr) and one layer of Gr in 0.9 × 0.9 nm^2 area has been shown.

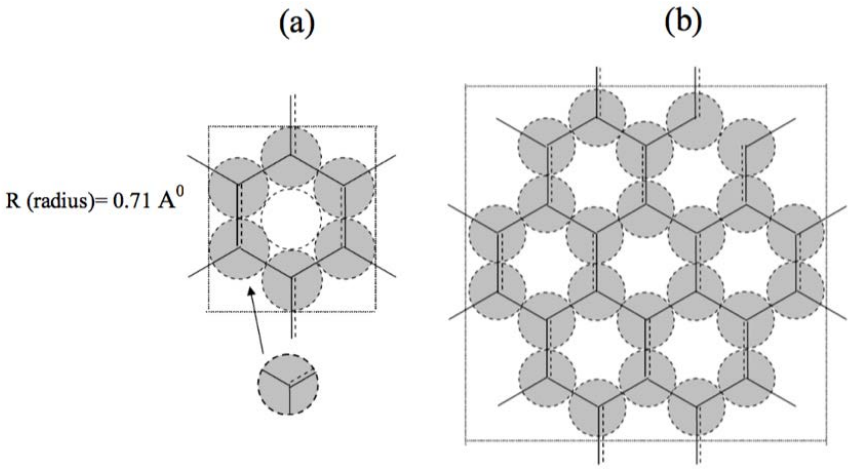

Figure 3.7. The atomic structure of Gr and one-layer Gr on 0.81 nm^2

Number of carbon atoms in this area (0.81 nm^2) is 24 atoms. Our GQD has this characteristics:

Quantum Dots Size: ~ 15nm , Thickness: 0.5-2 nm

So the effective area is : 15× 15 nm^2

Number of carbon atoms in this area (225 nm^2) is: $\frac{225}{0.81} \times 24 = 6666.66666$

On the other hand, in 1 mole we have 6.022×10^{23} (Avogadro number) carbon atoms that are equal to 12 gr. It means that 6666.66666 carbon atoms is equal to 13284.623×10^{-23} gr

So: the mass of each GQD= 13284.623×10^{-23} gr

For our solution the standard concentration is 1 mg/ml. So in 1 ml the number of GQD in one layer of is GQD is equal to:

$$\frac{1mg}{13284.623\times10^{-23}\ gr} = 7.5275 \times 10^{15}\ \frac{1}{ml}$$

With assumption of having 2 layers for each quantum dot, the number of GQD is: $2 \times 7.5275 \times 10^{15} = 15.055 \times 10^{15} \frac{1}{ml}$

We can apply an average between 2 and 1 layer: # of GQD= $1.5 \times 7.5275 \times 10^{15}$ = $11.2911 \times 10^{15} \frac{1}{ml}$

In conclusion, we can predict the number of GQD in each drop depends on the amount of drop. For example, in 1 µl of solution with considering the average number of layers we have about $1.7 \times 10^{12} \frac{1}{\mu l}$ of GQD.

3.3 PHOTOLUMINESCENCE OF GQD

The GQD solution in IPA has been coated on quartz substrate. Before coating, quartz glass cleaned by acetone followed by methanol and DI water in ultrasonic machine for 30 min each and baked at 80^{oC} for 30 min. Then 50 µL GQD spin coated on 1cm×1cm quartz substrate at 2000 rpm for 30 sec and baked at $90^{O}C$ for 30 min. The PL spectra were measured at room temperature using the 325 nm line of a He-Cd laser as the excitation source. Emitted light was collected by an optical fiber probe and analyzed using BWTek CCD spectrum analyzer (see Figure 3.8).

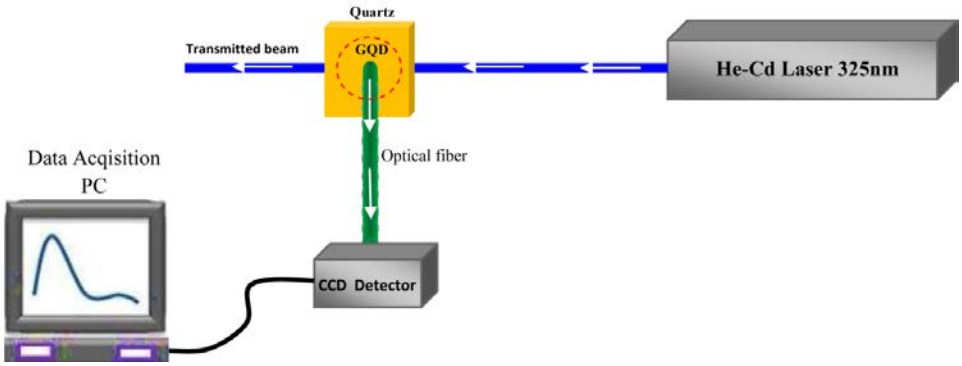

Figure 3.8. Manual set up for PL measurement

Figure 3.9a shows the PL for the one-time spin coating of GQD on quartz. The integration time and average number have been set at 1000 ms and 1, respectively. The PL and also EL spectra of GQD shows complex spectra because of the aggregation effect, oxidation, edge effect and presence of functional group [47]. Also, the GQD PL characteristics shows peak multiple peaks, depending on the status of oxidation and aggregation and on the excitation wavelength [48]. As Figure 3.9b illustrates, by 325 nm laser source two major peaks appeared at 496 and 580 nm. We can amplify the PL intensity by increasing the GQD concentration on the quartz substrate.

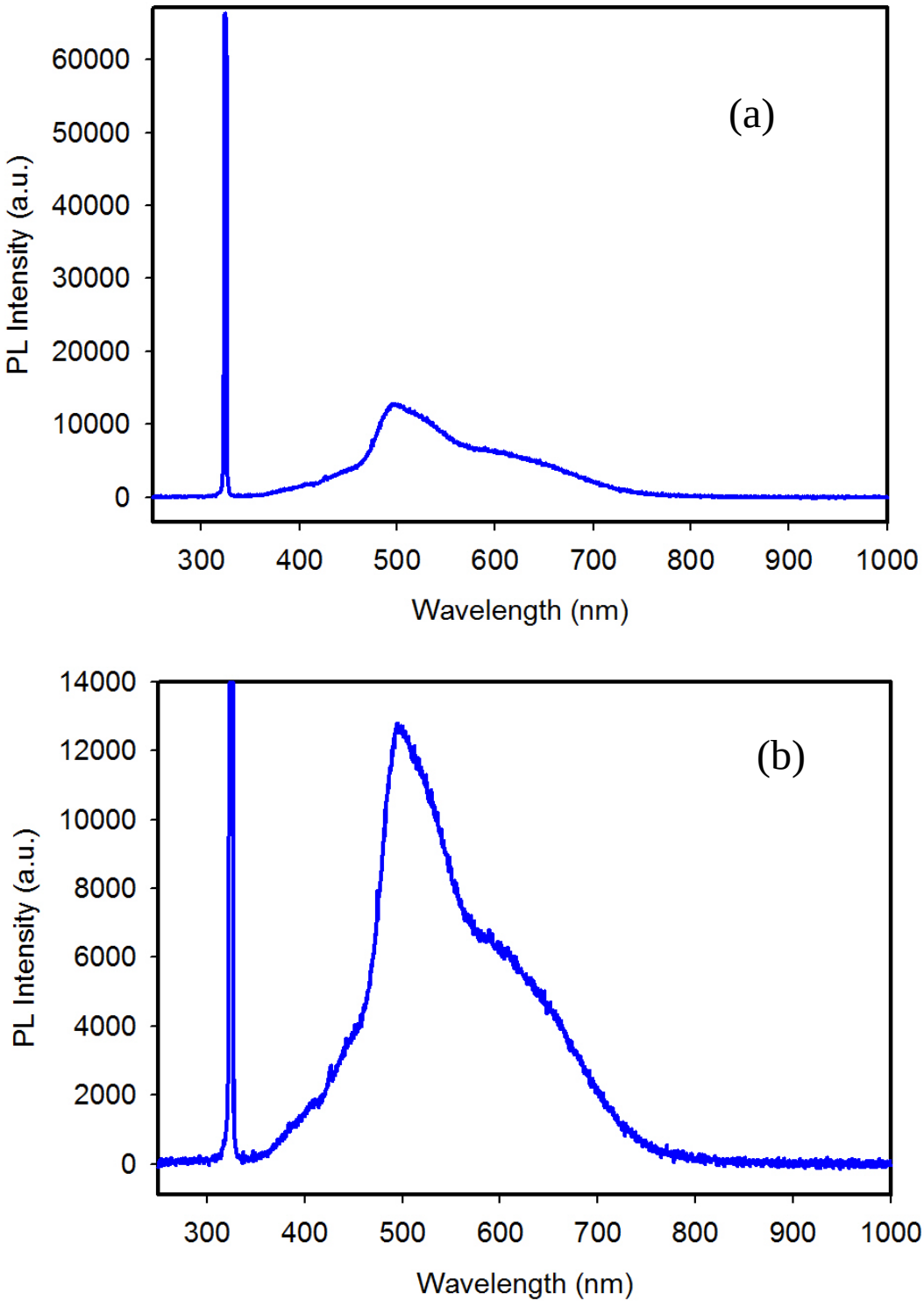

Figure 3.9. (a) The PL of one time spin coated GQD on quartz, (b) normalized PL which shows the two major peaks appeared in GQD PL

In this experiment we have investigated the photoluminescence (PL) property of GQDs with nanometer size (~<15nm). As the PL of one layer spin coated of GQDs on quartz substrates shows, the PL is consist of four distinct peaks at ~404, ~450, ~494 and 584nm. Figure 3.1, shows the TEM image of GQD distribution on quartz substrate. As the figure illustrates, GQDs with various size have various concentration distribution on the quartz surface. As we discussed, the PL emission peaks of the GQDs used in this study are not necessary determined by their overall sizes. Different parameters can be involved for these four distinct wavelength including oxygen containing functional group, shape, overall size and SP^2 clusters.

To increase the PL efficiency, the spin coating process have been repeated for ten times which results in more GQDs concentration on the quarts substrate. As the Figure 3.10 shows, the PL intensity peak has been intensified for the same measurement condition (Integration time: 1000 ms, Average:1).

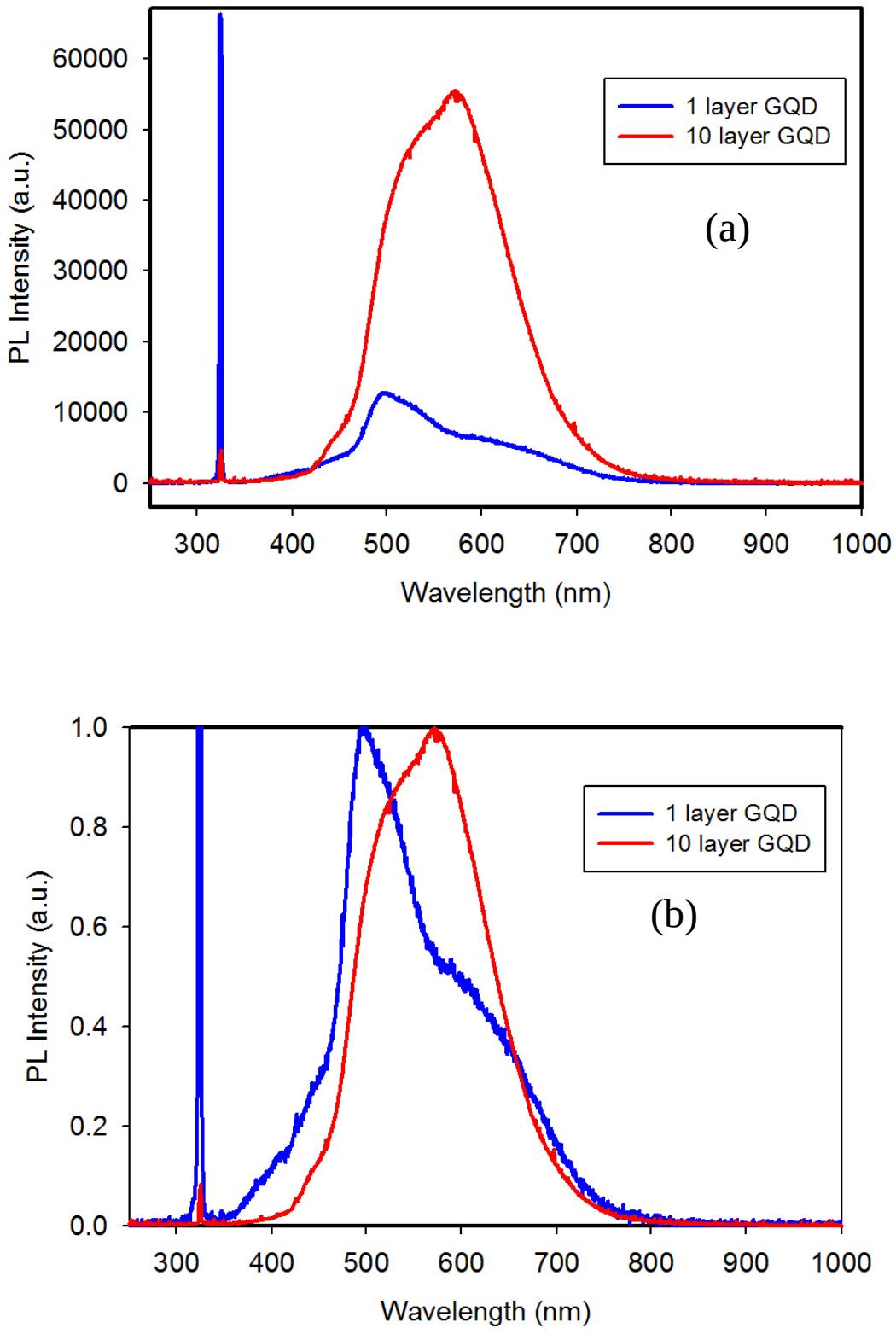

Figure 3.10. (a) PL spectra for one time and 10 times GQD spin coating, and (b) Normalized intensity.

4.0 BOTTOM EMISSION GQD BASED OLED

4.1 TRANSPARENT SUBSTRATE

The transparent ITO on glass r plastic substrate is the most common used material as anode in OLED. Some properties of ITO that make it a good candidate as anode are listed below:

1- High conductivity

2- High work function (WF) to increase the effective hole injection

3- Good thermal and chemical stability

4- High transparency

In OLED, the produced light will go out through anode. In visible range, ITO is transparent due to the high energy gap (>4eV) [49]. Although some other transparent and conductive electrodes such as fluorine injected in tin oxide (FTO) [50] or Al injected in zinc oxide (AZO) [51] are available, easy and rapid access to a glass substrate pre-coated by ITO as a commercial material widely used in liquid crystal displays (LCD) cause we use ITO as anode in OLEDs. However, ITO has some drawbacks like relatively high resistance (2×10^{-4} Ω.cm), surface roughness in rang of 2 nm, surface with chemical reaction which cause ion immigration into the device.

The surface morphology and properties of bare cleaned ITO can have some bad effect on the device characteristics such as I-V curve characteristics, shorting and damaging on the top

cathode surface in continuous operation [52-55]. In addition, since the metal contact has better electron injecting rather than ITO as hole injecting material, the hole density is less than electron density in recombination region which affect OLED efficiency [56,57]. To overcome these problem, some hole injecting/transporting materials have been introduced [56,59]. However, we can modify the ITO surface using oxygen plasma treatment to have a good performance such as lower turn on voltage and higher efficiency in OLEDs by reducing the work function and extra cleaning of ITO [59,60]. Furthermore, by oxygen plasma treatment and increasing the hydrophylicity, the adhesion between ITO and top organic material would be increased and we can make a good contact.

The ITO coated glass substrates used in this study was purchased with sheet resistance of 10 Ω/square and thickness of approximately 100 nm glass substrate dimension: 75×25×0.7mm). Before plasma treatment, a 1cm×1cm ITO is cleaned by acetone, Isopropanol alcohol (IPA), methanol followed by DI water in ultra sonic machine, 30 min each. Then the cleaned ITO is baked in oven for 30 min at 90^{oC}. A 10 min oxygen plasma treatment was performed in RF sputtering machine under an oxygen flow pressure of 45 mTorr, radio frequency forward power of 50 W. Table 4.1 and 4.2 shows the experiment conditions.

Table 4.1. Oxygen plasma treatment condition.

Target	Gas	Distance (between target and sample	O_2 flow pressure (mTorr)	RF- Power (W)	Temperature(^{O}C)	Time (min)
SiO_2	Oxygen	2 inch	30	50	Room temperature	10

Table 4.2. Condition during 10 min oxygen treatment.

Time(min)	FW power/W	RV power/W	DC bias	Pressure/mTorr	Temperature/°C
Presputtering	50	0	341	45	RT
2	50	0	355	45	RT
4	50	0	353	45	RT
6	50	0	350	45	RT
8	50	0	357	45	RT
10	50	0	354	45	RT

4.2 METAL CATHODE

Since the cathode material should not be transparent, there is less limitation for choosing cathode cathode material in compared to the anode ones. The most significant properties that a material should has as an anode are:

1- High conductivity

2- Low work function to have high electron injection

3- Making a good contact with organic layer

4- Good stability

5- High reflectivity coefficient

Usually cathode is a metal with low work function such as Mg, Ca, Ba and Al. In this study, we used the Al as a cathode material with work function of 3.2 eV.Low work function cause a high and better electron injection to the lower unoccupied molecular orbital (LUMO) of the ETL layer. However, low work function results in two disadvantages: 1- reaction with oxygen and moisture and damaging the device. 2- chemical reaction with the neighbour organic layers which decreases the OLED performance. To solve this problem, a composition of LiF/Al

that LiF is a very thin layer (less than 5nm) deposited on Al can be applied. Using this technique, the work function of Al (~4.3eV) changes to 2.6eV (for LiF/Al).

4.3 GQD-OLED FABRICATION TECHNIQUE AND CHARACTERIZATION

4.3.1 All solution process (spin coating)

The OLED in our study is fabricated using all solution technique. In this process, the polymer based carrier (electron-hole) transport materials solution are spin coated using spin coating machine. The spin coating speed (rpm) and time is set for the favorite thickness. As in chap. 2 fully described, the carrier transport material solutions have been prepared. In this section, the step by step of the fabrication process in ambient air is explained.

1) Substrate preparation:

   The glass substrate pre-coated with ITO is treated by oxygen plasma using RF sputtering machine (see section 4.1).

2) PEDOT:PSS coating process

   A thin layer of PEDOT:PSS hole injection material (50 μl mixture of PEDOT:PSS (94%) Ethylene Glycol (6%), and Triton (0.25%) was deposited via spin-coating onto cleaned ITO (1cm×1cm) at 2000 rpm for 40 sec. The film was baked in oven at 120^{oC} for 40 min to dry moisture and obtain a uniform layer.

In the next step, as described in Chap. 2.1., the post treatment process in Ethylene Glycol solution (E.G.) has been applied for 2 min to increase the electrical conductivity of the PEDOT:PSS. The post treated sample is blow dried by N_2 and annealed in oven at 120^{oC} for 40 min to remove E.G. solution from the surface as much as possible.

3) Poly-TPD spin coating

On top of PEDOT:PSS thin film, 50 μl of the prepared hole-transport payer Poly-TPD in chlorobenzene solution with a loading of 8 mg/ml (as described in Cap. 2.2) was spin coated at a speed of a 2000 rpm for 45 seconds followed by baking at 110^{oC} for 20 min. The measured thickness of this layer was 30 nm.

4) PVK spin coating

50 μl of the organic hole transport and electron blocking layer PVK in chlorobenzene solution with a loading of 5.5 mg/ml was spin coated on Glass/ITO/PEDOT:PSS/Poly-TPD at successive rotation speeds of 1000 and 4000 rpm for 10 sec each. The sample is baked in an oven at 120^{oC} for 30 min. The expected thickness of coated layer is 5nm.

5) GQD spin coating

The GQDs emissive material solution dissolved in IPA solution were used as the active layer in OLED structure. A thin layer of GQD was deposited on top of PVK layer by spin coating of 50 μl of GQD IPA solution at 2000 rpm for 30 seconds, followed by drying in oven at 90 ^{oC} for 30 min.

6) TPBI spin coating

The TPBI was used as electron injecting layer and spin-coated on top of the GQDs layer with a loading of 4 mg/ml in methanol solution at a speed of ~3500 rpm for 30 seconds and annealed at 50 ^{oC} for 20 minutes under ambient condition. The measured thickness of this layer was 26 nm.

4.3.2 Thermal evaporation

The Al electrodes (~350nm) as metal electrode have been evaporated by thermal evaporation system through a shadow mask with circle pattern (2.5mm diameter) under a high vacuum of 1.1×10^{-5} Torr. Figure 4.1 shows the top view of the Al deposited in OLED structure. The device area was 4.9 mm^2.

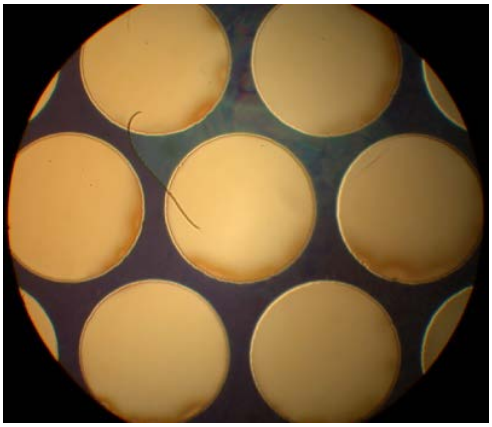

Figure 4.1. Top view of the fabricated OLED with Al in top with diameter 2.5mm.

4.3.3 Thermal evaporation

4.3.3.1 OLED without GQD

All organic electron/hole injection layers have been deposited one by one on ITO substrate by spin coating technique and finally Al cathode is deposited on top by thermal evaporation technique as shown in Figure 4.2.

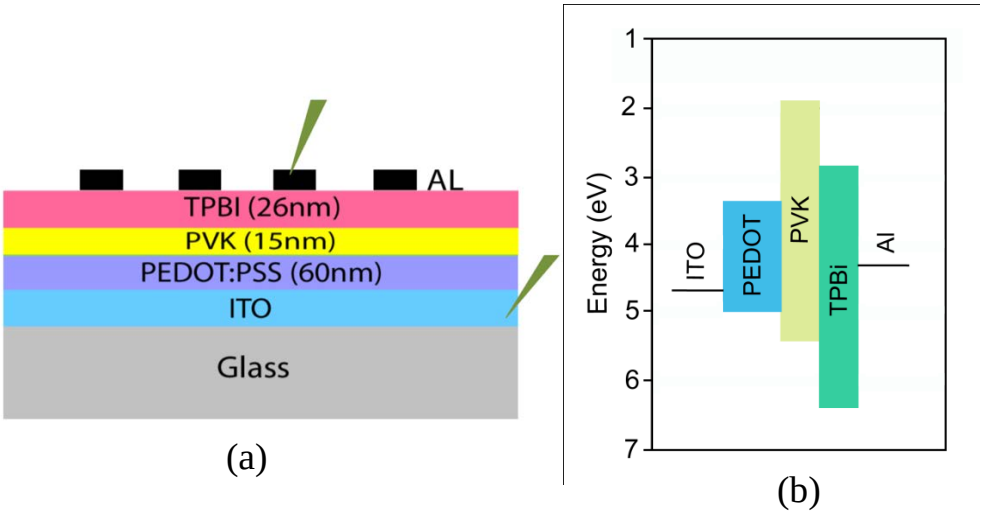

Figure 4.2. (a) OLED structure with PVK as an emissive layer. (b) Energy band diagram of this device.

4.3.3.1.1 PL and EL comparison of PVK

In Figure 4.3, the PL and EL spectrum of PVK hole transport material is shown which indicates their peak positions are comparable. It means that in output light, PVK polymer emission in blue and green regions is included.

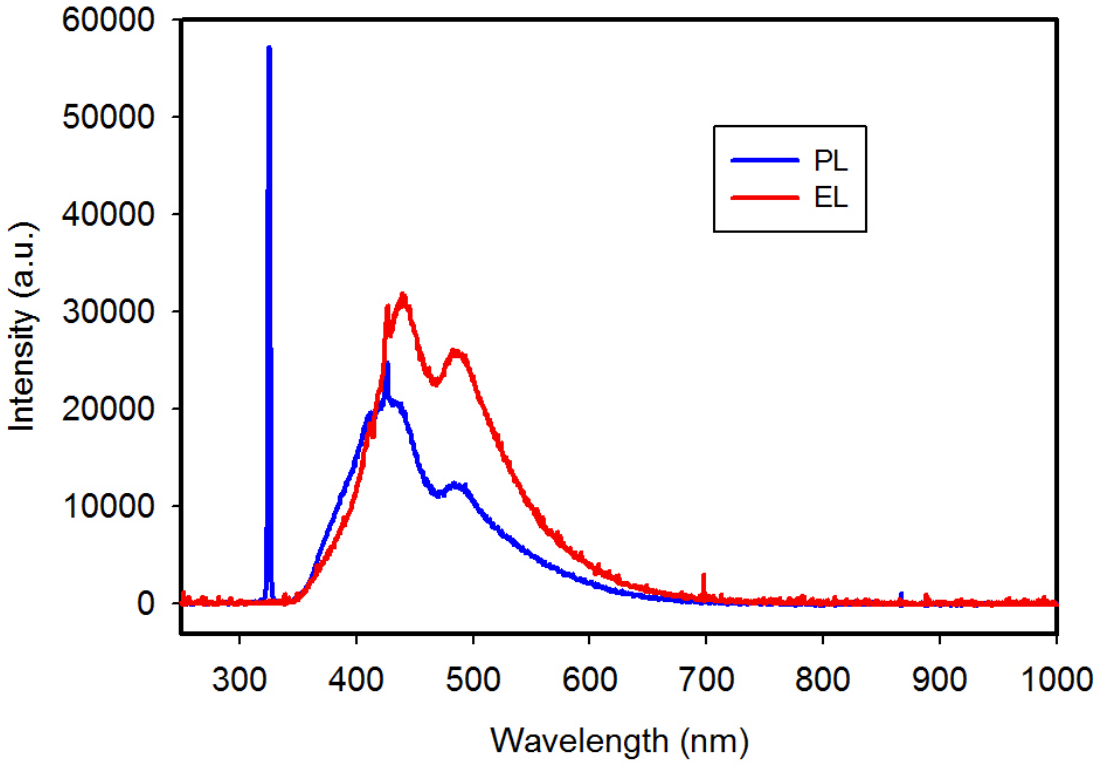

Figure 4.3. PL and EL spectra comparison of PVK hole transport layer

4.3.3.1.2 EL in structure including PVK and Poly-TPD

In this section, the all solution proceeded OLED has been made by stacking organic polymers on pre-cleaned ITO substrate. The ITO is cleaned by solvent cleaning process using acetone, IPA, methanol followed by DI water in ultrasonic bath for 10 min each. The organic layers are deposited one by one with described conditions in Chap. 2. Finally, top Al electrodes as cathode are deposited by thermal evaporator at 1.1×10^{-5} torr. A metal mask with 2.5mm diameter hole is used for Al electrodes patterning (see Figure 4.4)

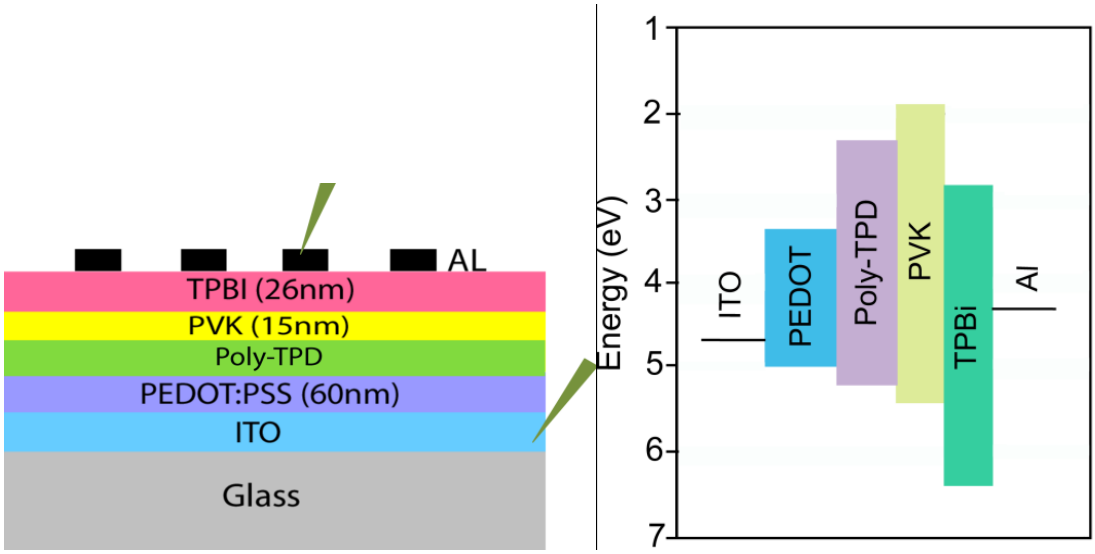

Figure 4.4. (a) OLED structure without GQD active layer. (b) Band diagram energy of the OLED structure without GQD layer

We introduced this structure as a reference sample without embedding GQD as an active layer. In this system, by applying electrical forward bias, electrons and holes are transported and injected into PVK and Poly-TPD through TPBI and PEDOT, respectively. For this experiment, we set HP4245 semiconductor analyzer in constant current 30 mA and the integration time of the CW output light in BWTek CCD was 10 sec. Recombination has occurred and the measured EL spectrum of the OLED is shown in Figure 4.5 . The EL spectrum has multiple peaks in blue and green area that come from both PVK and Poly-TPD organic layers. The energy band diagram (with respect to the vacuum level) of the fabricated LED device is shown in Figure 4.4b. The charge carrier balance due to the appropriate carrier transport layers helps efficient recombination in emissive layer. Poly-TPD as hole injection layer, not only helps injection by decreasing the offset voltage between ITO and PVK, but also inject large amount of holes to the next layer with high hole mobility (~1×10^{-4} cm^2 V^{-1} s^{-1}).

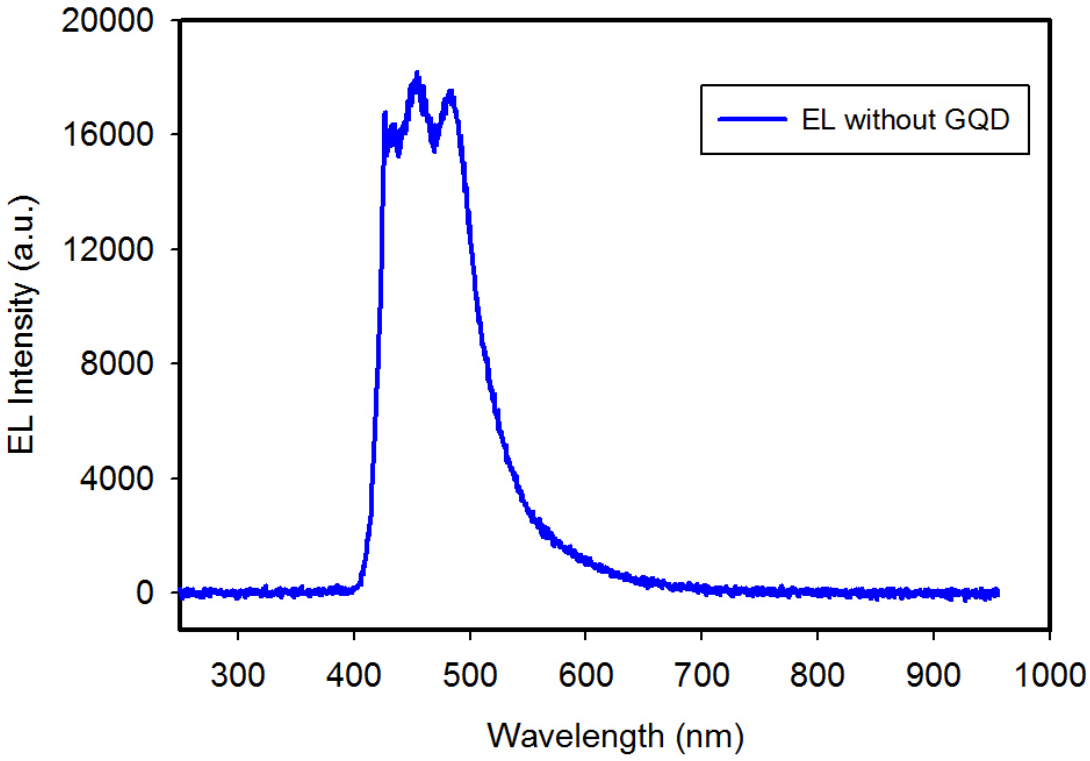

Figure 4.5. The EL spectrum of the OLED with PVK and Poly-TPD as organic emissive layers.

On the other hand, the electron mobility of TPBI as an electron injection layer is 10^{-5} cm^2 $V^{-1}s^{-1}$. The difference at carrier mobility cause more hole concentration in active layer. To make a balance carrier injection, the PVK layer with 2.5×10^{-6} cm^2 V^{-1} s^{-1} hole mobility has been incorporated to prevent holes moving faster than the electrons.

4.3.3.2 OLED with GQD

In this study, emissive GQDs were used as the active light emitting layer within the LED device structure illustrated in section 4.3.3.1. The GQDs chemical and optical properties fully described and investigated in Chap. 3. For device fabrication, all hole/electron transporting

materials have been deposited layer by layer as described before. A thin layer of GQDs was deposited on top of PVK layer from the GQD-IPA solution (1mg/ml) by spin-coating at ~2000 rpm for 30 seconds, followed by drying under ambient atmosphere at 90 ºC for 30 minutes (see Figure 4.6).

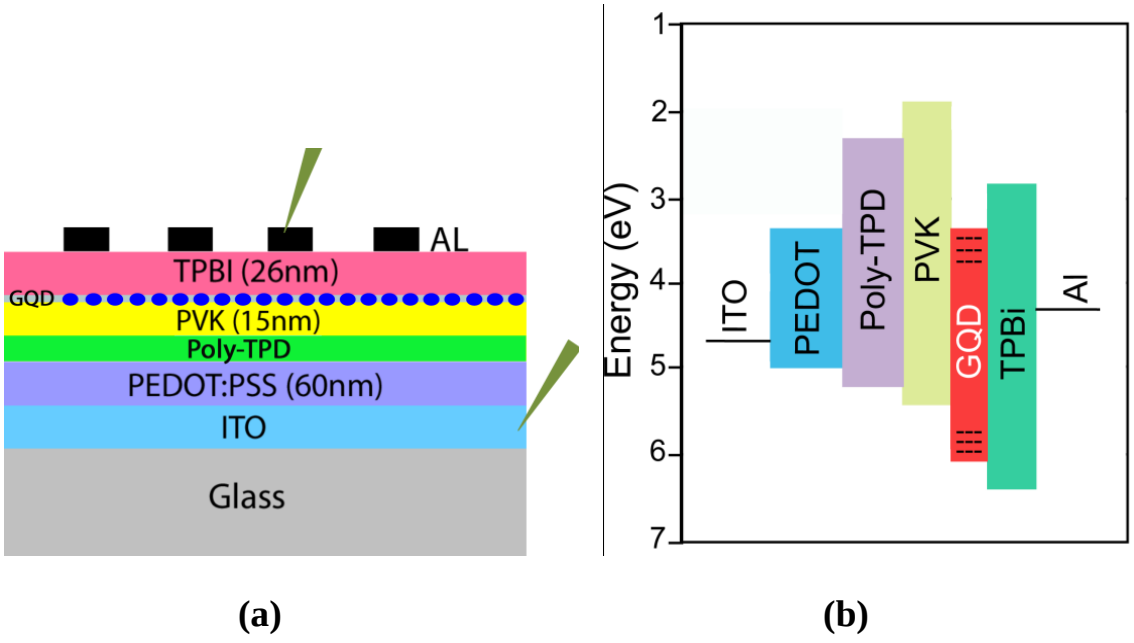

Figure 4.6. (a) OLED structure with GQD as an active layer. (b) Energy band diagram of the OLED structure with GQD layer.

In this GQD-LED device, with the application of electrical forward bias the electron-hole carriers are injected into GQDs layer through the electron transport layer (TPBI) and hole transport layers (Poly-TPD and PVK) respectively. Accordingly, the radiative recombination of pair electron-holes takes place within the GQDs. For this experiment, we set HP4245 semiconductor analyzer in constant current 30 mA and the integration time of the CW output light in BWTek CCD was 10 sec. To check the reproducibility of the EL spectrum, the GQD-LED devices have been fabricated at different days and their EL has been measured. Figure 4.7

shows the measure EL spectrum of the GQD based OLED. The electroluminescence spectrum of GQD is 83 nm wide (full width at half-maximum) centered near 620 nm. All measurements have been done in ambient air condition.

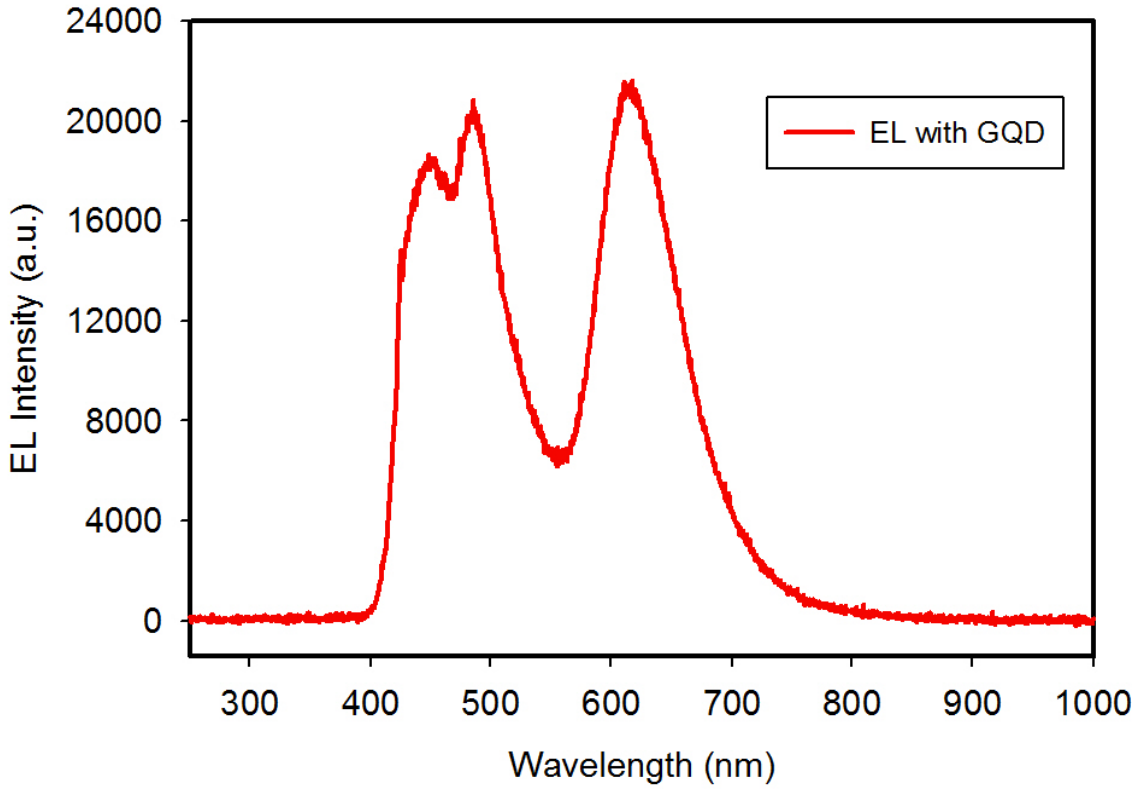

Figure 4.7. The EL emission spectrum of the GQD based LED device.

To differentiate the EL spectrum emitted by embedded GQD from EL spectrum due to other organic layers including Poly-TPD and PVK, we have compared their EL spectrum in Figure 4.8. As the Figure 4.8 illustrates, GQD-LED device has a red emission with peak emission wavelength at 618nm.

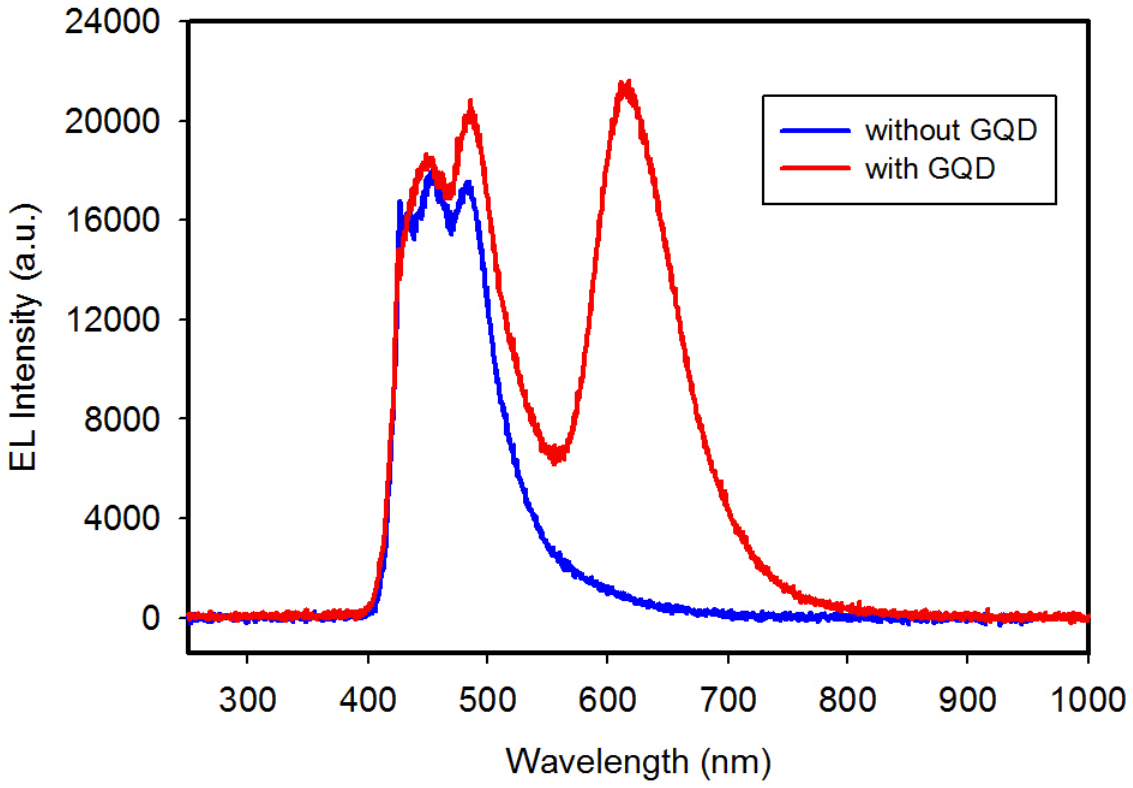

Figure 4.8. The EL spectrum comparison between reference structure (without GQD) and GQD based LED device.

The Kelvin probe analysis indicates that the Fermi level of the GQDs is around 4.74 eV regardless of their sizes between 2 to 10nm [61]. As Ishii et al. has reported the Fermi level position for the bulk organic semiconductor materials could be in the middle of the HOMO−LUMO gap at room temperature [62]. We can directly calculate the GQD energy band gap (Eg) with the help of maximum emission peak wavelength (λmax) in eV [62]. As a result, the absolute energy level of HOMO and LUMO for our GQDs at three peaks emission can be easily calculated as listed in Table 4.3.

Table 4.3. Energy levels of HOMO and LUMO of of the GQDs with size less than 15nm.

Size (nm)	Emission peak (λ_{max}, nm)	Energy gap[a] (Eg, eV)	HOMO[b] (eV)	LUMO[c] (eV)
7[60]	435	2.85	6.16	3.31
7<size<X	496	2.5	6	3.5
X<size<15	618	2	5.74	3.74

[a]Direct conversion of λ_{max} into eV.

[b]4.74 eV + Eg/2

[c]4.74 eV – Eg/2

4.3.3.3 Comparison of EL and PL spectrum of GQDs

In Figure 4.9, the EL spectrum of GQD based LED has been compared to the PL spectrum of the GQDs. The difference between EL and PL spectrum is due to different mechanism of charge carrier transition leading to PL and EL spectra. As the Figure 4.9 represents, the charge carriers transition is occurring between different energy levels within the GQDs.

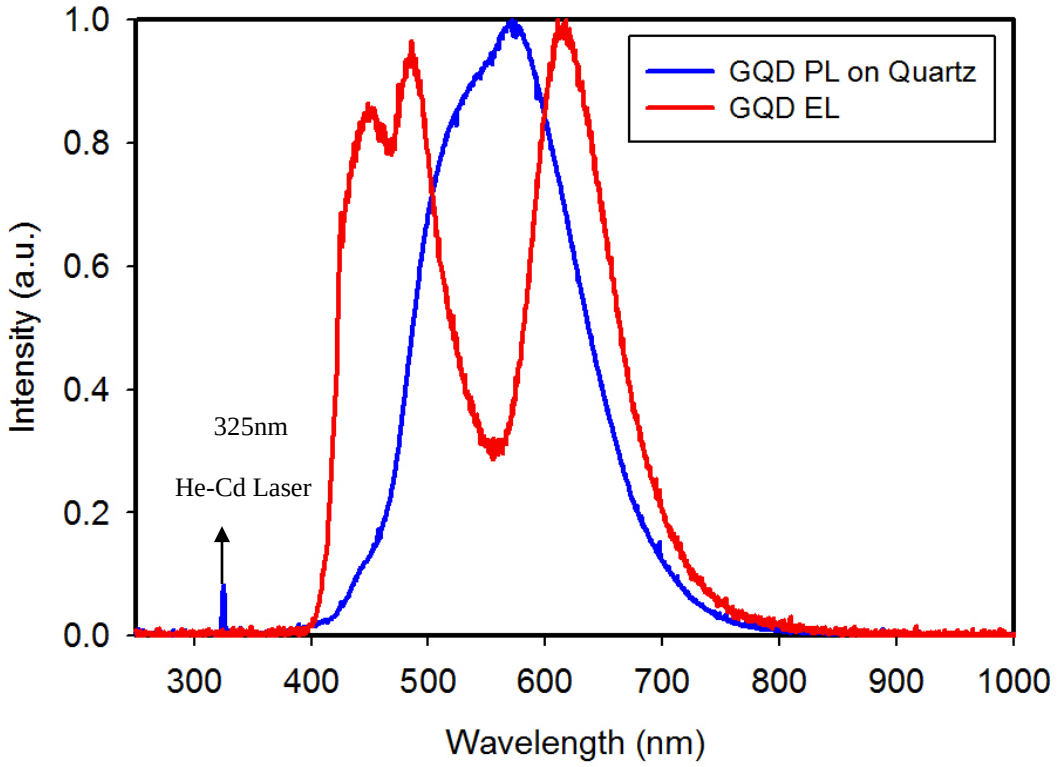

Figure 4.9. Comparison between PL and EL spectrum of GQD

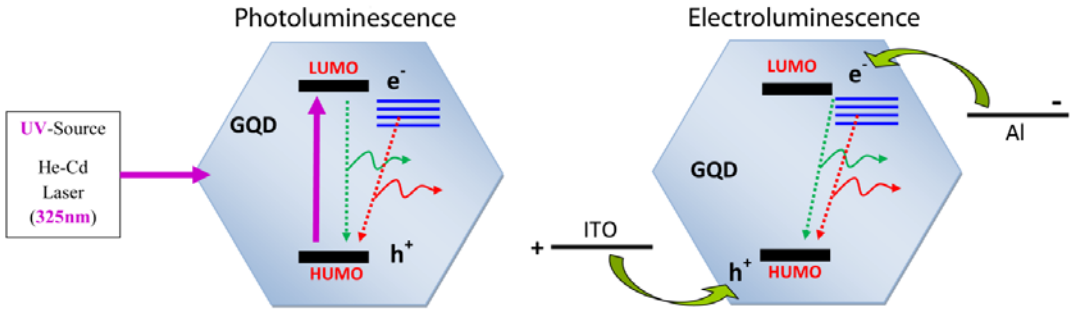

Figure 4.10. Charge carriers transition mechanisms for the both PL (left) and EL (right) in GQDs.

4.3.3.4 LiF buffer layer effect

As in Figure 4.6b is shown, the potential barrier between Al cathode and TPBI as electron injection layer is about 1.5 eV which is large for electron injection. The device with pure Al cathode can be significantly improved by inserting an ultrathin (~1.7nm) of Lithium fluoride (LiF) between TPBI and Al as shown in Figure 4.11 [63]. LiF is a remarkable insulating material with high band gap energy of 12 eV. However, an ultrathin LiF backed by Al cathode becomes an efficient electron injection material in OLED application.

One reason is tunneling injection from Al to TPBI in the presence of a thin layer LiF. As reported in the literature, interposing a tunneling barrier in polymer based device will be increasing the quantum efficiency [64]. The other mechanism that can contribute is the energy band bending at the interface of TPBI and LiF. The energy bands of TPBI were bent downwards when the TPBI surface is in contact with LiF, hence considerably lowering the potential barrier height between Al and TPBI [63,65].

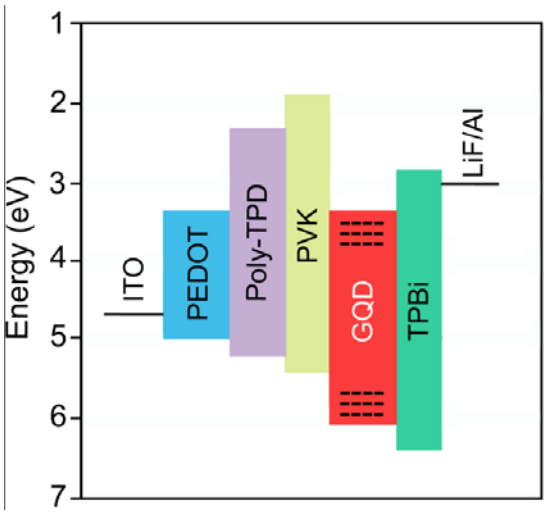

Figure 4.11. Alignment of Al work function by adding LiF

As the Figure 4.11 shows, this layer significantly increases the electron injection due to low offset voltage between cathode and TPBi. As a result, the EL efficiency has been intensified due to more carrier recombination. The EL spectrum, Figure 4.12, has been measured at the same measurement condition that we applied for the device without LiF (constant current 30 mA and the integration time 10 sec.)

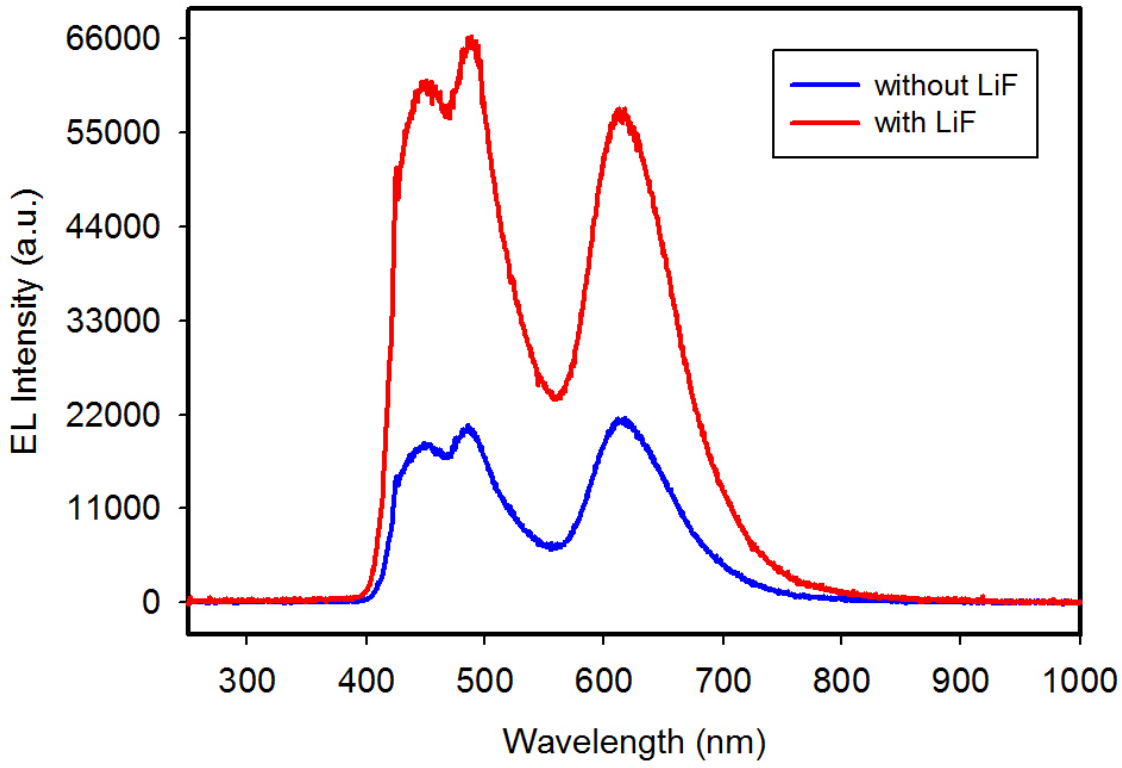

Figure 4.12. EL comparison of OLED devices with LiF and without LiF buffer layer between Al and TPBi.

4.3.4 I-V characteristic

The current density versus voltage characteristic for two structures including OLED with embedded GQDs and without GQDs have been measured and are shown in Figures 4.13. As the Figure clearly illustrates, the current density for GQDs based OLED is much higher than the device without GQDs. The reason is that, the GQD active layer will consume the injected pair hole-electron as a radiative recombination to produce photons. As a result, the amount of carriers injected from tow anode and cathode terminals would be increased which results in higher current density. The other conclusion that we can draw from the I-V characteristics is the effect of LiF on current density. As we expected, adding LiF buffer layer not only can facilitate the hole injection from the Al cathode by decreasing the offset voltage barrier between Al and TPBi, but also it will decrease the operating voltage.

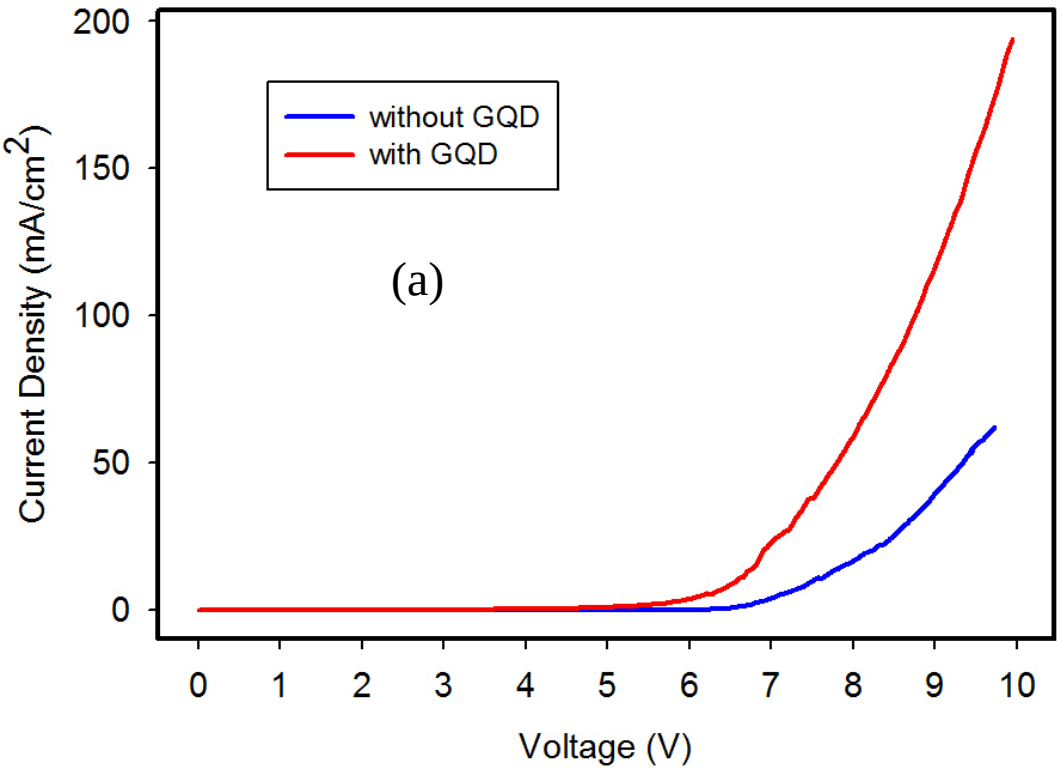

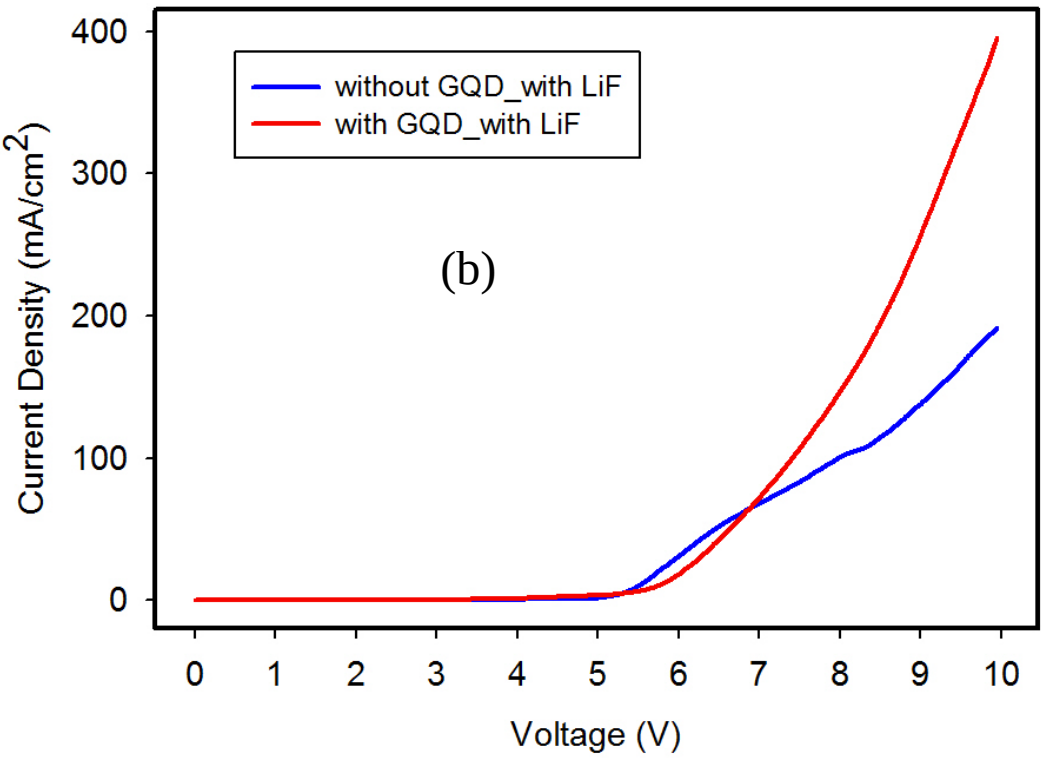

Figure 4.13. The I-V characteristics for (a) device without LiF, and (b) with LiF

4.3.5 GQD EL emission in a very simple structure

To remove EL emission originates from Poly-TPD and PVK layers and see the net emission from GQD active layer we embedded GQD in a very simple LED structure (Figure 4.14). In this device, we skipped Poly-TPD and PVK hole transport materials and the one time spin coated GQD layer is sandwiched between PEDOT:PSS and TPBI. As the Figure 4.15 shows, the EL spectrum from this structure multiple peaks composed of two major peaks at 435nm and 496nm and a shoulder around 600nm.

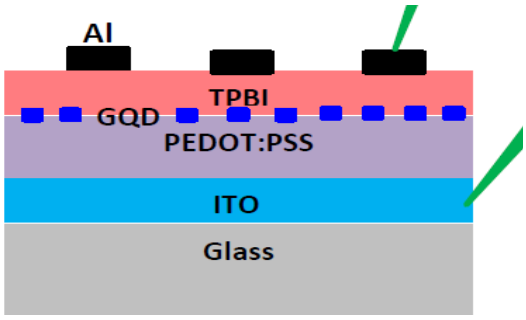

Figure 4.14. LED structure with GQD between PEDOT:PSS and TPBI

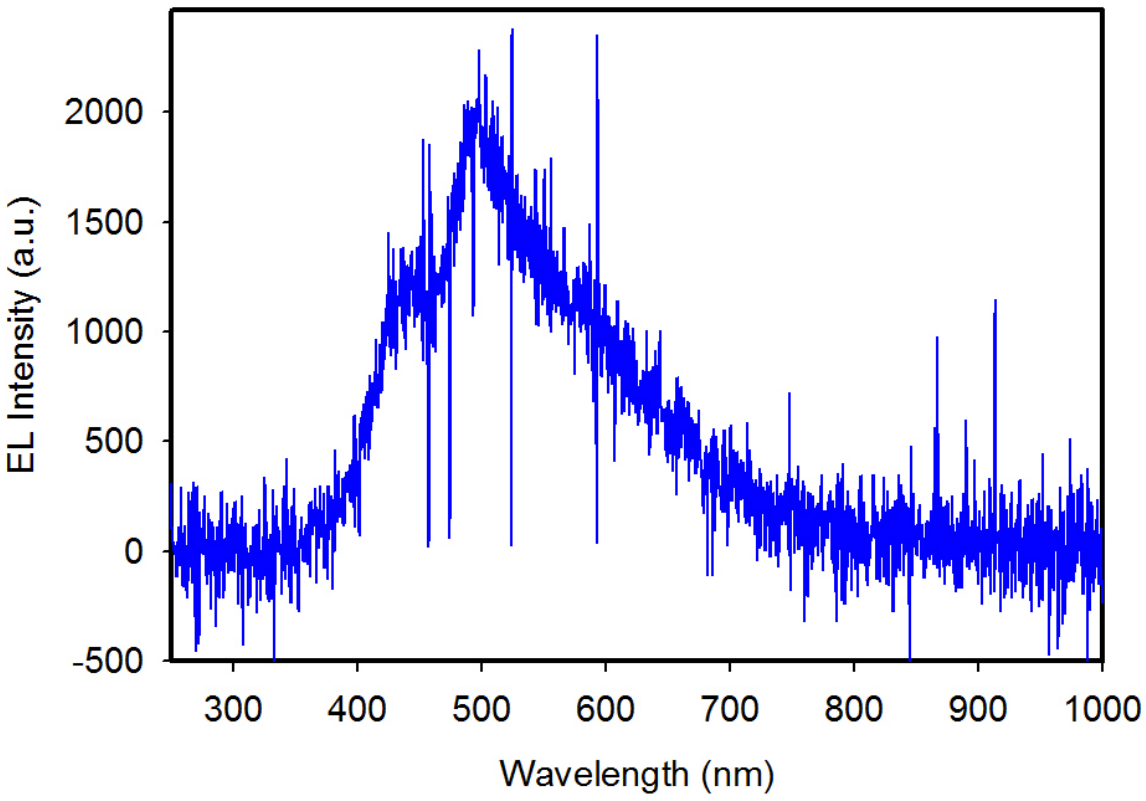

Figure 4.15. The EL emission from GQD layer sandwiched between PEDOT:PSS and TPBI (20 sec. integration time).

The PL of one layer GQD spin coated on quartz substrate and EL of GQD (as shown in Figure 4.15) are compared and shown in Figure 4.16. The PL and EL spectra of GQD are nearly matched and indicate the GQD emission at three different peaks.

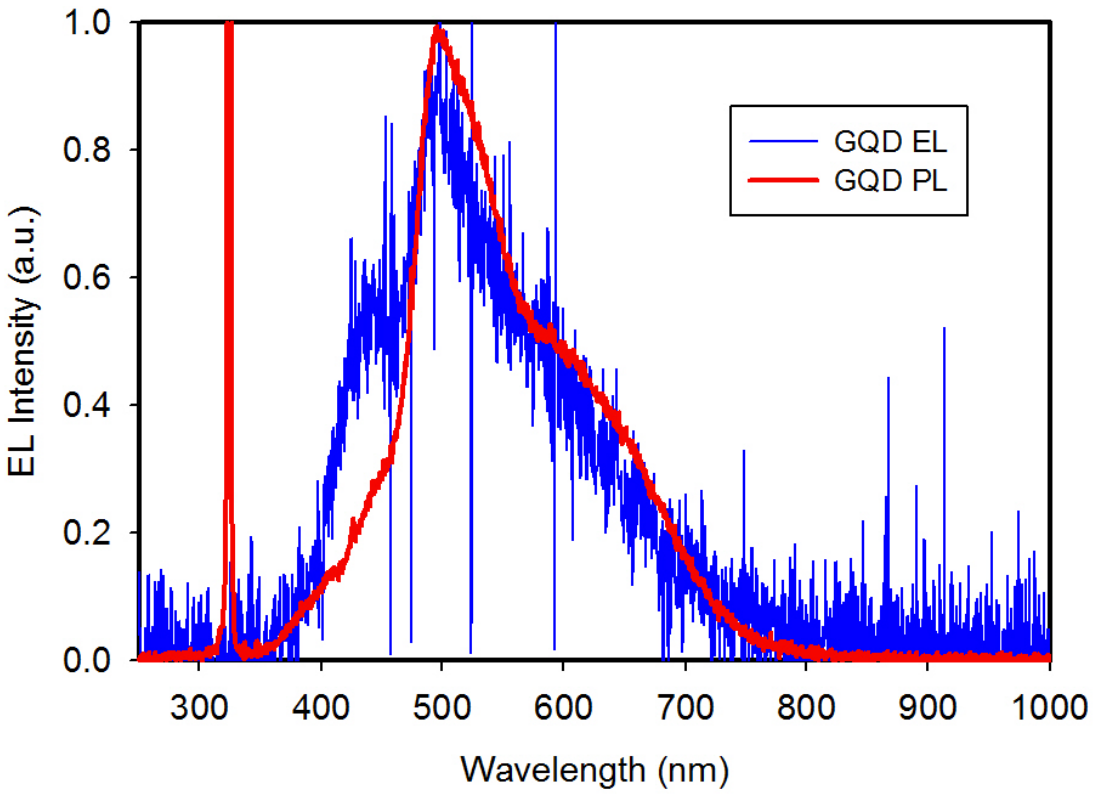

Figure 4.16. A comparison between PL (one layer coated on quartz) and EL (measured in a simple structure) of GQD.

By comparing Figure 4.15 and Figure 2.10b (from Chap.2) , we can say that the GQD EL spectrum at 435 and 492nm has overlap with EL of Poly-TPD and PVK in this region. Consequently, we are not able to differentiate GQD EL spectrum in blue and green area from EL spectrum produced by Poly-TPD and PVK. To confirm that the measured EL spectrum shown in Figure 4.15 is not originated from TPBI or PEDOT:PSS, the LED, we skipped the GQD active layer as shown in Figure 4.17.

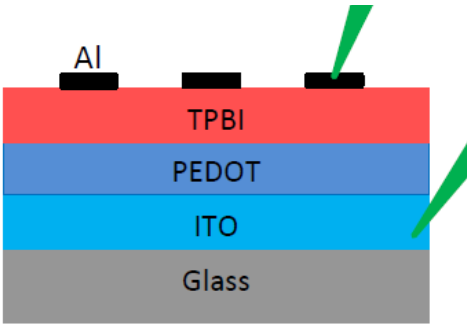

Figure 4.17. Device structure without GQD as an active layer

The EL testing has showed that, there is no emission from TPBI and PEDOT:PSS (see Figure 4.18). By this simple measurement we can strongly confirm that the EL spectrum shown in Figure 4.15 is only originated from GQD layer.

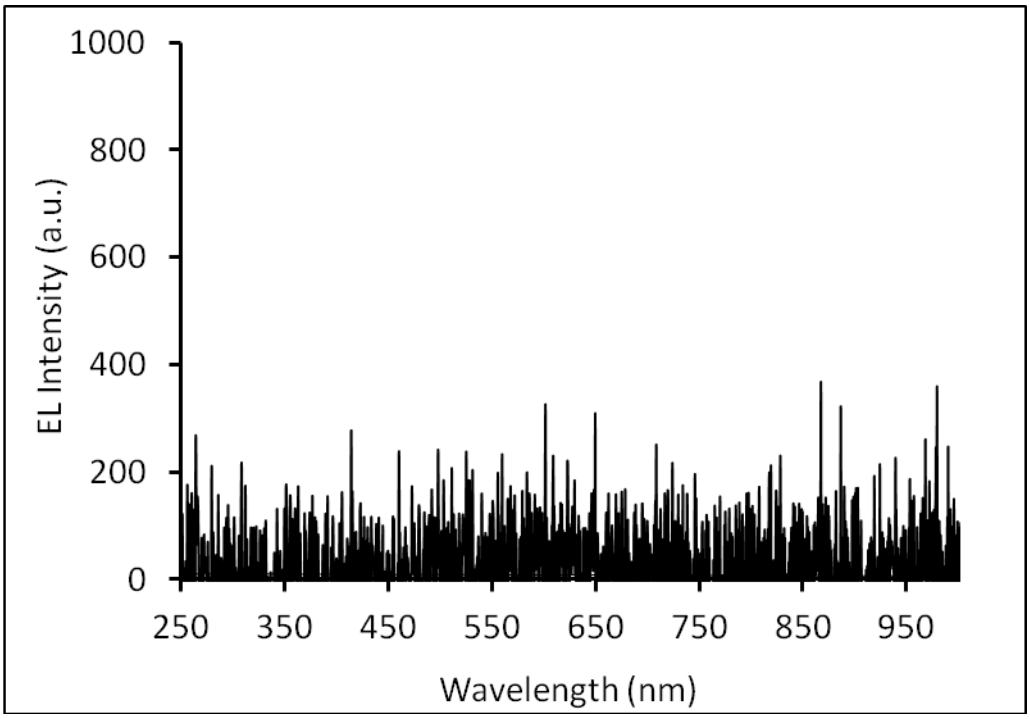

Figure 4.18. The EL spectrum of device structure including PEDOT:PSS and TPBI organic layers without GQD.

5.0 TOP EMISSION GQD-OLED

5.1 SUBSTRATE

Although ITO is widely used as anode in OLED devices, it has some drawbacks which are investigated and reported in the literature. Some of these disadvantages are defect formation on the ITO surface shown by scanning electron microscopy, indium diffusing into the organic materials, being inefficient in hole injecting into the organic layers [56,66-71]. Adding some materials as hole injection and transporting between ITO and active layer and also doing surface modification of ITO can minimize those negative effects of the ITO [72-77]. To overcome and remove the disadvantages of ITO substrate, in this study, we have introduced p-type Si as the anode in OLED device structure. The hole injection mechanism of ITO and p-Si substrates as an anode investigated by Zhou *et al.* showed an enhancement in hole injection in OLED device using p-Si compared to the ITO anode [78].Silicon is an attractive material in OLED field of study due to its important role in Si-based optoelectronics. Si wafers not only can be used just as substrate to fabricate inverted top emission OLED [79,80], bus also can be applied as anode substrate to support top emission OLEDs [78]. For the first time, Parker and Kim have reported Si as anode electrode to inject holes into the active layer [81].

5.2 TOP EMISSION OLED WITHOUT GQD

5.2.1 Device structure and Fabrication Process

A single side polished (SSP) P-type (100) silicon wafers with a resistivity of 10-20 Ω.cm has been used as the anodes and substrates. Before fabrication the wafer cleaned by the following process to increase the device performance.

First, wafer is cleaned by acetone, methanol in ultrasonic bath (10 min each) to remove any organic contaminations and greases followed by running DI water. Second, by RCA cleaning technique the natural deposited SiO_2 and other possible contaminations have been removed.

In the following steps the RCA are listed:

1- Clean individual wafer pieces with acetone, then methanol for 5 minute in ultrasonic bath. Then rinse the wafer in flowing DI water for 10 minutes.

2- Clean by the mixture of H2O + H2O2 + NH4OH with ratio 5:1:1 [150ml : 30ml : 30ml] at 70^o C for 10 min; then rinse by flowing DI water for 5 minutes

3- Dip in 2% HF solution for 15 sec and rinse with DI water for 1 minute

4- Clean by the mixture of H2O + H2O2 + HCL with ratio 6:1:1 [150ml : 30ml : 30ml] at 70^o C for 10 min; then rinse by running DI water for 5 minutes

5- Do Nitrogen blow dry and store the wafer in cleaned plastic container

The Al backside was deposited by thermal evaporating system at 1.1×10^{-5} with $3A^o$/min deposition rate. And then, annealing (N_2 ambient) at 350^oC for 30 min is done to form Ohm contacts on their backsides. The hole and electron transporting materials are prepared as

described in Chap. 2. In spite of bottom emission OLED, the PEDOT:PSS solution is only mixed with 0.25% Triton to increase its adhesion property and the post treatment process is skipped. All organic materials were deposited one by one as illustrated in Chap.4 on *p*-type Si as anode substrate.

For a top emission OLED, the output light comes from the top side so the cathode should be transparent. In this experiment the ITO is used as cathode to inject electrons to the TPBI hole transport layer. The ITO electrodes were deposited by RF magnetron sputtering unit. The sputter target used for this deposition was a source composed of 90% In_2O_3 and 10% SnO_2, disc shape with 2-inch diameter and 0.25-inch thickness. The sample was mounted with 2 inch distance from the target source. It is worth mentioning that to minimize the energetic ion damages to the underlying polymeric layers, the radio frequency power need to be controlled precisely. Under this condition process, the deposition rate is in range of several angstroms per second. In our experiment, about 90 nm ITO has been deposited for 8 min with 11.2 nm/min deposition rate. The experiment condition is illustrated in Table 5.1. A metal mask with circle holes (diameter~1.5 mm) is used to deposit arrays of ITO electrodes.

Table 5.1. Sputtering Parameters for ITO deposition

Target	ITO
Sample	SiO_2(23nm)/p-Si
Gas	Ar
Ar gas flow time	10 mTorr pressure 10 minute
Forward Power	30 W
Distance from target to sample	2 inch
Temperature	Room temp
Vacuum pressure	2.5E-5
Pre-sputtering time	10 min

5.2.2 Broad area p-Si with native oxide

The wafer used in these experiments is p-type (100) silicon with a resistivity of 10-20 Ω.cm. The p-Si (100) substrate is rinsed by acetone, ethanol, followed by ultrapure de-ionized (DI) water in ultrasonic batch for 10 min each, and then they were cleaned chemically with (H_2O + H_2O_2 + NH_4OH), ($HF:H_2O$), and (H2O + H_2O_2 + HCL) solution. After each step, the wafer is rinsed by DI water. Finally, the wafer is dried by nitrogen gas blow. It is worth mentioning that 2% HF solution for 15 sec is used to remove the old native oxide grown on the surface during time. Morita et al. investigated native oxide film thickness grown on different wafers measured by x-ray photoelectron spectroscopy (XPS) combined with ellipsometry [82]. Figure 5.1 shows their determined native oxide thickness on silicon substrate as a function of exposure time at room temperature. As the Figure indicates, the initial native oxide for p-type Si is about 2.3Ao which is grown during rinsing and drying process by DI water and N2 gas, respectively [82]. In our study, the p-type Si is left in ambient air condition for 24 hours after cleaning process. According to the Figure 5.1, the estimated native oxide grown on the surface should be around 6A^o (0.6nm).

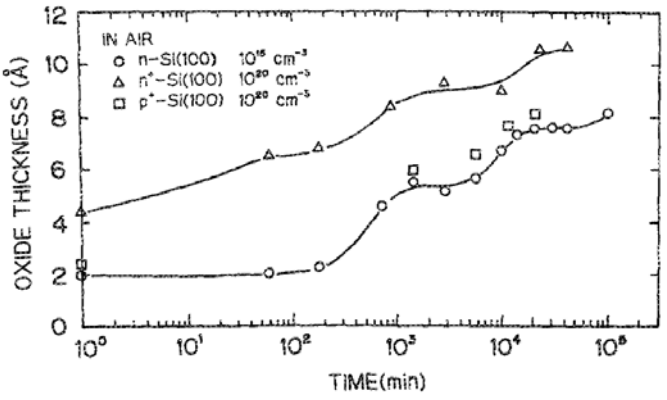

Figure 5.1. Native oxide thickness grown on wafer as a function of exposure time in air temperature [82].

The very thin native oxide layer will increase the hole injection from p-Si through the active layer by aligning the Fermi level of the electrode with the valance band of the PEDOT:PSS [81,83]. As a result, the probability of radiative recombination in active layer would be increased. In Figure 5.2a, the structure of the fabricated OLED has been shown. In this reference structure Poly-TPD and PVK play as emissive layers. PEDOT and TPBI are chosen as hole transport and electron transport material, respectively. The energy band diagram for this device is illustrated in Figure 5.2b. By applying forward bias voltage, the holes are injected from the Al anode through the p-type Si and accumulate in active layers. The large band gap of TPBI by very low HOMO energy level block hole carriers and increase their density in the middle part. Besides, the small potential barrier between p-Si and PEDOT layer facilitate the hole injection. Similarly, electrons are injected from ITO electrode as cathode to the active layers. The large amount of LUMO energy of PEDOT blocks the electrons injected to the ITO. Choosing suitable hole-electrons transporting and blocking materials enhances the carrier injection and confinement in the active layer.

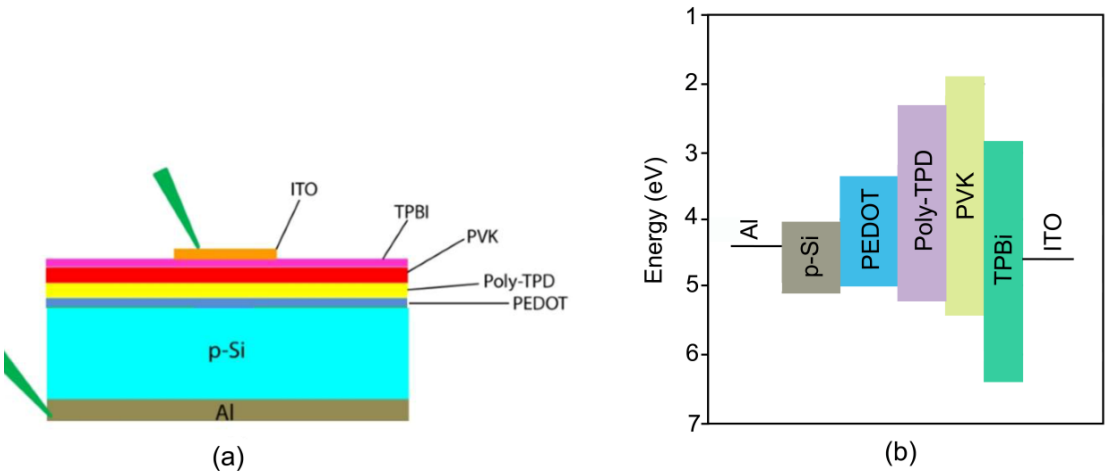

Figure 5.2. (a) The OLED structure with organic layers on p-Si substrate and (b) energy band diagram for different layers of this device.

It is well known that the by controlling the work function of p-Si as an anode substrate, we can tune the amount of hole injected carrier concentration and thereby the carrier balance within active layer. As a result, the efficiency and OLED performance can be improved [84,85]. In Figure 5.3, the energy band diagram for p-Si and PEDOT:PSS are shown. The Fermi level in bulk p-Si is 4.97ev, 0.2ev above the valance band with 5.17ev value, because of the doping concentration in the bulk region. However, the surface Fermi level is pinned at 0.3ev above the valance band in this region (5.27eV) [86]. The 0.1eV band bending barrier occurred between surface and bulk region results in only 0.1eV offset voltage as a effective barrier for hole injection through p-Si to PEDOT:PSS.

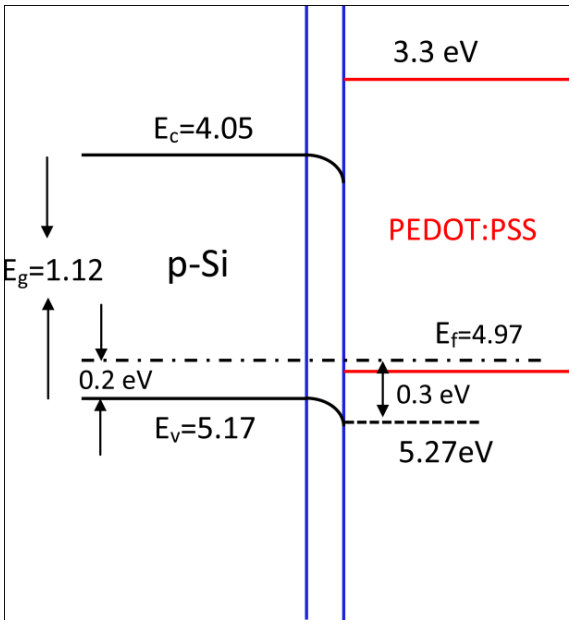

Figure 5.3. Band diagram of p-Si and PEDOT:PSS at the interface

5.2.3 Broad area thin SiO_2 on p-Si without GQD as an active layer

In this section, SiO_2 with different thickness as a buffer layer is grown on p-Si substrate. Researchers have determined the energy band profile of p-Si/SiO_2 at the interface for the thick oxide by an internal photoemission technique [82]. Although Dressendorfer et al. reported that the barrier height for the thick and thin oxide are same [82], the other experiments by other groups had reported various values of offset voltage for ultrathin 1.8-4.5nm oxide thickness [87-92].

5.2.3.1 Thin layer oxide grown on p-Si

To investigate effect of thin oxide interface between p-Si and PEDOT:PSS in OLED performance, thin buffer layer SiO_2 with different thickness (2, 5, and10 nm) has been grown on p-Si by dry thermal oxidation. The oxidation process for thin oxide calibratedin our Lab is shown in Table 5.2.

Table 5.2. Thin oxide growth condition on p-Si

Temperature (°C)	832°C	832°C	832°C
Oxidation time (min)	1min	15min	40 min
Expected thickness (nm)	2nm	5nm	10 nm

In Figure 5.4a and b, the device structure with SiO_2 thin layer as a buffer and energy band diagram of this OLED has been shown. With the application of a forward bias voltage, the holes

are injected from the Al anode through the p-type silicon and they tunnel through the oxide to the organic emission materials including PVK and Poly-TPD. Similarly, electrons are injected from the top ITO as a cathode and travel through the TPBI electron transporting layer to the emissive layer. The 0.9eV offset voltage in HOMO level between PVK and TPBI can block holes and increase the carrier confinement in the emissive layer. Likewise, the thin oxide layer blocks the transported electrons from ITO and confines them in the active layers. As a result, the hole carrier will recombine radiatively in the active layer and the corresponding light will be emitted by this structure.

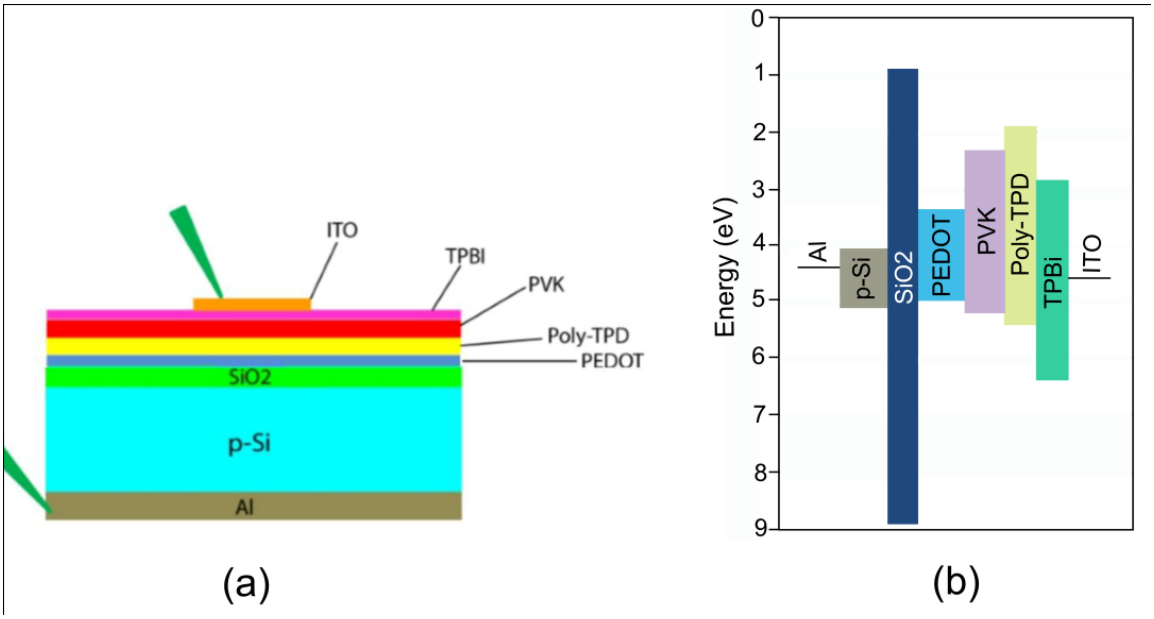

Figure 5.4. (a) OLED structure with a thin layer SiO_2 and (b) energy band diagram of this device.

To have an estimation of a tunneling current through the thin buffer oxide sandwiched between p-Si anode substrate and PEDOT:PSS hole transport layer, we need to have a precise

energy band diagram at the p-Si/SiO_2 interface. Although many studies have been done to determine the energy band profile of ultrathin SiO_2/Si, different values for valance and conduction band have been reported. In 1977, Alay and Hirose have reported for thin SiO_2 thickness range from 1.6 to 3.5nm grown by dry thermal oxidation, the hole/electron barrier height remained in constant value [93]. Similarly, Zhang *et al.* proved that for 2 nm oxide the work function (WF) of p-Si anode would be enhanced by ~0.6 eV [94]. By knowing that the valance band alignment or hole barrier height is constant regardless of the oxide thickness, we can safely claim that for various ultrathin SiO_2/p-Si interface the p-Si work function (WF) increases up to 0.6 eV (Figure 5.5). Consequently, the increased WF results in smaller offset voltage (barrier height) for holes and enhances the device efficiency due to the carrier balance made in the active layer. In energy band diagram which is shown in Figure 5.4 (b), the interface effect between p-Si and SiO_2 has been neglected and flat band energy diagram is drown.

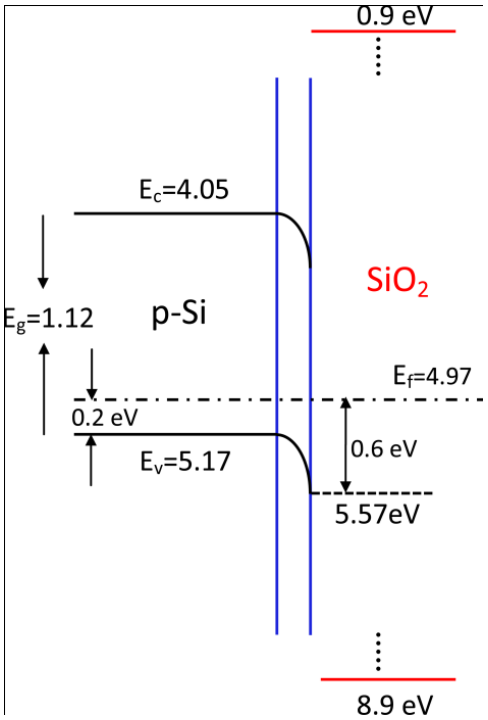

Figure 5.5. Energy band diagram at the p-Si/SiO_2 interface

Furthermore, the heavily doped Si shows metallic properties. With ultrathin SiO_2 buffer layer, the passivated SiO_2/p-Si anode exhibits semiconductor properties by changing in electronic structure which play a critical role in hole injection property [81]. In fact, the semiconductor properties of SiO_2/Si interface are due to the trade-off between metallic Si and insulating SiO_2 [95,96]. To illustrate, as described in section 5.2.1.1, the interfacial band structure modification between p-Si anode contact with the hole transport organic layer (PEDOT:PSS) would tune the hole carrier density injected from the modified p-Si through organic layer [84]. The other important role of the oxide layer is blocking the electrons that come from the ITO cathode which results in higher carrier confinement in the active layer. Consequently, the probability of radiative recombination would be increased.

5.2.3.2 Electroluminescence Measurement

In Figure 5.6 a top view image of one OLED pixel with 1.5mm diameter is shown. To operate device, one tungsten probe tip with 10μm size is connected to the top ITO electrode as cathode which injects electrons through the device. The other probe is connected to the bottom Gallium in which p-Si with Al backside as anode electrode attached to it. By applying voltage using HP4245 semiconductor analyzer, the OLED operate and emit light. To record EL spectrum, we collected output light by fiber probe and fed it to VIS-NIR spectrometer. Figure 5.7 shows EL spectra at different thickness.

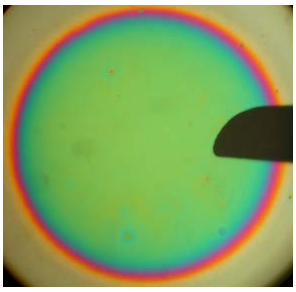

Figure 5.6. Top view image of an OLED pixel.

Table 5.3. EL measurement condition of the OLED device with thin oxide buffer layer

Oxide thickness (nm)	Constant applied voltage (V)	Integration time (sec.)
Native oxide	12	4
2	12	4
5	12	4
10	12	4

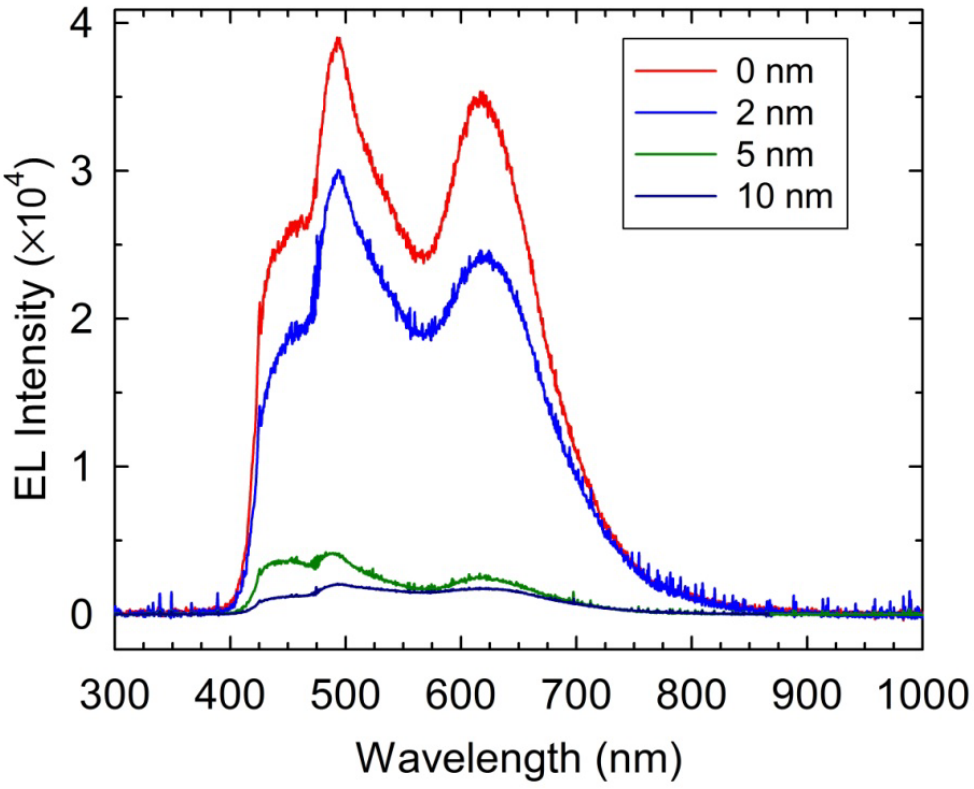

Figure 5.7. The EL spectra for OLED with native and grown thin oxide layer (2,5, and 10nm). The applied voltage (CW injection) and integration time of the HP machine were 12V and 4s, respectively.

To investigate oxide thickness effect on OLED performances such EL intensity which represent the device efficiency, the EL spectra have been measure at the determined condition measurement. The applied voltage and integration time are listed in Table.5.3. As the EL spectra in Figure 5.7 shows, by increasing the oxide thickness the intensity peak is decreased. Similarly, the digital photo image indicates in native oxide and very thin layer oxide thickness the output light has more brightness due to the more carrier confinement in active layer (Figure 5.8).

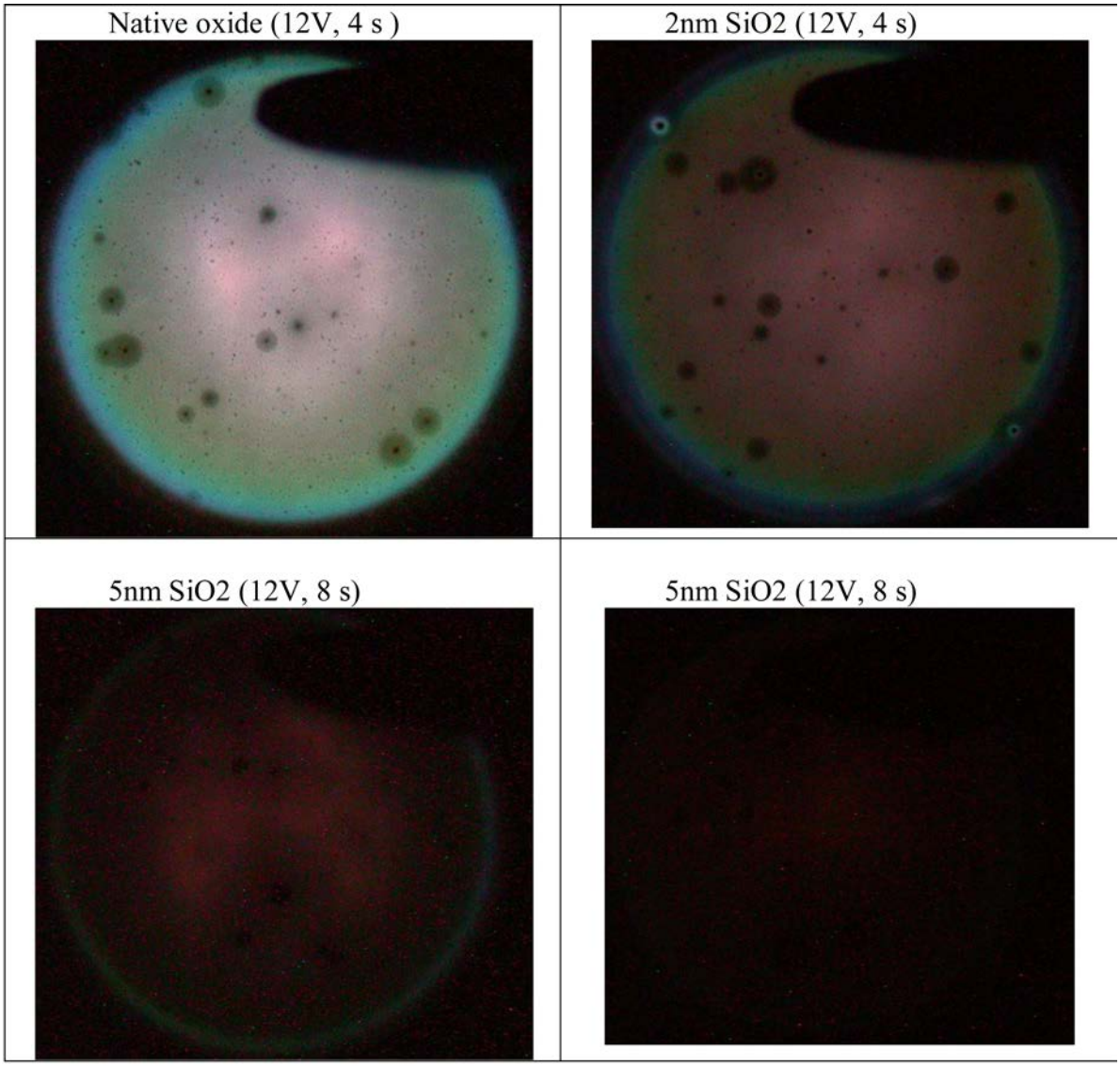

Figure 5.8. Digital image of lamination during CW injection for OLED with different thin oxide as a buffer layer.

5.2.3.3 Direct Tunneling (DT)

Direct tunneling is a quantum mechanical tunneling process that electrons or holes in low band gap material would face a potential barrier when they want to pass to a media with high

band gap potential energy. With the presence of the external electric field, the shape of the potential barrier would be changed in a way that the barrier height (Φ_B) would become larger than the voltage drop across the oxide V_{ox} ($V_{ox}<\Phi_B$). Accordingly, the injected carriers (electrons or holes) would face a trapezoidal barrier which is narrower than the case in the absence of external field [97,98]. As a result, with the application of low oxide field to the MOS structure with thin oxide layer, carriers can directly tunnel the barrier to the next conduction or valance band [99]. This type of quantum tunneling mechanism is called direct tunneling which is dependent on the oxide thickness. As the oxide thickness decreases, the direct tunneling increases exponentially. Equation 2.1 describes the related current density for direct tunneling (J_{DT}):

$$J_{DT} = C.E_{ox}{}^{2} \exp\left(\frac{-B\left(1-\left(1-\frac{V_{ox}}{\Phi_B}\right)^{\frac{3}{2}}\right)}{E_{ox}}\right)$$

Equation 5.1

Where, E_{OX} refers to the field across the oxide, Φ_B the barrier height for electrons, V_{OX} represents the voltage drop in the oxide and B and C are physical parameters [99].

5.2.3.4 I-V characteristic

In forward bias holes are able to tunnel from the p-Si anode into the HOMO level of the PEDOT:PSS polymer. As we described in direct tunneling mechanism, the oxide thickness has a crucial role in J_{DT}. As a result, while the oxide thickness increases, the direct tunneling current density decreases. The current density versus voltage characteristics of the device at different oxide thickness shown in Figure 5.9 clearly illustrates the oxide thickness effect on current density.

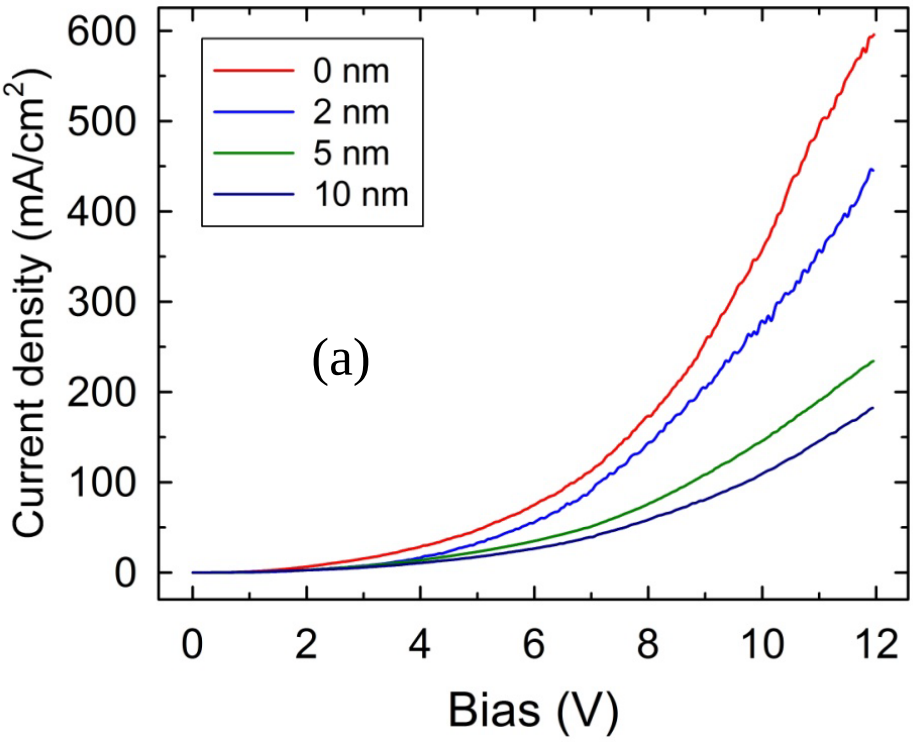

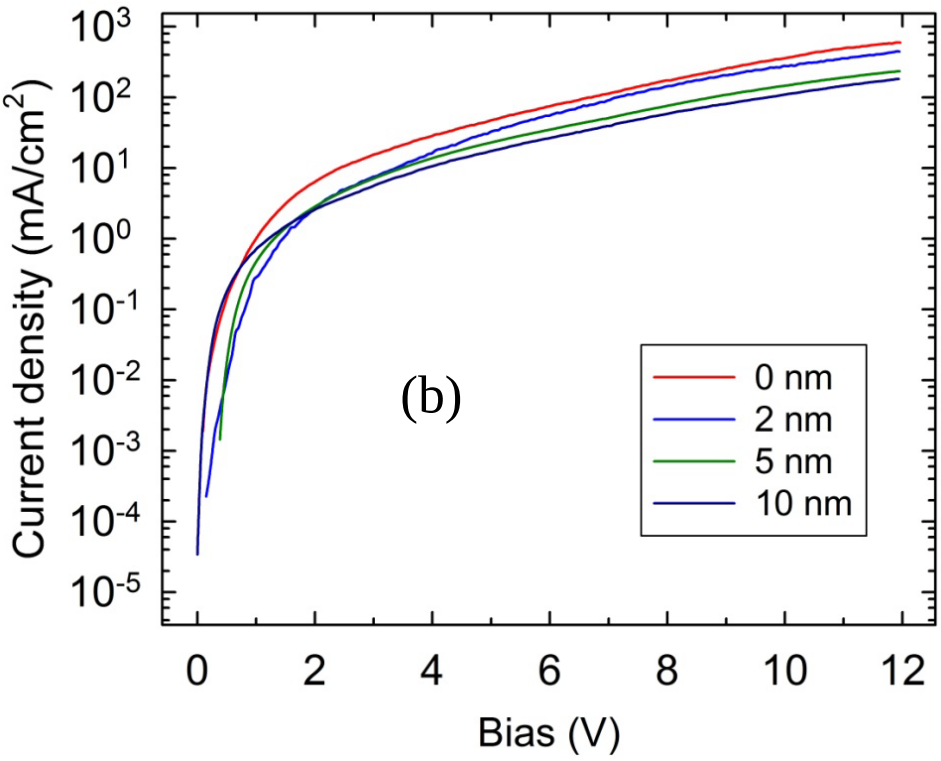

Figure 5.9. The current density vs. voltage of the device with various thin oxide thick thicknesses (the bias injection was 12V). (a) Linear-Linear plot, (b) Log-Linear plot

As Figure 5.9 shows, the very thin layer oxide layer has more current density due to the more direct tunneling of the holes from the p-Si to the PEDOT:PSS.

5.2.4 Broad area thick SiO_2 on p-Si without GQD as an active layer

To localize the output light in a small area, the thickness of the SiO_2 layer has been increased to 23, 50, and 150 nm and then by lithography we have made open windows in oxide. The oxidation condition for these thick thicknesses is shown in Table 5.5.

Table 5.4. Thin oxide growth condition on p-Si

Temperature (°C)	950°C	950 °C	950 °C
Oxidation time (min)	23	110	6h,30
Expected thickness (nm)	23	50	110

5.2.4.1 OLED device without GQDs layer

The device structure and the related energy band diagram have been shown in Figure 5.4. The measured EL spectra and recorded digital photo images of output light are shown in Figure 5.10, and 5.11, respectively. The measurement condition for the EL spectra and digital photo have been shown in Table 5.6, and 5.7, respectively.

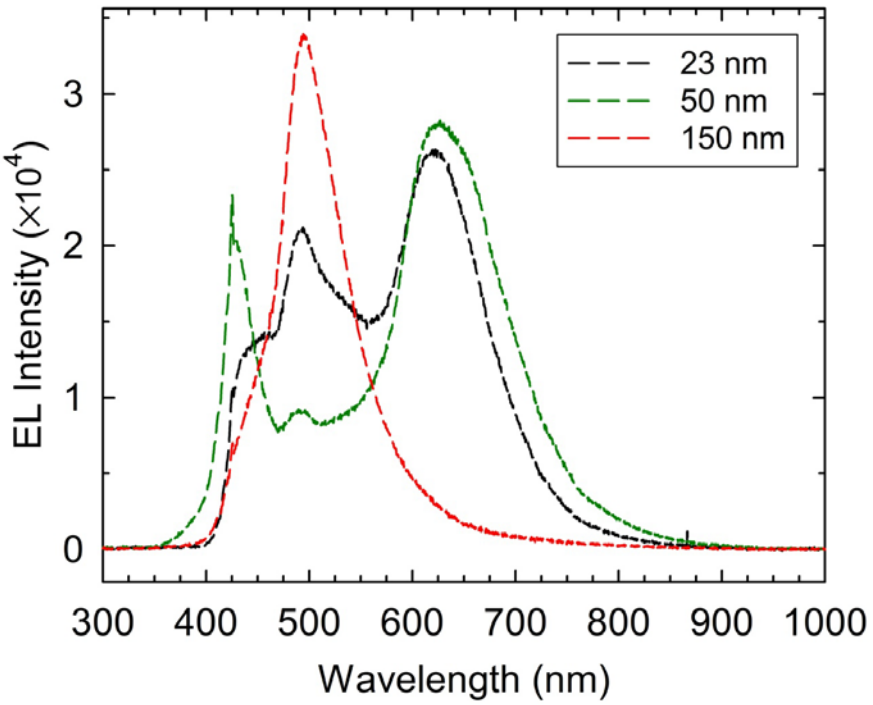

Figure 5.10. EL spectra at different oxide thickness for out of window area of the OLED without GQD. The measurement condition was for 12V CW injection and 4s integration time.

Table 5.5. The EL measurement condition for different oxide thickness

Oxide thickness (nm)	Constant applied voltage (V)	Integration time (sec.)
23	12	4
50	12	4
150	12	4

Table 5.6. Digital photo measurement condition for different oxide thickness

Oxide thickness (nm)	Constant applied voltage (V)	Shutter opening time (sec.)
23	13	2
50	13	2
150	12	1

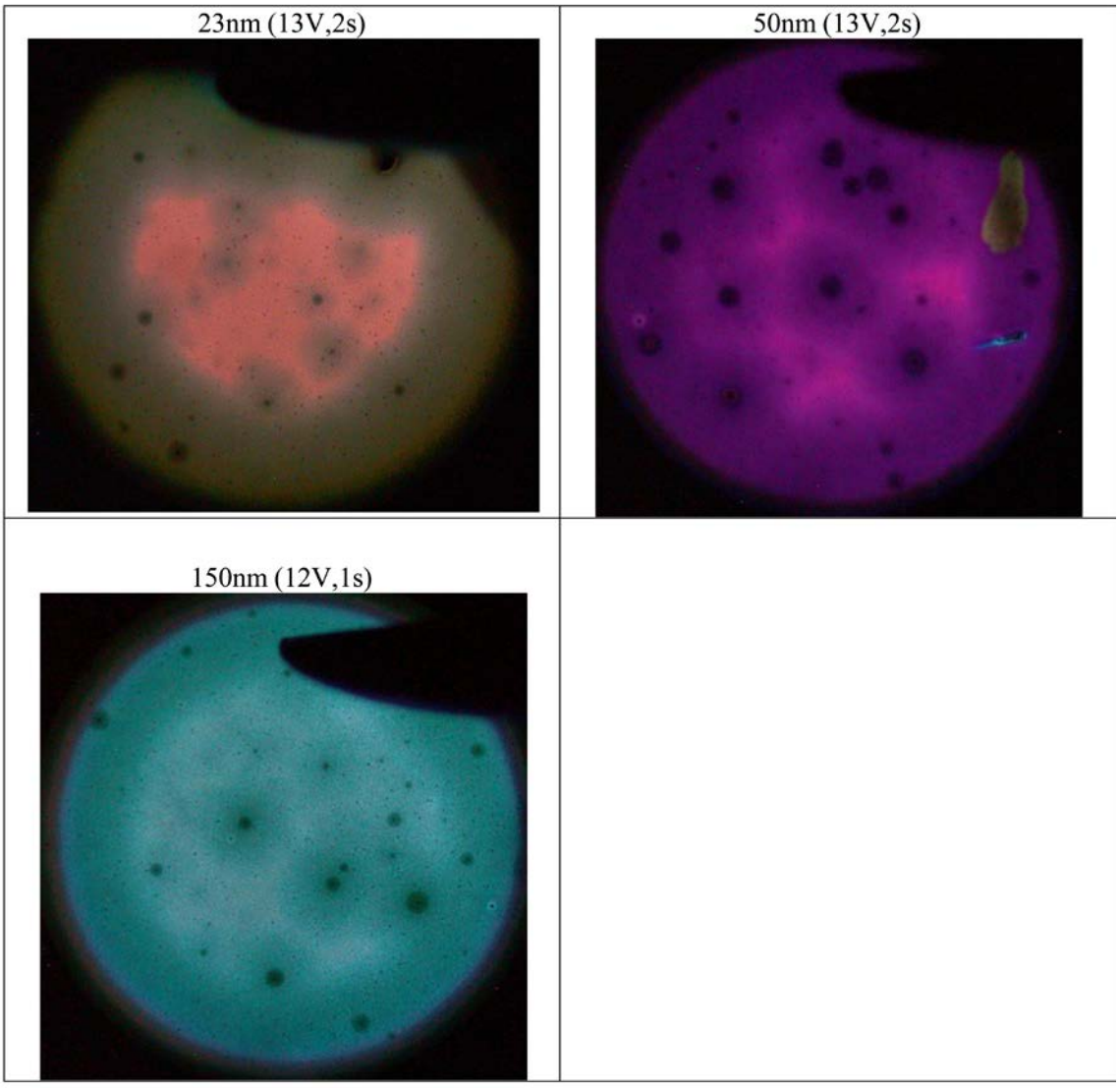

Figure 5.11. Digital image of lamination during CW injection

As the literature reported, the potential barrier height at the SiO_2/Si interface for thick oxide (31 nm and greater) is found to be almost similar to that of ultrathin SiO_2 due to the nearly same values for the valance band density of state (VBDOS) [87,93]. However, the tunneling mechanism for thick oxide is totally different from thin layer oxide.

5.2.4.2 Fowler-Nordheim Tunneling (FNT)

For the thick oxide thickness, holes cannot penetrate through the oxide layer based on the direct tunneling mechanism. The quantum mechanical tunneling process that can describe hole penetration through the thick SiO_2 layer passivated p-Si anode is Fowler Nordheim Tunneling (FNT) mechanism. By applying high voltage and strong external field to the structure illustrated in Figure 5.4 (with thick grown oxide), the valance and conduction band of the oxide layer would be bended in shape of triangular. As a result, the oxide barrier will decrease and become narrower for hole carriers injected from p-Si anode. In other word, the triangular barrier in oxide's valance band gets narrower as the applied voltage and electric field increases [100]. Hence, the hole carrier would tunnel the narrow triangular oxide barrier and reach the next PEDOT:PSS hole transport layer accordingly.

The FNT model for triangular potential barrier can be derived by solving the one dimentional and time independent Schrödinger equation equation [101]. As a result, the related FNT model for thick layer oxidation can be presented by:

$$J_{FN} = \frac{mq^3}{8\pi hm^*\Phi} E_{ox}^2 \exp\left[\frac{-8\pi\sqrt{(2m^*)}\Phi^{3/2}}{3hqE_{ox}}\right] \qquad \text{Equation 5.2}$$

In this equation, m is the free electron mass, m* the effective electron mass in the oxide, E_{ox} the electric field in the insulator, h the plank's constant, Φ the energy barrier height (which is assumed to be independent of the electric field) [102]. As the equation 5.2 explains, the FNT model is dependent on the magnitude of the oxide field and as it increases, the FN current increases.

As the Figure 5.11 shows, the color of the output light is changed when the oxide thickness is increased. The reddish color of the device with 23nm oxide is changed to purplish when the oxide thickness is increased to 50nm. Also, the EL spectra for these two spectra confirm this color changes. The sharp peak around 430nm appeared in OLED EL spectrum with 50nm oxide thickness that is the main reason for this color change from red to purple. Similarly, for thicker oxide (150nm), the color is change to green. The physical principle of this phenomenon is that the band bending for thicker oxide is larger than the thinner one even at same applied voltage. As a result, only holes with high energy can reach the narrow part of the oxide band and penetrate through the oxide according to the FNT mechanism. These high energy holes have sufficient energy to excite electron-holes from HOMO/LUMO of the molecules with high energy gap. Thus, the emission wavelength is blue shifted for higher oxide thickness and the color is changed accordingly.

5.2.4.3 I-V characteristics

The current density versus applied voltage measurement (see Figure 5.12) for these three devices clearly indicates the FNT tunneling mechanism when we apply high external field. As the Figure shows, the tunneling was started at around 9V. The current density for 23nm oxide thickness is more than 50nm and 150nm oxide thickness. The reason is that for higher thickness the population of holes (accumulation population) is less than for thinner thickness. In fact, at thicker oxide we have high energy holes with less population.

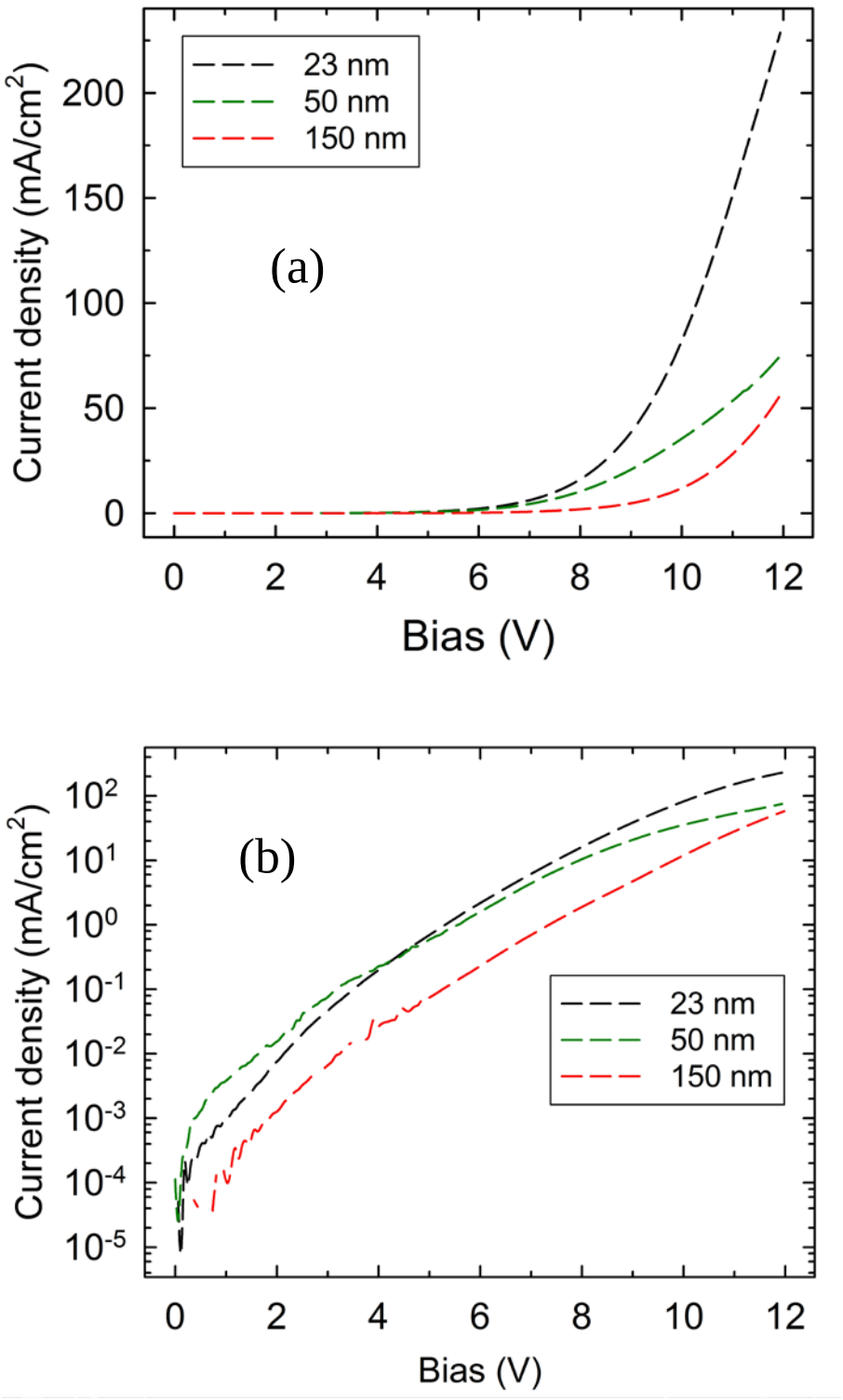

Figure 5.12. The current density vs. voltage in OLEDs with various oxide thickness. (a) Linear-Linear plot, and (b) Log-Log plot.

5.2.5 Patterned SiO_2 on p-Si

The photo lithography was carried out by spin coating a 3µm thick 1827 positive photoresist (P.R.) at 3000rpm for 30 sec on SiO2 layer grown on p-type silicon substrate. The photoresist was then baked at 90^{o}C for 30 minutes in an oven. Then, patterns with square shape were exposed on photoresist by Karl Suss MJB-3 mask aligner in constant power mode preset at 195 watts for 17 minutes. After exposure the photoresist resist was developed in 20% Microposit 391 developer for 2 minutes to obtain the patterns as desired. To etch the developed area, using wet etching technique by BHF etchant the oxide in the opened region was removed. The remained photoresist has been removed by acetone, methanol followed by DI water. The process is illustrated in Figure 5.13.

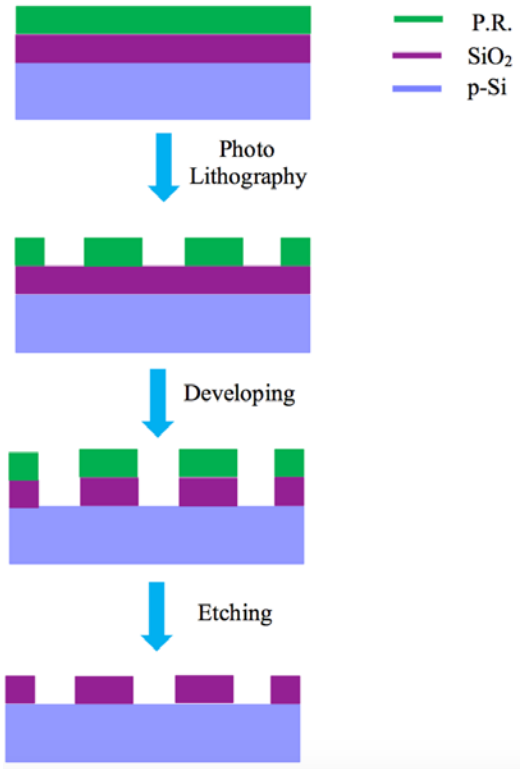

Figure 5.13. Photolithography process to make window in oxide.

After preparing the substrate with window patterned to localize the electron pathway which are injected from p-Si as cathode electrode, all other organic layers have been deposited based on mentioned condition in previous sections. Figure 5.14 shows the stacked organic hole/electrons transporting layers and top view of the fabricated device with sputtered ITO as an anode on top.

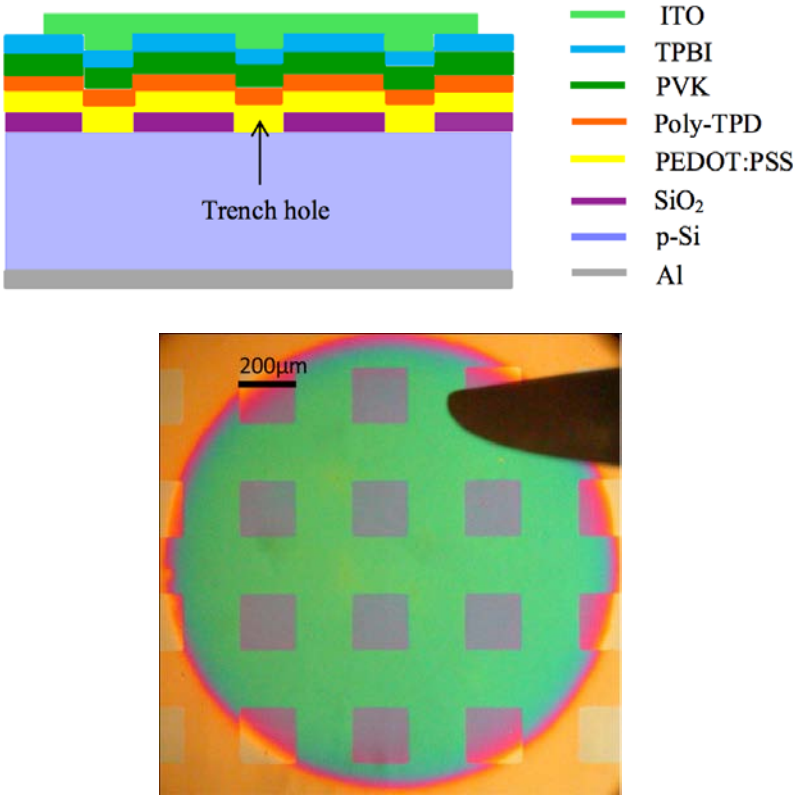

Figure 5.14 a) Schematic showing the side view of the OLED, b) Top view of the fabricated OLED

The device structure and the related energy band diagram is shown in Figure 5.15. The measured EL spectra and recorded digital photo images of output light are shown in Figure 5.16, and 5.17, respectively. The measurement condition for EL and digital photo have been shown in Table 5.8, and 5.9, respectively.

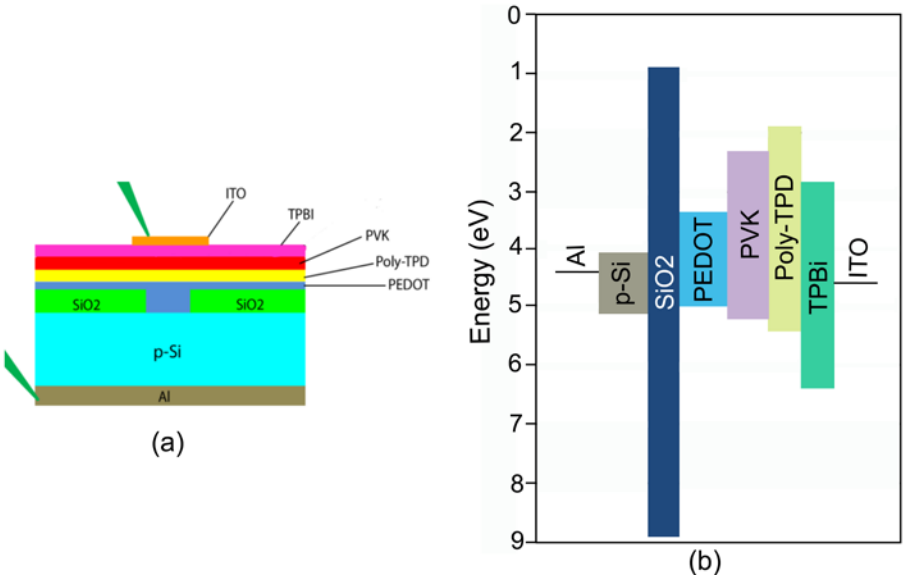

Figure 5.15. (a) The OLED structure, and (b), the energy band diagram of the device

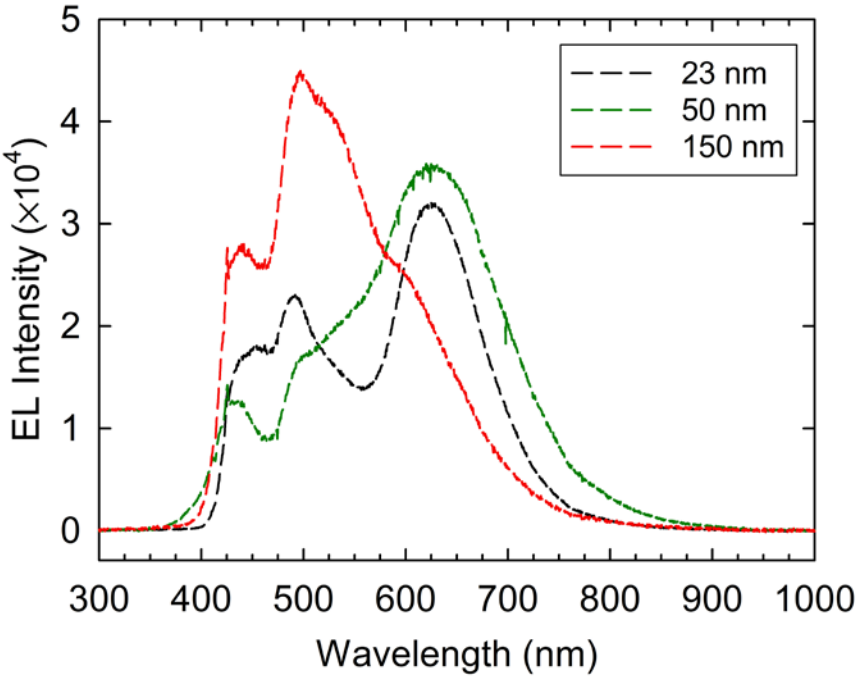

Figure 5.16. EL spectra at different thick oxide thickness

Table 5.7. The EL measurement condition for different oxide thickness

Oxide thickness (nm)	Constant applied voltage (V)	Integration time (sec.)
23	12	4
50	12	4
150	12	4

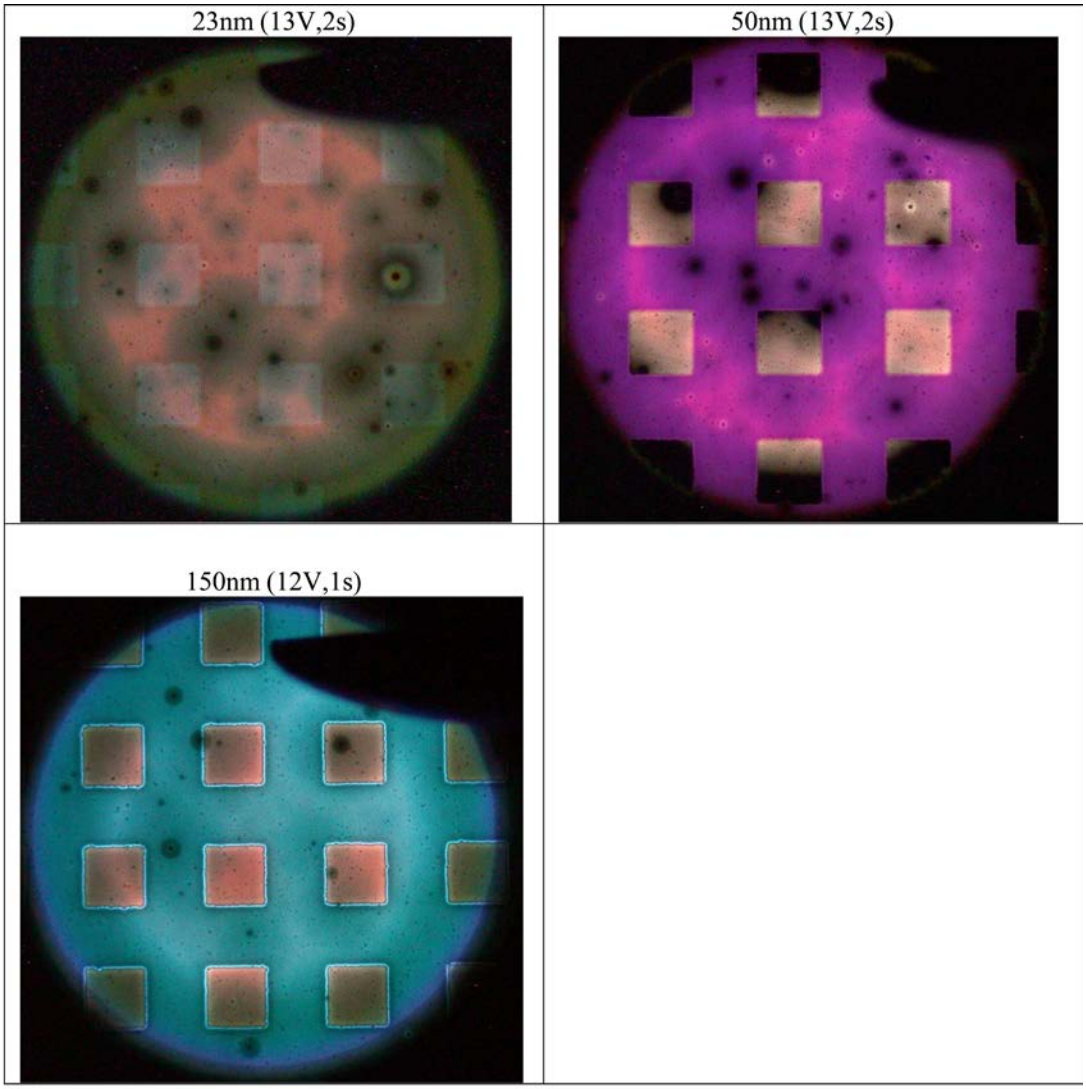

Figure 5.17. Digital image of lamination during CW injection for OLED (without GQD) with different thick oxide between p-Si and PEDOT:PSS.

Table 5.8. Digital photo for different oxide thickness

Oxide thickness (nm)	Constant applied voltage (V)	Shutter opening time (sec.)
23	13	2
50	13	2
150	12	1

The I-V characteristics measurement for these three structure show that by increasing the oxide thickness the current density would be decrease, as shown in Figures 5.18 a and b. It means that the FN tunneling mechanism decreased as the oxide thickness increases.

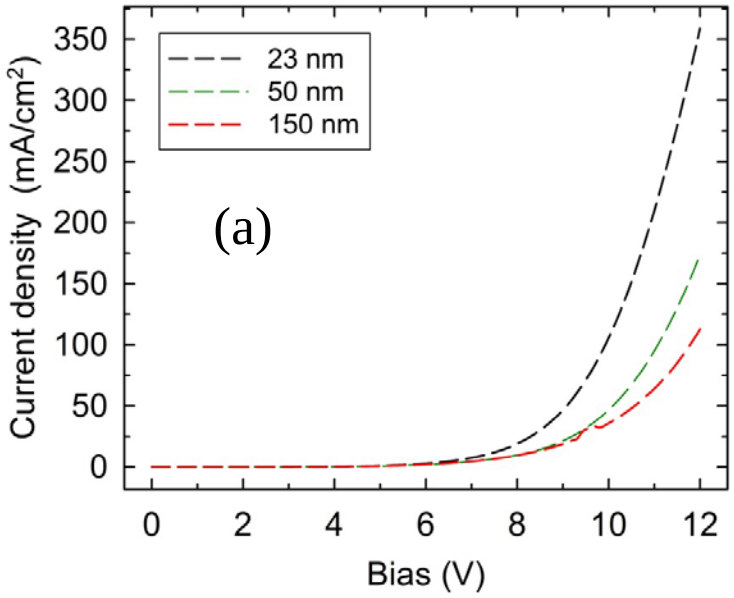

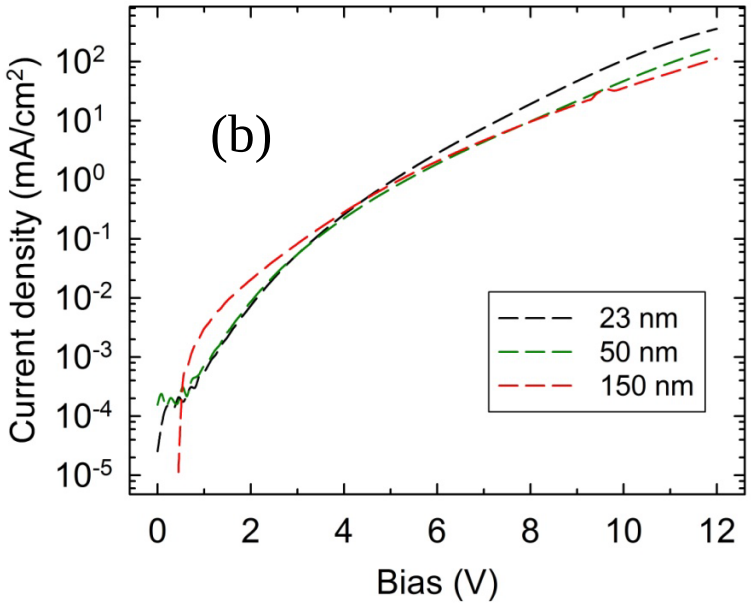

Figure 5.18. The current density vs. voltage in OLEDs with various oxide thickness. (a) Linear-Linear plot, and (b) Log-Log plot.

5.3 TOP EMITTING OLED WITH GQD

5.3.1 Broad area SiO_2 on p-Si with GQD as an active layer

In this experiment, the GQDs have been added as an active layer to the device structures with various thin oxide layers as illustrated in the previous section. Figure 5.19 shows the device structure and energy band diagram for with and without SiO2.

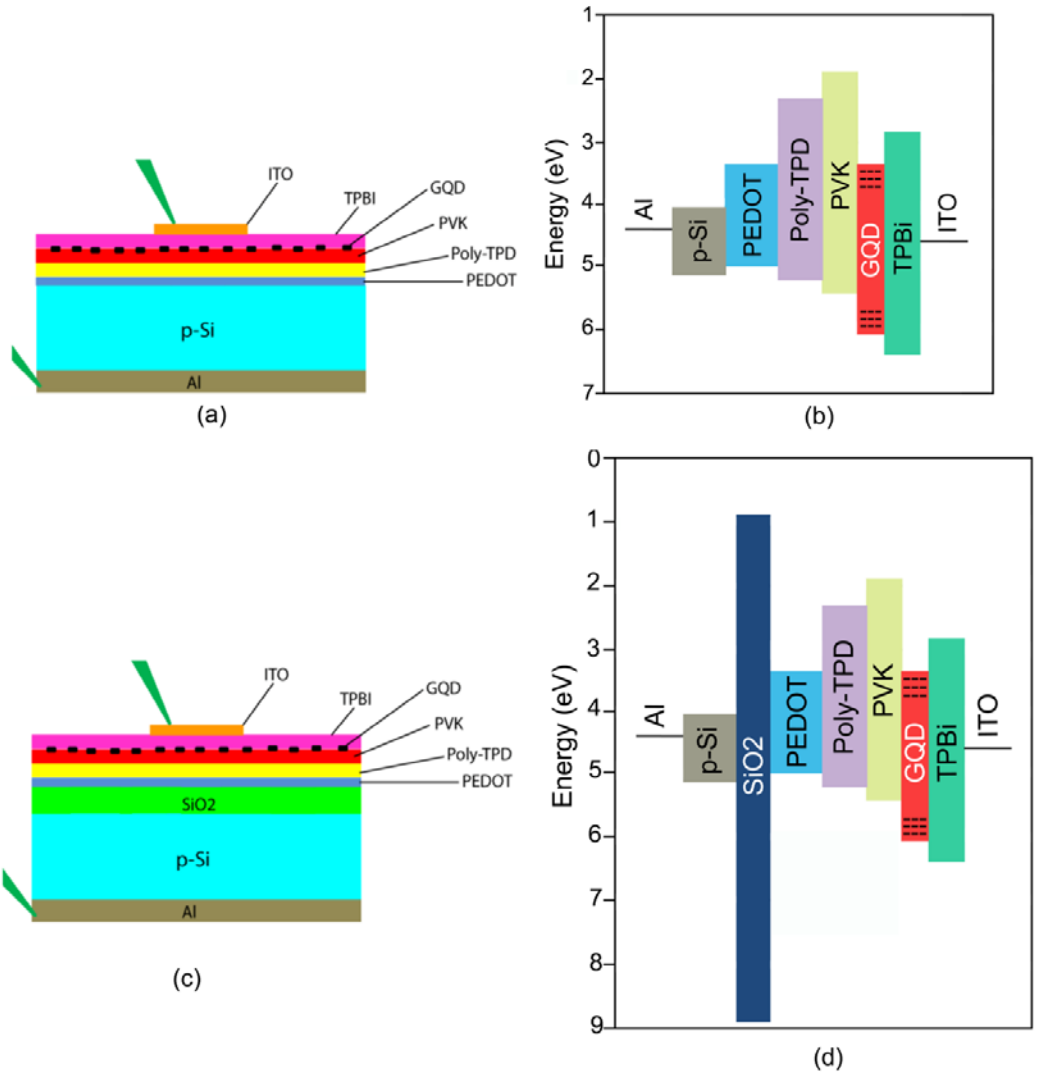

Figure 5.19. (a)The GQDs-based OLED structure with thin layer oxide buffer layer, and (b) energy band diagram of the device.

5.3.1.1 EL, digital photo and I-V measurement

The electruluminescence of the GQD-OLED has been measured and shown in Figure 5.20. All EL spectra is measured with same condition by appliying 12V for 4s integration time. As expected, the electroluminescence intensity increases when the thin oxide thickness

decreases. Likewise, the digital photo image of the output light has been recorded and shown in Figure 5.21.

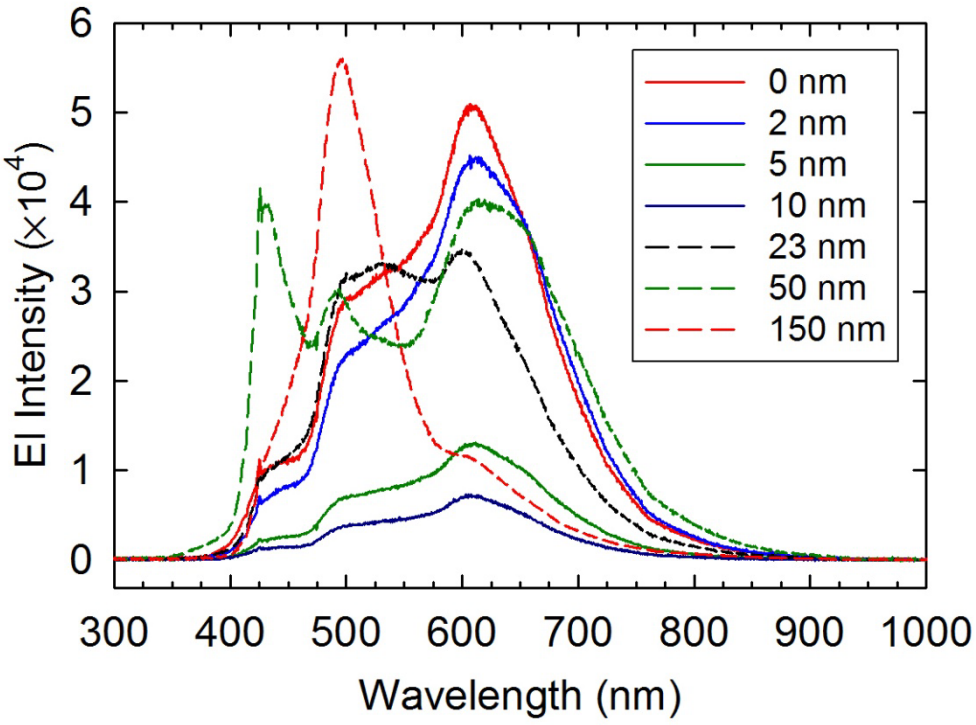

Figure 5.20. EL spectra of GQDs-based OLED with various oxide thickness

The I-V characteristics show that for the thin oxide thicknesses, 0, 2, 5, and 10 nm, by increasing the oxide thickness the current density is decreased due to the direct tunneling reduction (Figure 5.22). On the other hand, for the thick oxide thicknesses, 23, 50, and 150nm, the carrier injection is occurred because of the FN tunneling mechanism.

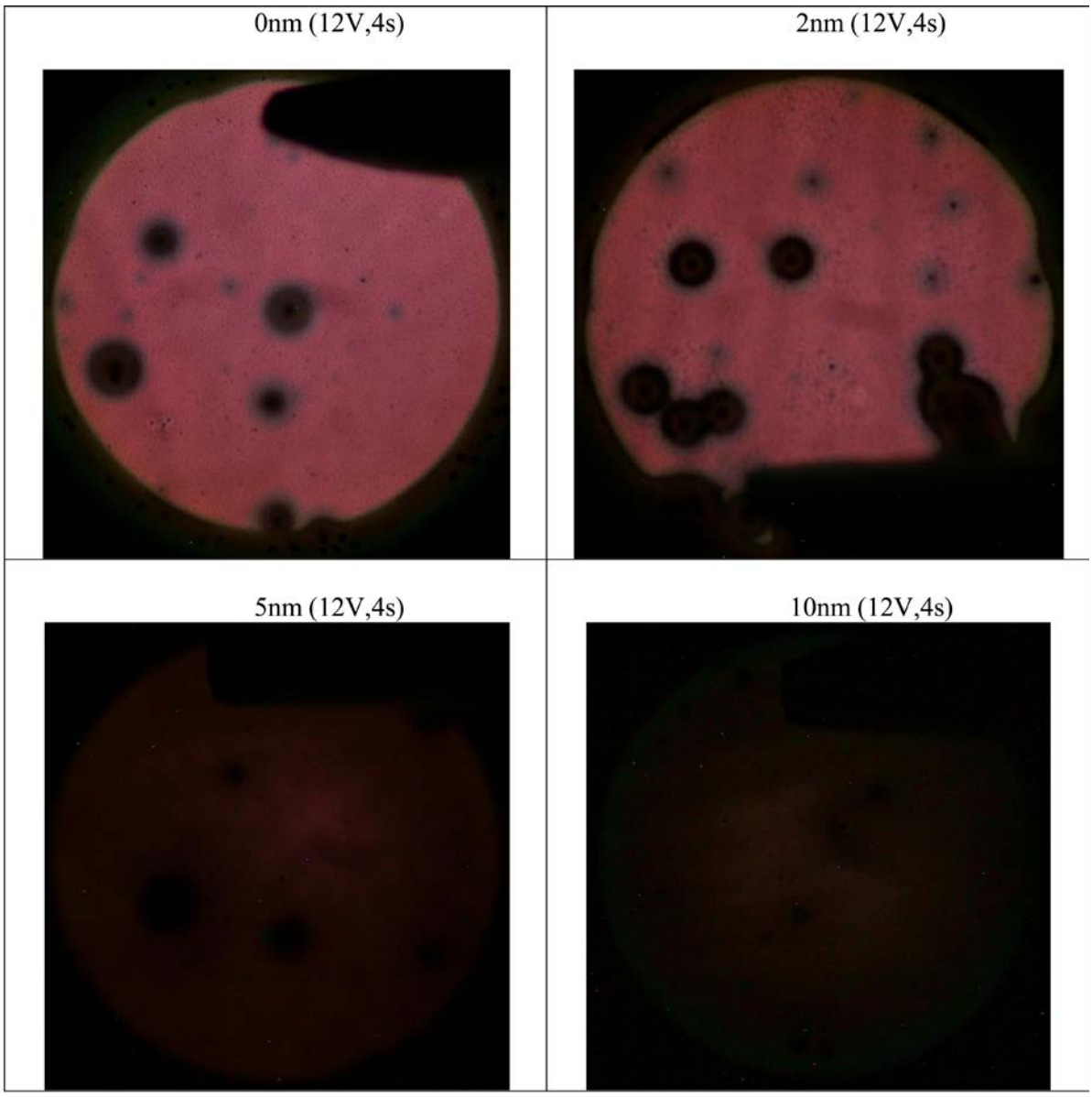
0nm (12V,4s)
2nm (12V,4s)
5nm (12V,4s)
10nm (12V,4s)

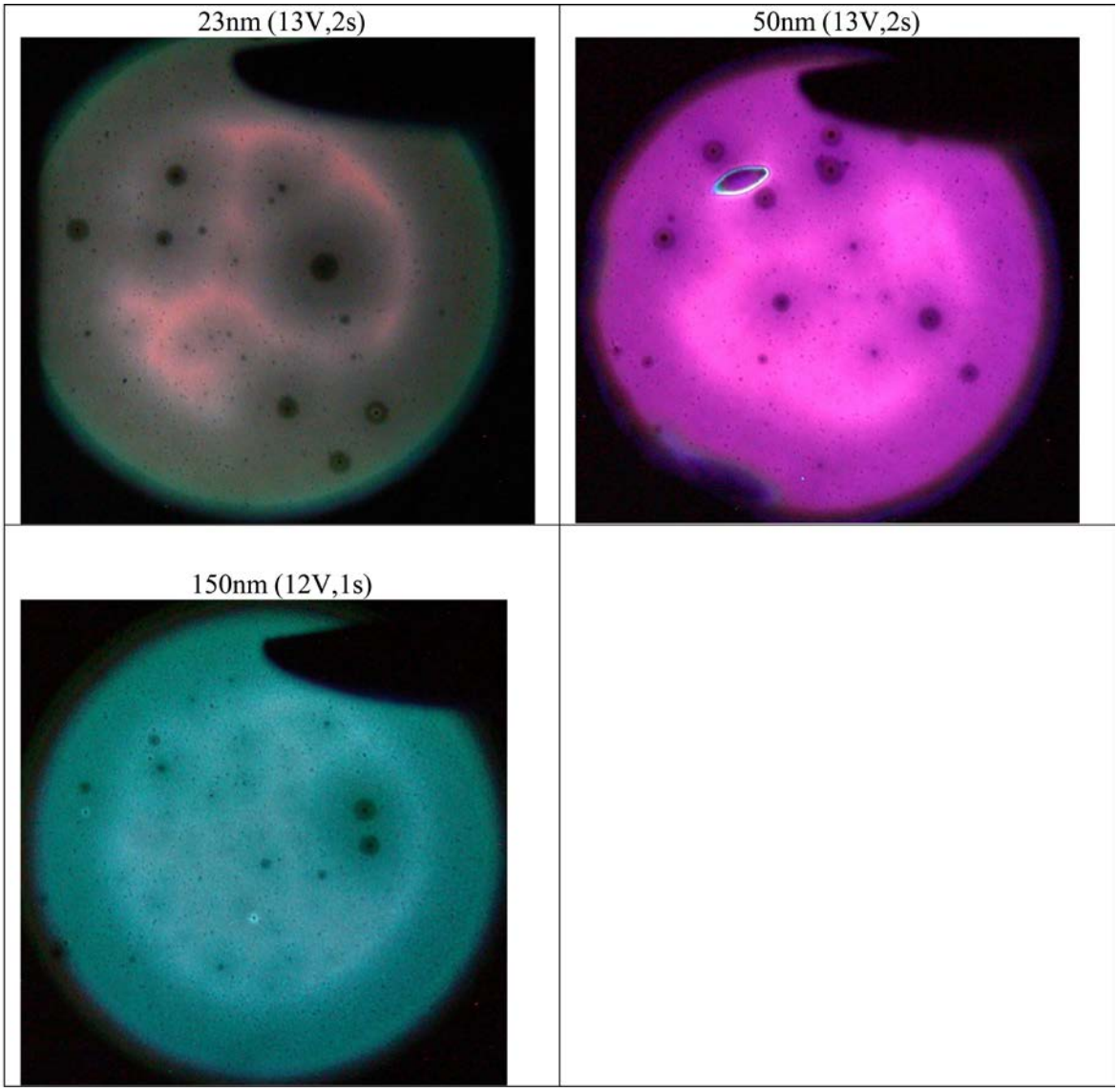

Figure 5.21. Digital image of lamination during CW injection for OLED with different thin and thick oxide thicknesses as a buffer layer.

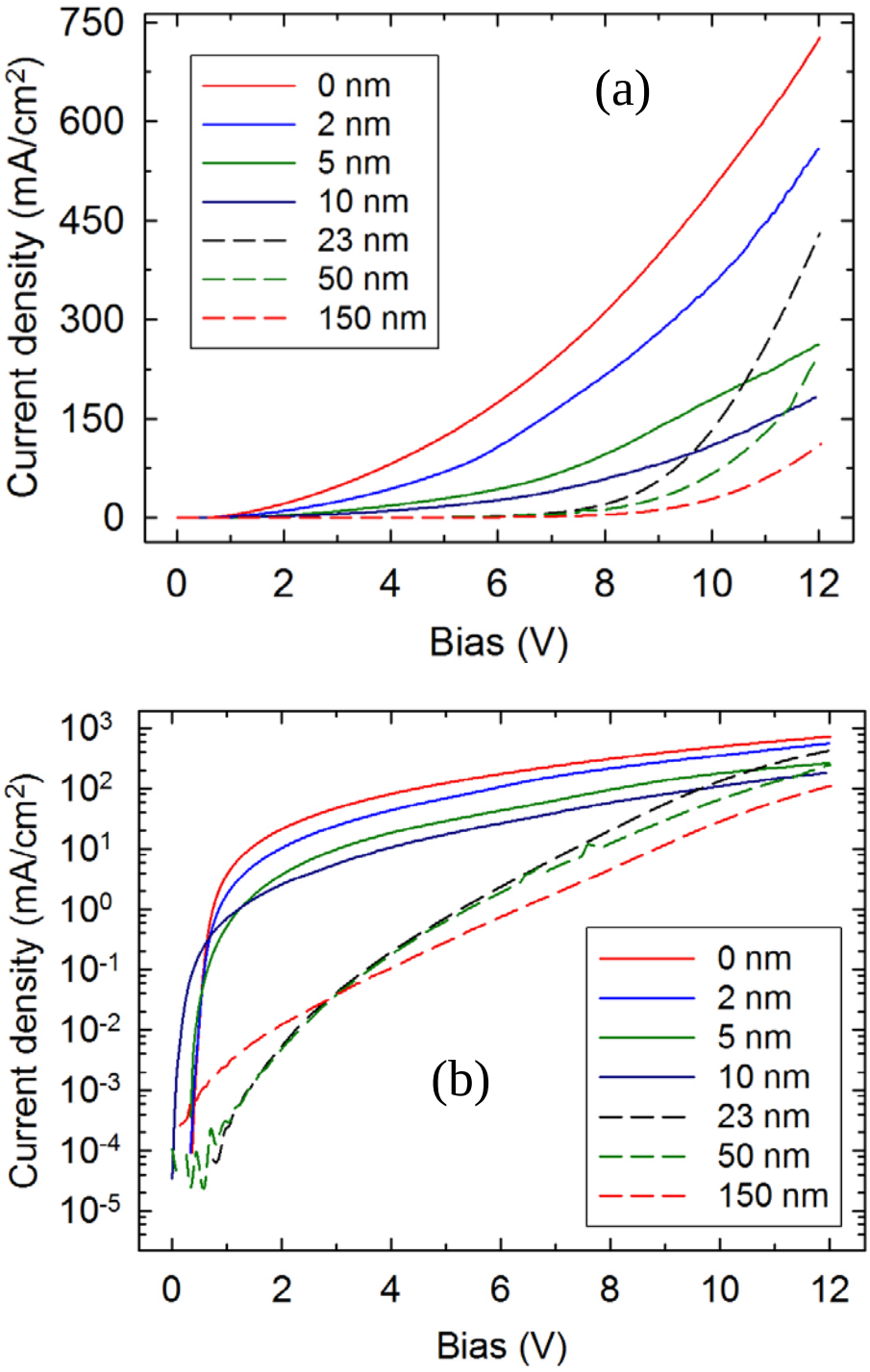

Figure 5.22. I-V characteristics for OLED with different thin and thick oxide as a buffer layer.

5.3.2 Window patterned structure with thick SiO_2 on p-Si with GQD as an active layer

In this section the previous experiments has been repeated by adding GQDs active layer in the device structure (Figure 5.23). The El spectra (at 12V and 4s integration time) and digital photo for the both thin and thick oxide structures have been measured and are shown in Figure 5.24 and 5.25, respectively. All measurement conditions for EL and photo measurements are remained same to have a fair comparison.

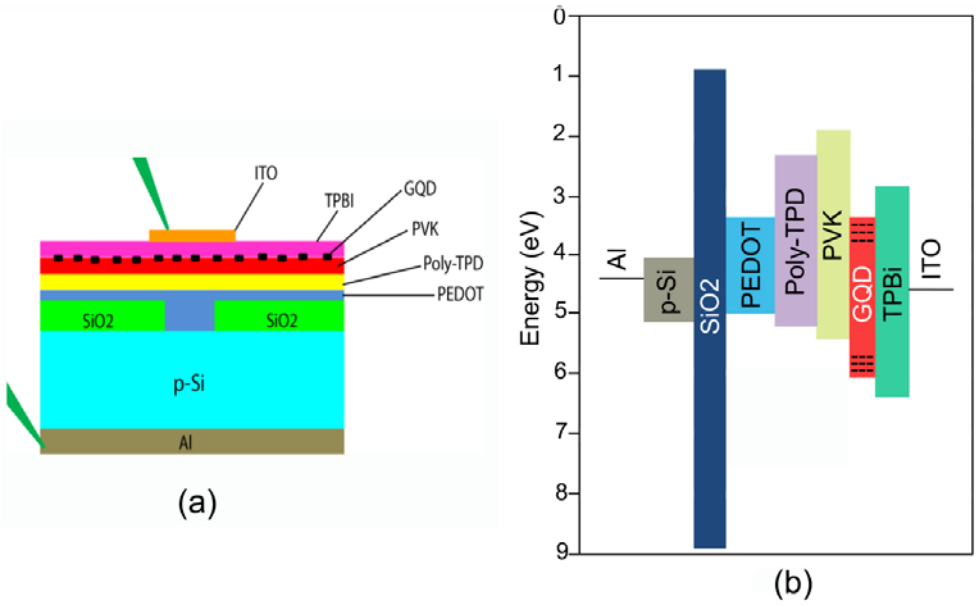

Figure 5.23. GQDs embedded in OLED structure with various oxide thicknesses. (a) Device structure, and (b) energy band diagram.

5.3.2.1 EL, Digital Photo, and I-V characteristic

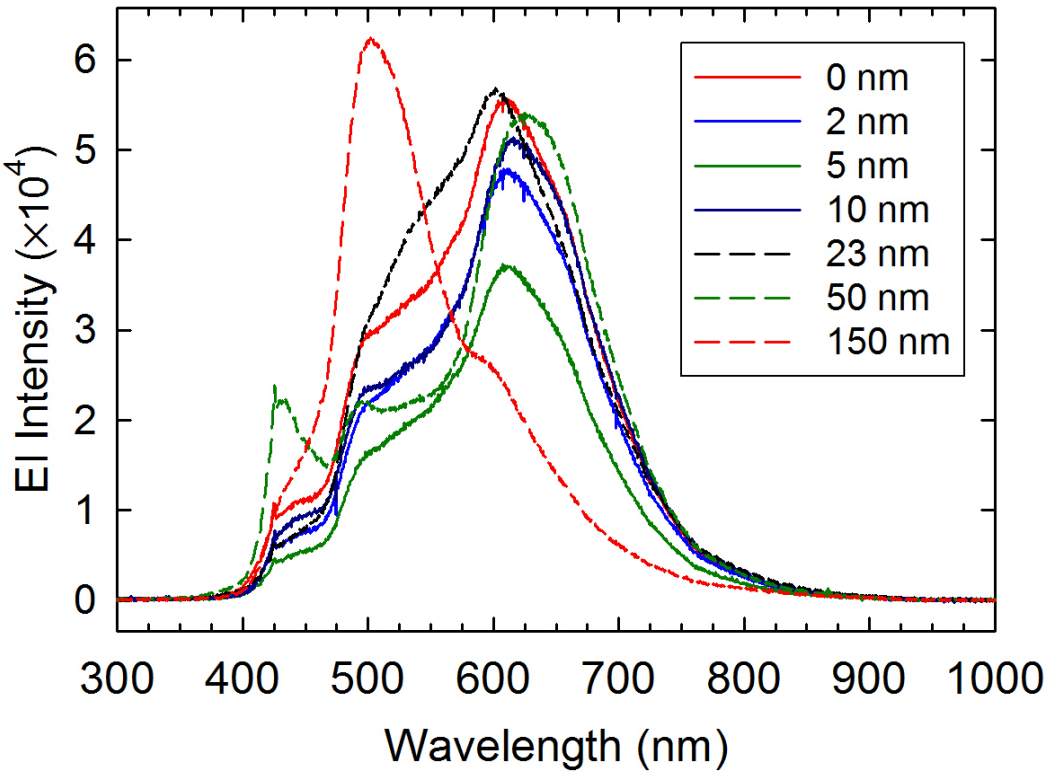

Figure. 5.24. The EL spectra for thin through thick oxide thickness in window patterned OLED structures embedded with GQD.

Native oxide (12V,4s) 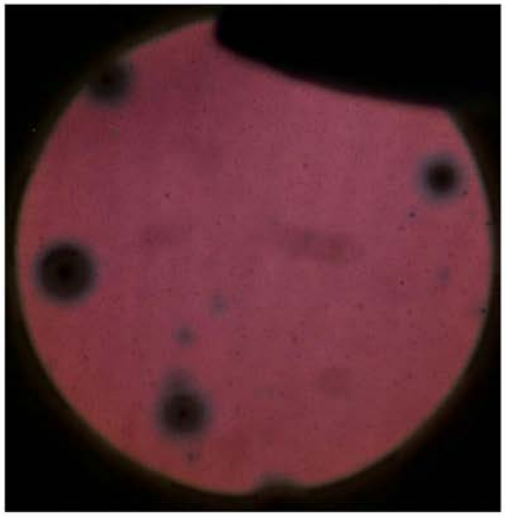	2nm (12V,4s) 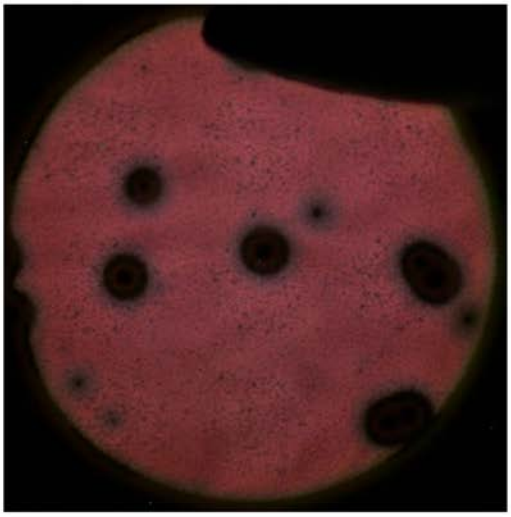
5nm (12V,4s) 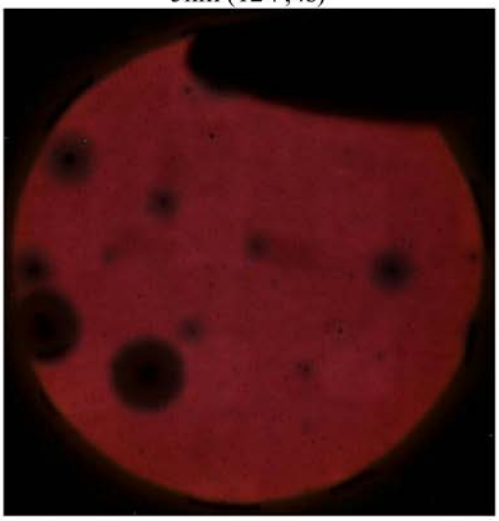	10nm (12V,4s) 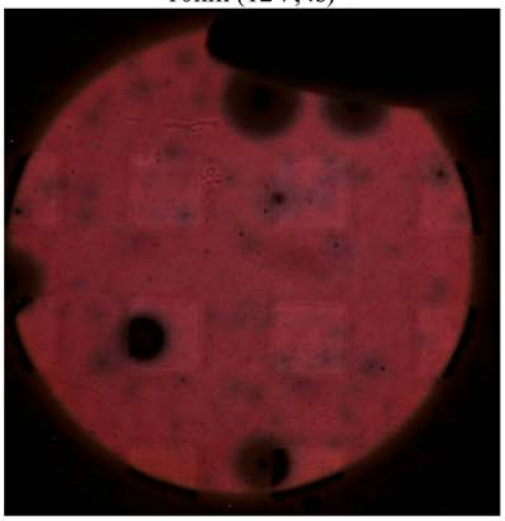

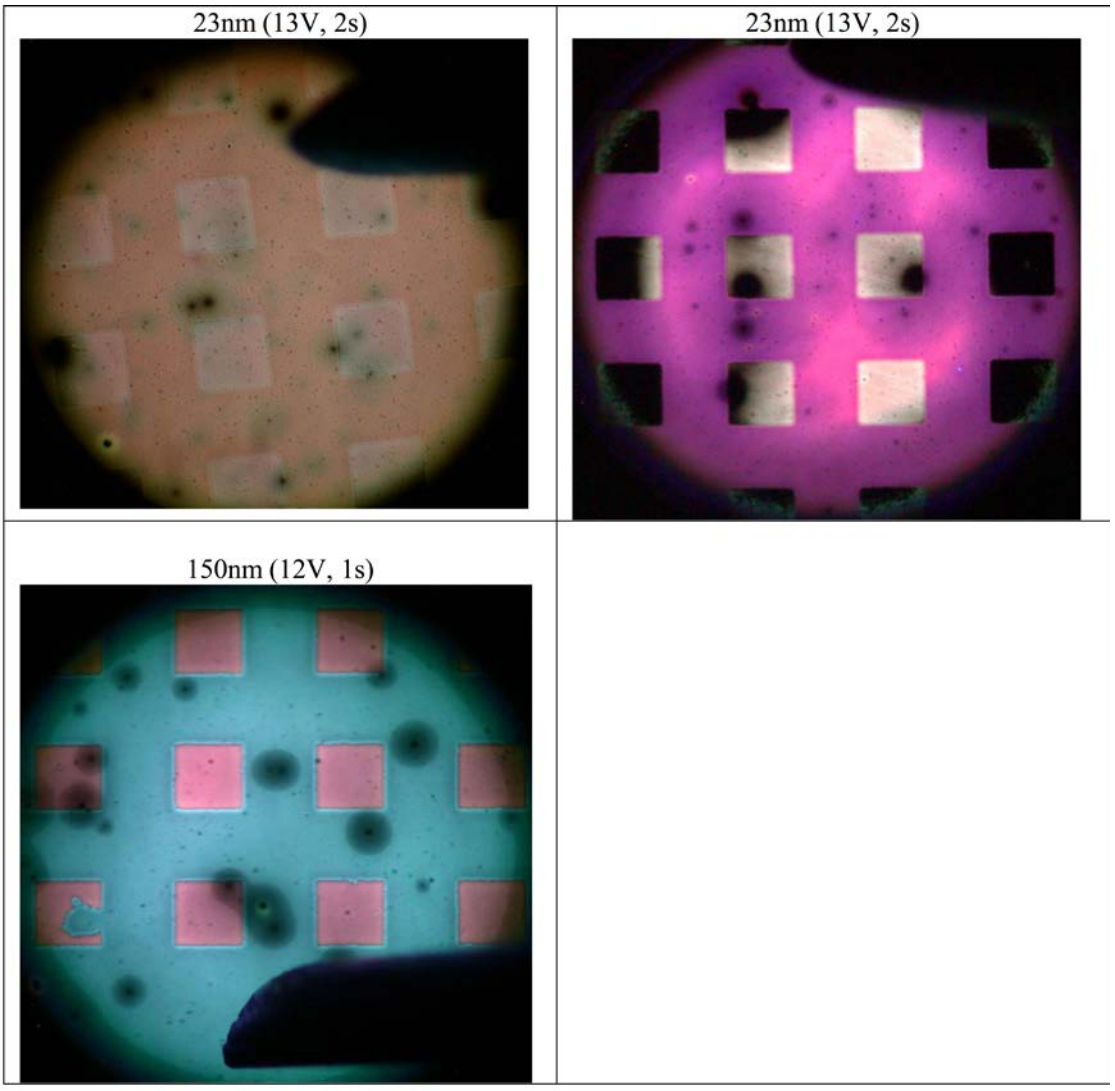

Figure 5.25. Digital image of lamination from OLED with embedded GQD (illumination from window regions).

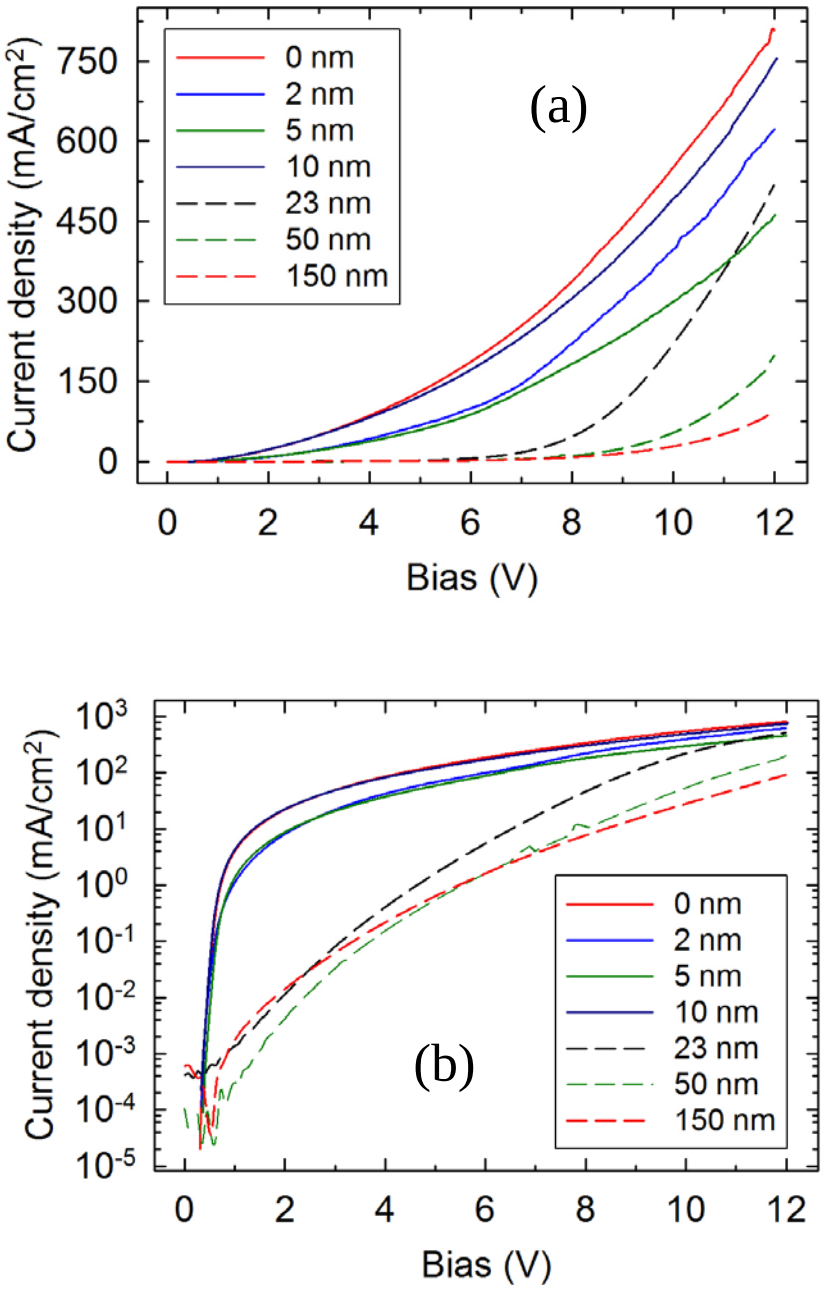

Figure 5.26. The current density vs. voltage of the OLEDs (with GQD at window region) with various thin and thick oxide thicknesses. (a) Linear-Linear, and (b) Log-Linear I-V curves

As the Figure 5.26 shows, by increasing the oxide thickness the current density would be increased. The reason why the current density for thinner oxide is larger than the thicker oxide is due to larger initial hole population for thinner one.

5.3.3 EL comparison for devices at various oxide thicknesses with GQD and without GQD

By comparing the EL spectrum of the device without GQDs and with GQDs, we can see the differences between two structures which indicate the GQDs contribution in EL emission. Figure 5.27 a, b, c, and d show the EL spectra comparison between the two structures with various oxide thickness as buffer layer for out of widow area. Embedding GQDs in device structure has improved the output light intensity due to the hole -electron recombination in GQD layer.

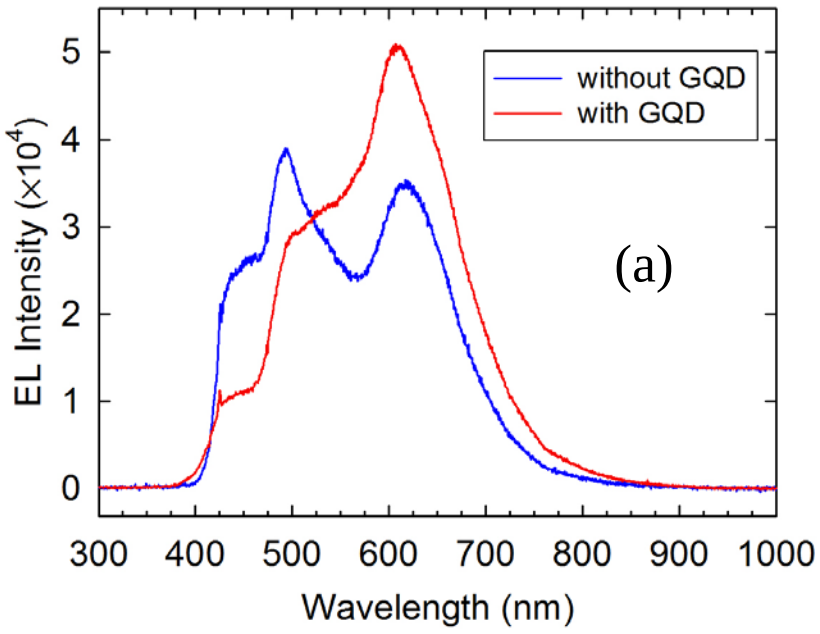

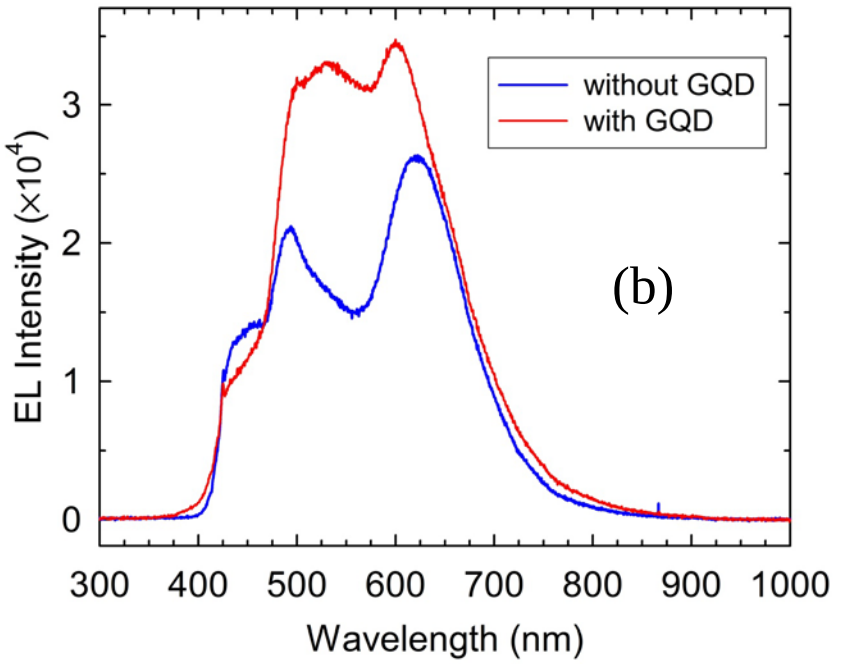
without GQD
with GQD
(b)
EL Intensity (×10^4)
Wavelength (nm)
0
1
2
3
300
400
500
600
700
800
900
1000

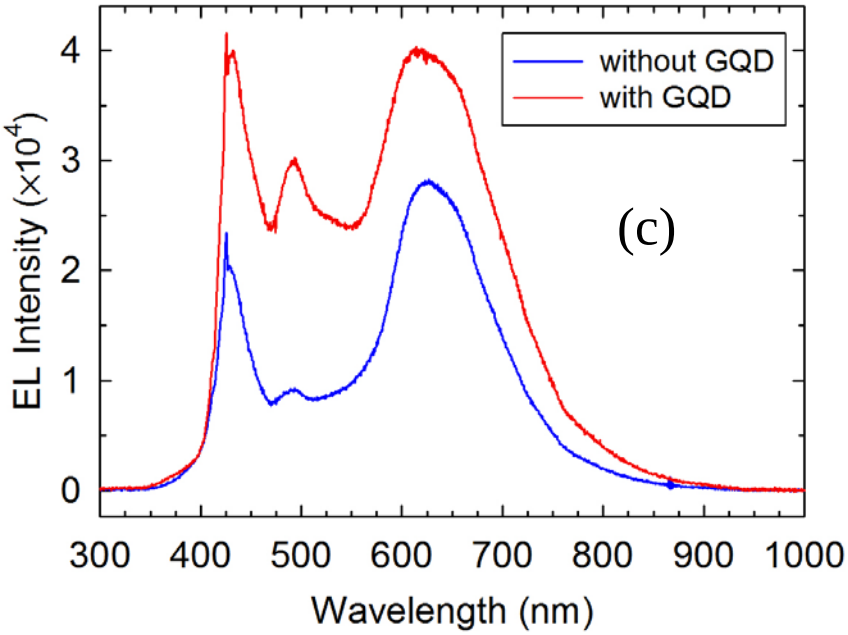
without GQD
with GQD
(c)
EL Intensity (×10^4)
Wavelength (nm)
0
1
2
3
4
300
400
500
600
700
800
900
1000

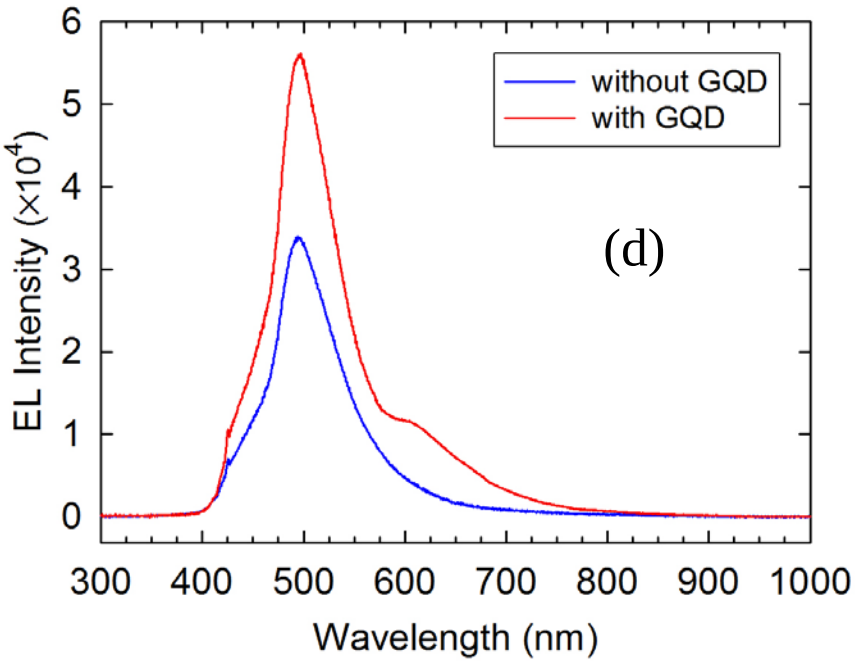

Figure 5.27. The EL spectrum comparison between OLED devices with GQDs and without GQDs for out of window area at various oxide buffer layer. (a) Native oxide, (b) 23nm SiO_2, (c) 50nm SiO_2, and (d) 150nm SiO_2.

Figure 5.27 (a) clearly shows the GQD emission for out of window area. Another experiment for this structure (with GQD, 0nm), illustrates the GQD emission with distinct emission wavelength as shown in Figure 5.28. In this Figure the EL spectra for the both without GQD and embedded GQD structure are normalized.

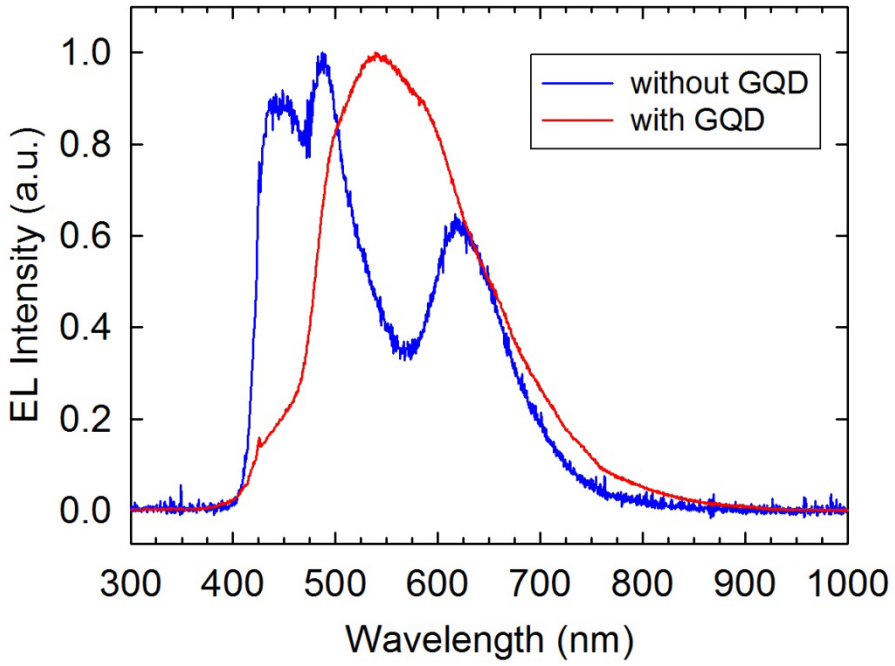

Figure 5.28. Normalized EL spectra comparison for with (18V,3s) and without GQD (18V, 22s) structure with 0nm oxide thickness.

6.0 SUMMARY

In this thesis, we have investigated the design and fabrication process of GQD-based OLEDs on ITO and silicon substrates. This study demonstrated the capacity of integration of silicon with GQDs which would provide the ability of using established CMOS technology. The unique property of GQDs such as wavelength tuning by their size makes them a promising candidate for light emitting applications. To enhance the device performance, the organic materials with appropriate HOMO/LUMO energy were chosen. The hole transport and electron transport materials with high band-gap rather than the GQDs, help hole-electron injection through the active layer. For GQD-OLED on silicon substrate, buffer oxide layer (2-150nm) is grown to improve device efficiency by blocking electrons within active layer. Two different injection mechanisms have been studied for thin and thick oxide thickness. For thin oxide (2-10nm), holes follow the direct tunneling to penetrate through the oxide. However, for thick oxide the band bending due to the external field enables holes to tunnel into the p-type transport material. We could tune the output color by changing the oxide thickness from red to blue. In fact, for thicker oxide only hole with higher energy are able to tunnel based on Fowler-Nordheim mechanism. These high energy holes can excite high energy states of the active layer which results in blue shift in output light.

REFERENCES

[1] R. Victor; K. Irina, Proceedings of SPIE 3948, 206–219 (2000).

[2] P. Anikeeva; J. Halpert; M. Bawendi; V. Bulovic, Nano Letters, 9, 2532–2536 (2009).

[3] P. Guyot-Sionnest, The Journal of American Physical Chemistry, 3, 1169-1175 (2012).

[4] Saleh, Bahaa E. A.; Teich, Malvin Carl. Fundamentals of Photonics. Wiley. p. 498 (2013).

[5] Tetsuo Tsutsui, Nature, 420, 753–755 (2002).

[6] E. Gautier, A. Lorin, J. M. Nunzi, A. Schalchli, J. J. Benattar, and D. Vital, Appl. Phys. Lett. 69, 1071-1074 (1996).

[7] Li, G.; Abroshan, H.; Chen, Y.; Jin, R.; Kim, H. J., J. Am. Chem. Soc., 137, 14295-14304 (2015).

[8] Y. Hirose, Kahn, V. Aristov, and P. Soukiassian, Appl. Phys. Lett. 68, 217-220 (1996).

[9] Shin-ya Takizawa, Victor A. Montes and Pavel AnzenbacherJr., Chem. Mater., 21, 2452–2458 (2009).

[10] L. X. Xiao, Z. J. Chen, B. Qu, J. X. Luo, S. Kong, Q. H. Gong, and J. J. Kido, Adv Mater, 23, 926-952 (2011).

[11] Chang Y F, Chen C Y, Luo F T, et al., Organic Electronics, 13, 388-393 (2012).

[12] Yong Hyun Kim, Christoph Sachse, Michael L. Machala, Christian May, Lars Müller-Meskamp, and Karl Leo, Adv. Funct. Mater, 21, 1076–1081 (2011).

[13] Abroshan, H.; Akbarzadeh, H.; Taherkhani, F.; Parsafar, G., Mol. Phys., 109, 709-724 (2011).

[14] L. Groenendaal, F. Jonas, D. Freitag, H. Pielartzik, J. R. Reynolds, Adv. Mater., 12, 481-494 (2000).

[15] Thesen, M.W.et al. J. Polym. Sci. A 48, 3417–3430 (2010).

[16] Xingliang Dai, Zhenxing Zhang, Yizheng Jin, Yuan Niu, Hujia Cao, Xiaoyong Liang, Liwei Chen, Jianpu Wang & Xiaogang Peng, Nature, 515, 96-99 (2014).

[17] Lee, D.-H., Liu,Y.-P., Lee, K.-H., Chae, H. & Cho, S.M. Org. Electron., 11, 427–433 (2010).

[18] Brian L. Scott; Ke Wang; Vincent Caluori; Gary Pickrell, Opt. Eng., 48, 100501-100501-3 (2009).

[19] Zhang, Y. B.; Tan, Y. W.; Stormer, H. L.; Kim, P., Nature, 438, 201-204 (2005).

[20] Stankovich, S.; Dikin, D. A.; Dommett, G. H. B.; Kohlhaas, K. M.; Zimney, E. J.; Stach, E. A.; Piner, R. D.; Nguyen, S. T.; Ruoff, R. S., Graphene-Based Composite Materials. Nature, 442, 282-286 (2006).

[21] Geim, A. K.; Novoselov, K. S., The Rise of Graphene. Nat. Mater. 6, 183-191 (2007).

[22] Kopelevich, Y.; Esquinazi, P., Graphene Physics in Graphite. Adv. Mater.19, 4559-4563 (2007).

[23] Akbarzadeh, H.; Abroshan, H.; Parsafar, G. A., Solid State Commun, 150, 254-257 (2010).

[24] Dikin, D. A.; Stankovich, S.; Zimney, E. J.; Piner, R. D.; Dommett, G. H. B.; Evmenenko, G.; Nguyen, S. T.; Ruoff, R. S., Nature, 448, 457-460 (2007).

[25] Ponomarenko, L. A.; Schedin, F.; Katsnelson, M. I.; Yang, R.; Hill, E. W.; Novoselov, K. S.; Geim, A. K., Science, 320, 356-358 (2008).

[26] Zhang, M.; Bai, L. L.; Shang, W. H.; Xie, W. J.; Ma, H.; Fu, Y. Y.; Fang, D. C.; Sun, H.; Fan, L. Z.; Han, M. et al., J. Mater. Chem., 22, 7461-7467 (2012).

[27] Zhuo, S. J.; Shao, M. W.; Lee, S. T., ACS Nano, 6, 1059-1064 (2012).

[28] Liu, C.; Abroshan, H.; Yan, C.; Li, G.; Haruta, M., ACS Catal., 6, 92-99 (2015).

[29] Yan, X.; Cui, X.; Li, B. S.; Li, L. S., Large, Nano Lett. 10, 1869-1873 (2010).

[30] Peng, J.; Gao, W.; Gupta, B. K.; Liu, Z.; Romero-Aburto, R.; Ge, L. H.; Song, L.; Alemany, L. B.; Zhan, X. B.; Gao, G. H. et al., Nano Lett., 12, 844-849 (2012).

[31] Pan, D. Y.; Zhang, J. C.; Li, Z.; Wu, M. H., Adv. Mater., 22, 734-738, (2010).

[32] O. Voznyy, A. D. Güçlü, P. Potasz, and P. Hawrylak, Phys. Rev., 83, 165417 (2011).

[33] Li, Y.; Hu, Y.; Zhao, Y.; Shi, G. Q.; Deng, L. E.; Hou, Y. B.; Qu, L. T., Adv. Mater., 23, 776-780 (2011).

[34] Eda, G.; Lin, Y. Y.; Mattevi, C.; Yamaguchi, H.; Chen, H. A.; Chen, I. S.; Chen, C. W.; Chhowalla, M., Adv. Mater., 22, 505-509 (2010).

[35] Loh, K. P.; Bao, Q. L.; Eda, G.; Chhowalla, M., Nat. Chem., 2, 1015-1024 (2010).

[36] L. Li, G. Wu, G. Yang, J. Peng, J. Zhao and J.-J. Zhu, Nanoscale, 5, 4015–4039 (2013).

[37] R. Liu, D. Wu, X. Feng and K. Mullen, J. Am. Chem. Soc., 133, 15221–15223 (2011).

[38] D. Pan, L. Guo, J. Zhang, C. Xi, Q. Xue, H. Huang, J. Li, Z. Zhang, W. Yu, Z. Chen, Z. Li and M. Wu, J. Mater. Chem., 22, 3314–3318 (2012).

[39] Kim et al. ACS NANO, 6, 8203–8208 (2012).

[40] Mahasin Alam Sk, Arundithi Ananthanarayanan, Lin Huang,a Kok Hwa Lim and Peng Chen. J. Mater. Chem. C, 2, 6954–6960 (2014).

[41] X. T. Zheng, A. Than, A. Ananthanaraya, D.-H. Kim and P. Chen, ACS Nano, 7, 6278–6286 (2013).

[42] A. Ananthanarayanan, X. Wang, P. Routh, B. Sana, S. Lim,D.-H. Kim, K.-H. Lim, J. Li and P. Chen, Adv. Funct. Mater., 24, 3021–3026 (2014).

[43] Lin, J.; Abroshan, H.; Liu, C.; Zhu, M.; Li, G.; Haruta, M., J. Catalysis, 330, 354-361 (2015).

[44] M. L. Mueller, X. Yan, J. A. McGuire and L.-s. Li, Nano Lett., 10, 2679–2682 (2010).

[45] Naoto Fuyuno, Daichi Kozawa, Yuhei Miyauchi, Shinichiro Mouri, Ryo Kitaura, Hisanori Shinohara, Toku Yasuda, Naoki Komatsu, and Kazunari Matsuda, Materials Science, 2, 983–989 (2014).

[46] http://www.acsmaterial.com/product.asp?cid=141&id=1185 ,CAS NO.7440-40-0.

[47] Shuai Chen, Jia-Wei Liu, and Jian-Hua Wang, Chem. Commun., 48, 7637–7639 (2012).

[48] Lingling Li, Gehui Wu and Jun-Jie Zhu, Nanoscale, 5, 4015 (2013).

[49] Lee, C. J., pode, R.B., Han, J. I., Moon, D. G., Applied Surface Science, 253, 4249- 4253 (2007).

[50] You, Z. Z., Microelectronics Journal, 38, 564– 569 (2007).

[51] Tang, C. W., VanSlyke, S. A., Appl. Phys. Lett., 51, 12-15 (1987).

[52] J. R. Sheats, H. Antoniadis, M. Hueschen, W. Leonard, J. Miller, R. Moon, D. Roitman, and A. Stocking, Science 273, 884 (1996).

[53] P. E. Burrows, V. Bulovic, S. R. Forrest, L. S. Sapochak, D. M. McCarty, and M. E. Thompson, Appl. Phys. Lett., 65, 2922-2925 (1994).

[54] Abroshan, H.; Li, G.; Lin, J.; Kim, H. J.; Jin, R., J. Catalysis, 337, 72-79 (2016).

[55] J. C. Scott, J. H. Kaufman, P. J. Brock, R. DiPietro, J. Salem, and J. A. Goitia, J. Appl. Phys. 79, 2745-2751 (1996).

[56] I. D. Parker, J. Appl. Phys. 75, 1656-1666 (1994).

[57] Y. Yang, E. Westerweele, C. Zhang, P. Smith, and A. J. Heeger, J. Appl. Phys. 77, 694-698 (1995).

[58] Y. Yang and A. J. Heeger, Appl. Phys. Lett. 64, 1245-1247 (1994).

[59] I.-M. Chan, W.-C. Cheng and F. C. Hong, Appl. Phys. Lett., 80, 13-15 (2002).

[60] C. C. Wu, C. I. Wu, J. C. Sturm, and A. Kahn, Appl. Phys. Lett., 70, 11-14 (1997).

[61] Woosung Kwon, Young-Hoon Kim, Chang-Lyoul Lee, Minkyung Lee, Hee Cheul Choi, Tae-Woo Lee, and Shi-Woo Rhee, Nano Lett., 14, 1306−1311 (2014).

[62] Ishii, H.; Hayashi, N.; Ito, E.; Washizu, Y.; Sugi, K.; Kimura, Y.; Niwano, M.; Ouchi, Y.; Seki, K. Phys. Status Solidi A, 201, 1075−1094 (2004).

[63] L. S. Hung, C. W. Tang, and M. G. Mason, Appl. Phys. Lett., 70, 2-4 (1997)

[64] Y.-E. Kim, H. Park, and J.-J. Kim, Appl. Phys. Lett. 69, 599-601 (1996)

[65] E. Ettedgui, H. Razafitrimo, Y. Gao, and B. R. Hsieh, Appl. Phys. Lett. 67, 2705-2707 (1995).

[66] P. E. Burrows, V. Bulovic, S. R. Forrest, L. S. Sapochak, D. M. McCarty, and M. E. Thompson, Appl. Phys. Lett. 65, 2922-2924 (1994).

[67] J. C. Scott, J. H. Kautman, P. J. Brock, R. DiPietro, J. Salam, and J. A Goitia, J. Appl. Phys. 79, 2745-2751 (1996).

[68] A. R. Schlatmann, D. Wilms Floet, A. Hilberer, F. Garten, P. J. M. Smul- ders, T. M. Klawijk, and G. Hadziioannou, Appl. Phys. Lett. 69, 1764-1766 (1996).

[69] E. Gautier, A. Lorin, J. M. Nunzi, A. Schalchli, J. J. Benattar, and D. Vital, Appl. Phys. Lett. 69, 1071-1073 (1996).

[70] Akbarzadeh, H.; Abroshan, H.; Taherkhani, F.; Parsafar, G. A., Solid State Commun, 151, 965-970 (2011).

[71] Y. Hirose, Kahn, V. Aristov, and P. Soukiassian, Appl. Phys. Lett. 68, 217-219 (1996).

[72] C. W. Tang and S. A. Van Slyke, Appl. Phys. Lett. 51, 913-915 (1987).

[73] C. W. Tang, S. A. Van Slyke, and C. H. Chen, J. Appl. Phys. 65, 3610-3616 (1989).

[74] S. A. VanSlyke, C. H. Chen, and C. W. Tang, Appl. Phys. Lett. 69, 2160-2162 (1996).

[75] C. C. Wu, C. I. Wu, J. C. Sturm, and A. Kahn, Appl. Phys. Lett. 70, 1348-1350 (1997).

[76] F. Li, H. Tang, J. Shinar, O. Resto, and S. Z. Weisz, Appl. Phys. Lett. 70, 2741-2743 (1997).

[77] S. Fujita, T. Sakamoto, K. Ueda, and K. Ohta, Jpn. J. Appl. Phys., 36, 350 (1997).

[78] X. Zhou, J. He, L. Liao, M. Lu, Z. Xiong, X. Ding, X. Hou, F. Tao, C. Zhou, and S. Lee, App. Phys. Lett., 74, 4, 609–611 (1999).

[79] D. R. Baigent, R. N. Marks, N. C. Greenham, R. H. Friend, S. C. Moratti, and A. B. Holmes, Appl. Phys. Lett., 65, 2636-2648 (1994).

[80] V. Bulovic, P. Tian, P. E. Burrows, M. R. Gokhale, S. R. Forrest, and M. E. Thompson, Appl. Phys. Lett. 70, 2954-2956 (1997).

[81] I. D. Parker and H. H. Kim, Appl. Phys. Lett. 64, 1774-1776 (1994).

[82] M. Morita, T. Ohmi, E. Hasegawa, M. Kawakami, and M. Ohwada, Appl. Phys. 68, 1272-1281 (1990).

[83] S. Khadka, and A. C. Coleman, Master Thesis, Uni. of Illinois at Urbana Cjamaign (2013).

[84] X. Zhou, J. He,L.S.Liao, M. Lu, Z. H. Xiong, X. M. Ding, X.Y. Hou, F. G. Tao, C.E.Zhou, S. T. Lee, Appl. Phys. Lett., 74, 609-611 (1999).

[85] C.J. Huang, S. Han, D. Grozea, A. Turak, Z.H. Lu, J. Appl. Phys. 97, 086107 (2005).

[86] W. Mo¨nch, Semiconductor Surfaces and Interfaces (Springer, Berlin, 1993).

[87] P. V. Dressendorfer and R. C. Barker, Appl. Phys. Lett. 36, 933-935 (1980).

[88] S. Horiguchi and H. Yoshino, J. Appl. Phys. 58, 1597-1600 (1985).

[89] S. Heike, Y. Wada, S. Kondo, M. Lutwyche, K. Murayama, and H. Kuroda, Extended Abstracts of the International Conference on Solid State Devices and Materials, Yokohama, Japan (1994).

[90] V. Kumar and W. E. Dahlke, Solid-State Electron. 20, 143 (1977).

[91] Taherkhani, F.; Akbarzadeh, H.; Abroshan, H.; Fortunelli, A., Fluid Phase Equilib, 335, 26-31 (2012).

[92] F. J. Grunthaner and P. J. Grunthaner, Mater. Sci. Rep. 1, 147 (1986).

[93] J. L. Alay, M. Hirose, J. Appl. Phys. 81, 1-10, 1997.

[94] Xiao-Wen Zhanga, Jun Li, Liang Zhanga, Hua-Ping Lina, Xue-Yin Jianga, Wen-Qing Zhua, Zhi-Lin Zhanga, Synthetic Metals 160, 788–790 (2010).

[95] W. Q. Zhao, G. Z. Ran, W. J. Xu, and G. G. Qin, Appl. Phys. Lett. 92, 073303-073305 (2008).

[96] G. L. Ma, G. Z. Ran, A. G. Xu, Y. H. Xu, Y. P. Qiao, W. X. Chen, L. Dai, and G. G. Qin, Appl. Phys. Lett. 87, 081106-081108 (2005).

[97] W. Soutter, “An Introduction to Quantum Tunneling” 1–5, (1927).

[98] K. Roy, S. Mukhopadhyay, and H. Mahmoodi-Meimand, “Leakage Current Mechanisms and Leakage Reduction Techniques in Deep-Submicrometer CMOS Circuits,” Proceedings of the IEEE, 91, (2003).

[99] R. W. Dutton, “Direct tunneling current model for circuit simulation,” International Electron Devices Meeting, Technical Digest (Cat. No.99CH36318), 3, 735–738 (1999).

[100] R . H . Fowler and L . Nordheim, Series A , Containing Papers of a Mathematical and Physical character, Published by : The Royal Society Stable, 781, 173–181 (1928).

[101] M. A. Grado-Caffaro and M. Grado-Caffaro, 121, 2001–2002, (2010).

[102] E. Miranda and F. Palumbo, Solid-State Electronics, 61, 93–95 (2011).